



HAL
open science

Advanced virtual simulation for optimal cutting parameters control in five axis milling

? Hendriko

► **To cite this version:**

? Hendriko. Advanced virtual simulation for optimal cutting parameters control in five axis milling. Other [cond-mat.other]. Université Blaise Pascal - Clermont-Ferrand II, 2014. English. NNT: 2014CLF22464 . tel-01176218

HAL Id: tel-01176218

<https://theses.hal.science/tel-01176218>

Submitted on 15 Jul 2015

HAL is a multi-disciplinary open access archive for the deposit and dissemination of scientific research documents, whether they are published or not. The documents may come from teaching and research institutions in France or abroad, or from public or private research centers.

L'archive ouverte pluridisciplinaire **HAL**, est destinée au dépôt et à la diffusion de documents scientifiques de niveau recherche, publiés ou non, émanant des établissements d'enseignement et de recherche français ou étrangers, des laboratoires publics ou privés.

Titre :

Advanced virtual simulation for optimal cutting parameters control in five axis milling

Résumé

La thèse concerne l'usinage à 5 axes de formes complexes. Le but est d'estimer le plus précisément possible les efforts induits par la coupe pour ajuster la vitesse d'avance et gagner en performance. Pour cela, il est nécessaire d'estimer les engagements radial et axial de la fraise à chaque instant. Ce calcul est rendu particulièrement complexe à cause de la forme de la pièce, de la forme du brut et de la complexité de la géométrie de l'outil. Les méthodes usuelles par Zbuffer sont particulièrement coûteuses en temps de calcul. Dans ces travaux nous proposons une méthode de calcul rapide à partir d'une modélisation du contact dans toutes les situations envisageables. Différentes simulations et expérimentations ont permis de valider la précision expérimentalement.

Mots clés

Français

CFAO, Usinage à 5 axes, modélisation de l'enlèvement de matière, estimation des efforts de coupe

Anglais

CAD / CAM, 5 axes milling, Toroidal cutter, material removal rate simulation, cutting forces simulation

N° d'ordre : 2466

EDSPIC : 657

Université Blaise Pascal - Clermont II
Universitas Indonesia – Indonesia

École doctorale
Sciences pour l'Ingénieur de Clermont-Ferrand

Thèse de Doctorat
Présentée par

HENDRIKO

Pour obtenir le grade de :
DOCTEUR D'UNIVERSITE BLAISE PASCAL
Et
DOCTOR IN UNIVERSIATAS INDONESIA

Spécialité : GÉNIE MÉCANIQUE

***Advanced virtual simulation for optimal cutting parameters
control in five axis milling***

Soutenue publiquement le 24 juin 2014 devant le jury

Pr	Danardono	AS. DEA	Universitas Indonesia	
Dr	Ario	BASKORO	Universitas Indonesia	
Dr	Hélène	CHANAL	IFMA	
Pr	Emmanuel	DUC	IFMA	Co-directeur
Pr	Jean-Yves	HASCOET	Ecole centrale de Nantes	Rapporteur
Dr	Jos	ISTIYANTO	Universitas Indonesia	
Pr	G.	KISWANTO	Universitas Indonesia	Directeur
Pr	Henry	PARIS	Université Joseph Fourier- Grenoble	Président / Rapporteur

Institut Pascal – Universiata Indonesia



UNIVERSITE BLAISE PASCAL



UNIVERSITAS INDONESIA

THESIS

**A dissertation submitted in partial fulfillments of the
requirements for the degree of
DOCTOR IN UNIVERSITE BLAISE PASCAL
and
DOCTOR IN UNIVERSITAS INDONESIA**

HENDRIKO

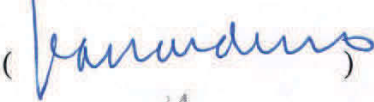
**ADVANCED VIRTUAL SIMULATION FOR
OPTIMAL CUTTING PARAMETERS
CONTROL IN FIVE-AXIS MILLING**

HALAMAN PENGESAHAN

Disertasi ini diajukan oleh :
Nama : Hendriko
NPM : 1006783434
Program Studi : Teknik Mesin
Judul Disertasi : Advanced Virtual Simulation for Optimal Cutting
Parameters Control in Five-Axis Milling

Telah berhasil dipertahankan di hadapan Dewan Penguji dan diterima sebagai bagian persyaratan yang diperlukan untuk memperoleh gelar Doktor pada Program Studi Doktor Teknik Mesin, Fakultas Teknik, Universitas Indonesia.

DEWAN PENGUJI

Promotor : Dr. Ir. Gandjar Kiswanto, M.Eng. ()
Kopromotor : Prof. Emmanuel Duc ()
Penguji I : Prof. Danardono AS, DEA ()
Ketua
Penguji II : Prof. Henri Paris ()
Anggota
Penguji III : Prof. Jean Yves Hascoët ()
Anggota
Penguji IV : Dr. Hélène Chanal ()
Anggota
Penguji V : Dr. Jos Istiyanto, MT ()
Anggota
Penguji VI : Dr. Ario Sunar Baskoro, M.Eng. ()
Anggota

Ditetapkan di : Depok

Tanggal : 24 Juni 2014

DIPLOME DE DOCTEUR
Thèse en Cotutelle (arrêté du 06 janvier 2005)

UNIVERSITE BLAISE PASCAL - CLERMONT-FERRAND II
UNIVERSITAS INDONESIA - INDONESIA

Date de la soutenance : 24 juin 2014

Titulaire du master of engineering obtenu en Malaisie en 2008 - autorisation de la
Présidente de l'UBP en date du 20/10/2011

SUJET DE LA THESE : *Advanced virtual simulation for optimal cutting parameters
control in five axis machining*

M. HENDRIKO a été jugé digne du grade de **DOCTEUR**
D'UNIVERSITE Spécialité : GÉNIE MÉCANIQUE

LES MEMBRES DU JURY :

M. AS. DEA Danardono - Professeur - Universitas Indonesia

M. BASKORO Ario - Docteur - Universitas Indonesia

M. BEAKOU Alexis - Professeur - IFMA - Clermont-Ferrand - invité

Mme CHANAL Hélène - Maître de conférences HDR - IFMA - Clermont-Ferrand

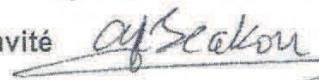
M. DUC Emmanuel - Professeur - IFMA - Clermont-Ferrand

M. HASCOET Jean-Yves - Professeur - Ecole Centrale de Nantes

M. ISTIYANTO JOS - Docteur - Universitas Indonesia

M. KISWANTO G. - Professeur - Universitas Indonesia

M. PARIS Henry - Professeur - Université Joseph Fourier - Grenoble



ABSTRACT

Name : Hendriko
Department : Mechanical Engineering
Title : Advanced Virtual Simulation For Optimal Cutting Parameters
Control In Five-Axis Milling

In five-axis milling of 3D free-form surface, determining the continuously changing Cutter Workpiece Engagement (CWE) for supporting force and surface quality prediction remains a challenge. In order to predict the cutting forces accurately, precise geometric information on cutter workpiece engagement is very important. Solid models and discrete methods are the most common methods used to predict the engagement region. However, both methods give the result with the accuracy as the tolerance set in the beginning. The methods suffer with the long computational time. Several studies in the CWE generation using analytical method have been performed. The results showed that analytical approaches were proven much faster and more accurate over the discrete approaches. However, despite this method has the advantage compared with the discrete method and solid models, but the current available studies are still limited to three axis milling and flat workpiece surface.

This study presents new simple methods to define Cutter Workpiece Engagement during sculptured surface machining in five-axis milling. The proposed models were developed for two cutting tools that are widely used in the machining process, flat-end and toroidal cutting tool. The instantaneous CWE was defined by determining two engagement points, the lowermost engagement (LE)-point and the uppermost engagement (UE)-point. For flat-end cutter, the LE-point is always located at the bottom side. Meanwhile for toroidal cutter, an extended method to define the grazing point in swept volume development was employed to define the instantaneous LE-point.

The UE-point was calculated using a combination of discretization and analytical method. During rough milling and semi-finish milling, the workpiece surface was represented by vertical vector. The method called the *Toroidal-boundary* was employed to obtain the UE-point when it was located on the cutting tool at the toroidal side. On the other hand, the method called the *Cylindrical-*

boundary was used to calculate the UE-point on a flat-end cutter and on the cylindrical side of a toroidal cutter. Moreover, when the workpiece is a non-straight staircase, the UE-point was calculated using the *Curve-boundary* method. The equation derived in this study was used to develop a simulation program that was called the *Analytical Boundary Simulation (ABS)*. The simulation program can be employed to generate the shape and length of cut. The accuracy of the proposed model was verified two times, first by comparing the coordinate of the UE-points with respect to the workpiece surface, and the second using a commercial CAD software, Siemens-NX. The results proved that the proposed method is accurate. The efficiency of the proposed model in generating the CWE was compared with the *Z*-mapping method. The result confirmed that the proposed model is more efficient in term of computational time.

For machining with a free-form surface, the surface was discretized using normal vector. Although the workpiece surface was discretized, but there was no calculation to check the intersection between a cutter and the normal vectors. The normal vectors were only used as the reference to define the shape of the surface at every CC-point mathematically. The engagement point was obtained using a combination of workpiece surface equation, parametric equation of cutting tool and tool orientation angles. The accuracy of the developed method was also tested using the verification methods that were applied in semi-finish milling. The results showed that the proposed model produced relatively small errors. It proved the accuracy of the method. Moreover, the method was eliminating the need for large number of *Z*-map to define the workpiece surface. The comparison test proved that the proposed method is much faster in term of computational time than *Z*-mapping method.

Cut geometry data from the CWE models were employed to support the method to calculate the cutting forces. In this study, mechanistic cutting force model was used. Cutting force coefficients as a function of axial depth of cut was obtained using a cubic polynomial fitting. The results of the tests showed that the calculated cutting forces have a good agreement with the cutting force generated from the experimental work.

TABLE OF CONTENTS

TITLE'S PAGE	i
HALAMAN PENGESAHAN	ii
ABSTRACT	iv
TABLE OF CONTENTS	vi
LIST OF FIGURES	x
LIST OF TABLES	xiv
NOMENCLATURES	xv
CHAPTER 1 : INTRODUCTION	1
CHAPTER 2 : LITERATURE REVIEW	7
2.1. Feedrate Optimization/Scheduling	7
2.1.1 Feedrate Optimization Methods	9
2.1.2 Classification of Control Parameters and Optimization Approaches	10
2.1.3 Volumetric Based Optimization Feedrate Optimization Methods	11
2.1.3.1 MRR calculation methods	12
2.1.3.2 MRR based feedrate scheduling implementation	14
2.1.4 Force-based Feedrate Optimization Methods	15
2.1.4.1 Geometric requirement for mechanistic cutting force	16
2.1.4.2 Feedrate scheduling based on mechanistic cutting force	17
2.1.4.3 Force-based feedrate scheduling algorithms and implementation	18
2.1.5 Discussion	20
2.2 Geometric Modeling for Supporting Virtual Machining	21
2.2.1 Curve (Wireframe) Modeling	21
2.2.2 Solid Modeling	22
2.2.3 Polyhedral Model based Methods	25
2.2.4 Discrete Vector based Methods	26
2.2.5 Analytical based Methods	27
2.2.6 Discussion	28
CHAPTER 3 : DEFINING TOOL ORIENTATION	30
3.1 Coordinate System in Five-Axis Milling	30
3.2 Effect of Helical Angle to the Tool Orientation	33

3.2.1	Identifying the Tool Mapping Operator and Tool Orientation Angle During Plain Milling	33
3.2.2	Identifying the Tool Mapping Operator and Tool Orientation Angle During Free-Form Milling	35
3.3	Cutting Tool Geometry and Selection in Five-Axis Milling	36
3.3.1	Parametric Equation of Flat-End and Toroidal Cutting Tool	37
3.3.2	Effect Of Helical Angle to the Shape of Swept Surface	39
3.4	Conclusion	39
 CHAPTER 4 : ANALYTICAL METHOD FOR OBTAINING THE LE-POINT AND THE UE-POINTS FOR ROUGH AND SEMI-FINISH MILLING		41
4.1	Calculating the Geometry of Cut	42
4.2	Obtaining LE-Points	44
4.2.1	Identifying LE-Point and the Length of Bottom Side CWE of Flat-End Cutting Tool	45
4.2.2	Identifying LE-Point and the Length of Bottom side CWE of Toroidal Cutting Tool	47
4.2.3	Application and Discussion	49
4.3	2.5D Rough Milling (Flat-End Cutter)	51
4.1.1.	Obtaining UE-Points During Rough Milling	51
4.1.2.	Effect of Helical Angle During Rough Milling	52
4.1.3	Application and Discussion	56
4.4	Semi Finish Milling with Straight Staircase Profile	57
4.4.1.	Obtaining UE-Point of Flat End Cutter During Semi Finish Milling	58
4.4.1.1	Application and discussion	61
4.4.2.	Obtaining UE-Point for Toroidal Cutter During Semi-Finish Milling	66
4.4.2.1.	Toroidal Boundary Method	68
4.4.2.2.	Identification and Calculation of Final UE-point	71
4.4.2.3.	Application and Discussion	74
4.4.2.4	Experimental Verification	79
4.4.2.5	Comparison with Z-mapping Method	80
4.5	Semi Finish Milling with Non-Straight Staircase Profile	82
4.5.1.	Curve Surface Representation	83
4.5.2.	Curve Boundary Method	84
4.5.3.	Obtaining Engagement Point	86
4.5.4.	Implementation and Discussion	88
4.6	Conclusion	90

CHAPTER 5 : ANALYTICAL METHOD FOR OBTAINING UE-POINTS ON FREE-FORM WORKPIECE SURFACE	92
5.1 Identifying Instantaneous Surface Shape	93
5.2 Obtaining UE-point of Free-form Surface Machining with Flat-End Cutter	96
5.2.1 Checking the Feasible Engagement Location	96
5.2.2 Obtaining UE-point	97
5.2.2.1 Step 1: Rotating the Projection Line by θ_B	97
5.2.2.2 Step 2: Inclined Surface	99
5.2.2.3 Step 3: Rotating the Rotated Line by θ_A	100
5.2.3 Application and Discussion	102
5.2.4 Comparison of Finish Model with Z-mapping	106
5.3 Obtaining UE-point of Free-Form Surface Machining with Toroidal Cutter	108
5.3.1 Checking the Feasible Engagement Location	108
5.3.2 Obtaining UE-point	110
5.3.2.1 Rotating the Rotated Line by θ_2	111
5.3.2.2 Calculate Toroidal Angle of UE-point	113
5.3.2.3 The UE-point for Every Engagement Angle	115
5.3.3 Application and Discussion	116
5.4 Conclusion	120
CHAPTER 6 : MODELING OF MILLING FORCE	122
6.1 Cutting Force Coefficient Identification	122
6.2 Mechanistic Modeling of Milling Forces	125
6.3 Identification of Specific Cutting and Edge Coefficients	127
6.4 Cutting Force Prediction in Five-Axis Milling	129
6.5 Simulation and Experimental Results	130
6.5.1. Cutting Force Coefficients	131
6.5.2. Model Implementation in Five-Axis Milling	132
6.6 Conclusion	138
CHAPTER 7 : CONCLUSION AND FUTURE WORKS	139
7.1 Conclusion	139
7.2 Future Works	140

REFERENCES 142

LIST OF FIGURES

Fig. 1-1	Upper engagement point and lower engagement point	6
Fig. 2-1	A comprehensive process simulation and optimization flow chart by Altintas [7]	8
Fig. 2-2	MRR calculation method, a) using dixel space, b) average MRR vs max. MRR [46], c) removed volume [46], d) The same MRR but different force [47], e) CWE for ball-end mill and chip thickness varies as a function of engagement angle [48]	12
Fig. 2-3	Detailed extraction of in-cut segment [52]	16
Fig. 2-4	Block diagram of feedrate adjustment based on mechanistic cutting force model [46]	19
Fig. 2-5	Extraction of ceF boundary using advancing semi cylinder technique [8]	23
Fig. 2-6	a) Instantaneous chip geometry extraction for 3-D ball-end milling [52], b) procedure for extracting in-cut segments of the cutting edge(s) [71]	24
Fig. 2-7	Faceted representation of a model [17]	26
Fig. 2-8	Workpiece representation with Z Direction Vectors (ZDV) approach [11]	27
Fig. 2-9	Top, front and detail view of boundaries [22]	28
Fig. 3-1	Illustration of the relationship among the coordinate systems, (a) three coordinate systems, (b) tool orientations relative to WCS, (c) entry angle	32
Fig. 3-2	Effect of helical angle to the cutting edge orientation with respect to engagement angle	33
Fig. 3-3	Cutting tool geometry, (a) generalized cutting tool model based on APT, (b) flat-end tool, (c) toroidal tool, (d) ball-end tool	36
Fig. 3-4	Geometry cutting tool, a) flat-end cutter, b) toroidal cutter	37
Fig. 3-5	Swept surface of flat-end tool with helical angle	39
Fig. 4-1	Effect of inclination angle to the CWE region in flat-end tool, (a) front view, (b) side view	45
Fig. 4-2	Bottom view of flat cutting tool	46
Fig. 4-3	Effect of inclination angle to the CWE region in toroidal tool, (a) front view, (b) side view	47
Fig. 4-4	Geometry of cutting tool at the bottom side, (a) bottom view, (b) front view	49
Fig. 4-5	Test on effect of some variables to LE-point, a) effect of inclination angle to λ_C , b) Effect of inclination angle to length of bottom CWE, c) LE-point on toroidal tool, d)	50

	Effect of helical angle to λ_c	
Fig. 4-6	a) Workpiece representation method for rough milling, b) CWE region and CWE points	51
Fig. 4-7	Feasible Location of UE-point during tool revolution	53
Fig. 4-8	Test model, a) part model, b) cut geometry without helical angle, c) cut geometry with helical angle	54
Fig. 4-9	The length of cut with and without helical angle	56
Fig. 4-10	Workpiece representation method	57
Fig. 4-11	Flowchart for obtaining CWE points for flat-end cutter	58
Fig. 4-12	Two possible location of UE-point for flat-end cutter, a) wall of workpiece, b) top of workpiece	59
Fig. 4-13	Location of UE-point when $z_A > z_B$	59
Fig. 4-14	Location of UE-point when $z_A < z_B$	60
Fig. 4-15	Test model, a) Part model, b) chip geometry generated by the program simulation	62
Fig. 4-16	The length of cut progression, a) without helical angle ($\chi=0$), b) with helical angle ($\chi=11$)	63
Fig. 4-17	Two types of model verification, a) comparing UE-point with respect to workpiece surface, b) verification using Siemens-NX	64
Fig. 4-18	Chip geometry of selected CC-points, a,b,c) the shape of cut at $\varphi \in \{0, 180\}$, d,e,f) the length of cut at $\varphi \in \{0,180\}$...	65
Fig. 4-19	Cut geometry of CC-12 at $\varphi \in \{0, 190\}$, a) with helical angle ($\chi = 11$), b) without helical angle, c) the length of cut	66
Fig. 4-20	Test model 2, a) part model, b) cut geometry generated by the program, c) the length of cut progression, d) cut geometry for several CC-point at $\varphi \in \{0, 180\}$	66
Fig. 4-21	Two possible locations of UE-point for toroidal cutter, a) wall of workpiece, b) top of workpiece	68
Fig. 4-22	Various possible conditions of CWE with toroidal cutter when $z_A < z_B$	71
Fig. 4-23	Various possible conditions of CWE with toroidal cutter when $z_A > z_B$	71
Fig. 4-24	Test model; a) Parts and workpiece for test model; b) CWE progression for one tool pass; c) verification	73
Fig. 4-25	The length of cut, a) without helical angle, b) with helical angle	74
Fig. 4-26	CWE from CC-37 a) the shape of cut without helical angle, b) the shape of cut with helical angle, and c) the length of cut as a function of engagement angle	75
Fig. 4-27	Test model 2; a) Parts and workpiece for test model; b) CWE progression for one tool pass	76
Fig. 4-28	The length of cut from (a) Test A ($\alpha = 0; \beta = 0$), (b) Test B ($\alpha = 15; \beta = 0$), (c) Test C ($\alpha = 15; \beta = 10$)	77

Fig. 4-29	Geometry of cut (a) Test A, (b) Test B, (c) Test C, and (d) the length of cut for CC-35	78
Fig. 4-30	Actual cutting verification, a) experimental setup, b) chip from machining, c) chip measured using Corel Draw X3, d) comparison of calculated and measured the length of cut	79
Fig. 4-31	Part model for computational time test	81
Fig. 4-32	Comparison of average computational time between ABS and Z-mapping	81
Fig. 4-33	Non straight staircase workpiece surface	82
Fig. 4-34	Flow chart to obtain CWE point for non-straight staircase	83
Fig. 4-35	Location of UE-point when $z_A > z_B$	86
Fig. 4-36	Location of UE-point when $z_A < z_B$	86
Fig. 4-37	a) Part and workpiece model, b) the length of cut progression, c) the shape and the length of cut for CC-4, and d) for CC-22	88
Fig. 4-38	Model verification, a) error of the proposed model, b) the sections of cut	89
Fig. 5-1	Workpiece surface representation, a) normal vector distribution, b) vector orientation in WCS, d) feasible surface shape combination	93
Fig. 5-2	Flow chart to obtain UE-point of flat-end cutter (cylindrical tool)	94
Fig. 5-3	Workpiece surface representation, a) top view of workpiece, b) method to calculate radius of surface	95
Fig. 5-4	Projection line and location of UE-point	96
Fig. 5-5	Rotation of projection line on S_x , a) convex surface, b) concave surface, c) slope surface, d) inclined surface	98
Fig. 5-6	Rotation of rotated projection line on S_i , a) convex surface, b) concave surface	100
Fig. 5-7	Engagement points on the wall of workpiece surface	101
Fig. 5-8	Part and workpiece design for test, and the shape of cut generated by program simulation	103
Fig. 5-9	The progression of length of cut for every test model.....	104
Fig. 5-10	The shape and the length of cut at $\varphi \in \{0, 180\}$ for selected CC-point	105
Fig. 5-11	Model verification, a) method to measure CWE in CAD software, b,c,d) error for $\varphi \in [0 : 10: 180]$	106
Fig. 5-12	Comparison of average computational time between ABS and Z-mapping	107
Fig. 5-13	Projection line of toroidal cutter	108
Fig. 5-14	Flow chart to obtain UE-point for toroidal cutter	109
Fig. 5-15	Rotation of the rotated projection line on S_i when engagement on toroidal and curved surface	112
Fig. 5-16	Intersection between cutter on toroidal side and curved	113

	surface, a) θ_2 positive, b) θ_2 negative	
Fig. 5-17	Intersection between cutter on toroidal side and slope surface, a) when θ_2 positive, b) when θ_2 negative	114
Fig. 5-18	Intersection between cutter on toroidal side and slope surface, a) when θ_2 positive, b) when θ_2 negative	115
Fig. 5-19	UE-point for $\varphi \in \{0, 90, 180\}$	116
Fig. 5-20	Test model; a,b,c,d) the shape of cut, e,f,g,h) the progression of the length of cut	117
Fig. 5-21	Error at every CC-point	118
Fig. 5-22	The shape of cut geometry, the length of cut and error for $\varphi \in \{0, 180\}$ at selected CC-points	119
Fig. 5-23	Actual cutting verification, a) chip from machining, b) chip measured using Corel Draw X3, c) comparison of calculated and measured the length of cut	120
Fig. 6-1	Orientation of cutting force components on cutting edge	125
Fig. 6-2	Two samples of cutting forces data, a) feedrate 0.3 mm/tooth and axial depth of cut 2 mm, b) feedrate 0.1 and axial depth of cut 10 mm	128
Fig. 6-3	Experimental setup	130
Fig. 6-4	Experimental and fitting of coefficients data, a) cutting coefficients, b) edge coefficients	132
Fig. 6-5	Test for semi-finish milling, a) part and workpiece model, b) the length of cut progression	134
Fig. 6-6	Comparison of F_x , a) measured, b) calculated, c) detail of calculated	135
Fig. 6-7	Comparison of F_y , a) measured, b) calculated, c) detail of calculated	135
Fig. 6-8	Comparison of F_z , a) measured, b) calculated, c) detail of calculated	136
Fig. 6-9	Test for finish milling, a) part and workpiece model, b) the length of cut progression	136
Fig. 6-10	Comparison of F_x , a) measured, b) calculated, c) detail of calculated	137
Fig. 6-11	Comparison of F_y , a) measured, b) calculated, c) detail of calculated	137
Fig. 6-12	Comparison of F_z , a) measured, b) calculated, c) detail of calculated	138

LIST OF TABLES

Table 4-1	: Method to identify and calculate CWE for flat-end cutter	61
Table 4-2	: Method to identify and calculate CWE for toroidal cutter	72
Table 4-3	: Method to identify and calculate CWE for curve surface	87
Table 5-1	: Variables used for selected engagement angle	110

NOMENCLATURES

- C_f : Lower engagement (LE) point
 n_f : Upper engagement (UE) point
 n_W : Engagement point on wall surface
 α : Inclination angle
 β : Screw angle
 ϑ : Tool orientation angle
 θ_A : Tool rotation angle in x -axis
 θ_B : Tool rotation angle in y -axis
 $[M]$: Operator to map the coordinate system from TCS to WCS
 $[M]_h$: Mapping operator when helical angle exist
 $[M]_F$: Mapping operator with respect to $\lambda_{i,j}$, φ and χ
 T : Coordinate of cutter location point
 V_T : Linear velocity within two subsequent CC-point
 ε : Entry angle
 φ : Engagement angle
 φ_b : Engagement angle of back cutting edge
 χ : Helical angle
 r : Minor radius
 r_m : Distance between cutter centre point to the minor radius
 $\theta_{A\chi}$: Orientation of cutting edge relative to x -axis, due to helical angle
 $\theta_{B\chi}$: Orientation of cutting edge relative to y -axis, due to helical angle
 R : Radius of flat-end cutter
 ψ_C : Lag angle of flat-end cutter
 ψ_t : Lag angle of toroidal cutter
 Λ : Toroidal angle
 λ_n : Toroidal angle of UE-point
 λ_C : Toroidal angle of LE-point
 D : Axial depth of cut
 L : Length of cut
 l_n : Length of engagement on cylindrical side

- l_b : Length of engagement at bottom side of cutting edge
- ϑ_D : Orientation cutting edge relative to z -axis
- h : Cut thickness
- f : Feedrate
- A_φ : Cross cut area
- ω : Angular velocity
- R_x : Radius of workpiece surface in x -axis
- R_y : Radius of workpiece surface in y -axis
- μ_x : Orientation of normal vector in x -axis
- μ_y : Orientation of normal vector in y -axis
- S_x : Shape of curve surface in x -axis
- S_y : Shape of curve surface in y -axis
- F_t : Tangential cutting force
- F_r : Radial cutting force
- F_a : Axial cutting force
- F_X : Cutting force in X -direction
- F_Y : Cutting force in Y -direction
- F_Z : Cutting force in Z -direction
- K_{tc} : Tangential cutting force coefficient
- K_{rc} : Radial cutting force coefficient
- K_{ac} : Axial cutting force coefficient
- K_{te} : Tangential edge force coefficient
- K_{re} : Radial edge force coefficient
- K_{ae} : Axial edge force coefficient
- ϕ_j : Toroidal angle of the small segment
- $L_{i,j}$: The length of cut of small segment

CHAPTER 1

INTRODUCTION

Multi-axis CNC milling is a key technology in machining a complex part with free-form surface. Application can be found in the milling of dies and mold, jet engine parts, pump blade, and biomedical parts. Technically, machining a small part will only take a few minutes in overall mass production, while dies, molds and aerospace parts in fact may take several days of machining when accuracy, precision and productivity become a critical factor in the economic survival of the manufacturing industry.

In today machining, the ability to automatically generates an optimal process plan is an essential step toward achieving automation, higher productivity and better accuracy. This requirement is particularly emphasized in die and mold manufacturing, where the complex cutter and workpiece geometry involved makes it difficult to generate the process plan. Current modern machine tools are Computer Numeric Control (CNC) milling machine and lathe. The Numeric Control (NC) Code program in each machine read by a microprocessor that user creates and performs the programmed operations. Traditionally, a costly time consuming process of machining process of plastic or wooden models was used to verify and corrects the NC program. For solving this kind of problem, various studies [1-4] have been conducted to produce a new approach called Virtual Machining (VM). This new approach is for advancing productivity and quality of the machining processes. Manufacturing process, includes designing, testing and producing the parts, is simulated in a virtual environment. This technique tries to decrease the lead time before the implementation of a new product and also to minimize the cycle of the product development. The main purposes of virtual machining in milling operation are how to predict the instantaneous cutting force and surface roughness. They can be used as an input to shorten the machining time by optimizing process parameter without sacrificing the machining quality.

This purpose is to overcome the remaining drawback of modern CNC which is the machining parameters, such as feedrate, cutting speed and depth of cut, are still programmed off line. There is no mathematical model of integrated machining physics used in the industry. Process planner selects machining parameters based on their accumulated experience which is gained through trial and error over a period of years. When machining a free-form surface that result in constantly changing tool orientation and depth of cut, they prefer to select moderate machining parameters which means that the value of feedrate is much lower than the recommended values specified by the tool maker. It is aimed to prevent unpredictable failures such as tool breakage, machining failure and low surface quality. By selecting low feedrate, the benchwork e.g. grinding and polishing to obtain the expected surface quality can be avoided. The bench-work is time consuming, such work accounting for about 80% of total machining time [5]. Therefore, it seems to be the best choice to obtain an efficient machining process. However, low feedrate causes the tool and the machine is not fully utilized. As a result, the machining is run under the operating condition that is inefficient and far from optimal condition.

In supporting the machining optimization, a precise geometrical information is very important especially in the modeling of the cutting forces. According to Salami et al.[6], there are three information required to calculate the instantaneous chip load *i.e.* in-cut segment of the cutting edge, tool angular position and chip thickness (undeformed radial chip thickness). According to Merdol and Altintas [4], there are two fundamental challenges in virtual machining process simulation system: identification of cutter-part intersection, feedrate intervals and development of computationally efficient process simulation algorithms. The geometric simulation must be fast enough as the number of cutter movement can be very large. The accuracy of predicted cut geometry must be high enough in order to predict the accurate machining forces. Various studies in geometric simulation strategy based on solid modeling include the constructive solid geometry (CSG) and the boundary representations (B-Rep) have been conducted. The CSG method is popular because this method can construct a complex surface using Boolean operator relatively easily, precisely

and accurately. Altintas and Spence [7,8] used the CSG to identify the cutter workpiece intersection to predict the cutting forces. El-Mounayri et al. [9] used a solid modeling system to compute the volume removed for a three-axis tool path.

Other researchers who have contributed significantly are Jerard et al. [10-12]. They evaluated the conditions of the cutter part engagement with a computationally efficient algorithms called the Z-map method. Using this method, the workpiece was broken into a set of evenly distributed discrete z-direction vectors (ZDV). The Z-map or dexel can be thought of as a special type of discrete vector model, or also known as discrete vertical vector [13]. Another type of discrete vector model is discrete normal vector. This model represents the workpiece as a set of position and direction vectors where the directions are generally the normal vectors at the corresponding surface point. Roth et al.[14, 15] tried to eliminate the need for an extended Z-map by introducing an adaptive depth buffer method for mechanistic modeling in three-axis and five-axis machining.

Another alternative for modeling CWE that is starting to receive more attention are Polyhedral Models. In this model the workpiece surface are represented by a finite set of polygonal planes called facets. The most commonly used shape is the triangle , because of this, the term facet is usually understood to mean triangular facet. In triangulated model, each facet is described by three vertices and a normal direction of the triangles. Several researches [16-18] on faceted based CWE extraction method for supporting the process modeling have been reported. The polyhedral modeling may offer a good compromise between manageable computational speed, robustness and accuracy. Another discretization method is voxel based discretization method. A voxel represents a single sample, or data point on a regularly spaced, three-dimensional grid. In virtual machining, several geometric studies [19-21] based-voxel volume representation have been reported.

Solid modeling gives more accurate information on the cutter workpiece engagement (CWE). 3D part model can be represented easily, precisely and accurately. But it has drawback in high computation time. The computation time drastically increases due to the surface-surface intersections. Meanwhile the

discrete models make the calculation become faster than solid modeling because it based on the vector/vertices-surface intersection instead of the surface-surface intersection. However, the computation time and memory consumption increases intensely as the precision and accuracy are improved. In a free-form surface machining, determining the cutter workpiece engagement become much more difficult because of complex tool path and target surface geometry. Although large studies have been reported in modeling the cutter workpiece engagement, but a good compromise between manageable computational speed and accuracy is still a challenge.

Discretization method to obtain the CWE data is time consuming, especially for a simple surface like a flat surface. To overcome such problem, Ozturk and Lazoglu [22] proposed an analytical method to determine chip load of ball-end mill during 3D free-form machining. Although the method is fast and accurate, but it is only applicable for three-axis milling with a flat workpiece surface. Spence et al. [23] reported an analytical method to calculate the cutter workpiece engagement using filled circles and rectangles as primitives to describe parts to be machined. They proposed two basic calculations, one was for the cutter engagement of circle primitives, and one was for the rectangles. Finally, a Boolean operation was applied to find the entry and exit angles on the cutter.

Another study was performed by Tunc and Budak [24], in which a simple analytical method called the bounding point coordinate was used for five-axis milling. By using this method, the depth of cut in each tool location can be predicted by defining the coordinate of the cutter contact point. The tests showed that the proposed method could predict the depth of cut well. However, this method was only applicable for a flat surface. When a sculptured workpiece surface was machined, then they used faceted model to represent the workpiece surface. Another limitation of the current analytical methods is they cannot provide the CWE data with respect to engagement angle. The instantaneous length of cut and cut thickness information are required to predict the instantaneous cutting forces [25-27]. Gupta et al. [28] mentioned that analytical approaches for computing the CWE are proven much faster and more accurate compared with the discrete approaches. But they do not work for a free-form surface geometries.

Even though analytical method is preferable to discrete method, studies on the CWE using this method have not been well developed, especially for complex surfaces.

From the above discussion it can be concluded that a number of challenges exist in the development of Virtual Machining. One of the challenges is how to calculate the CWE efficiently and accurately. Considering this challenge, the objectives of this thesis are:

1. To develop the CWE model

When machining a complex surface, a tool path may contain hundreds or thousands of tool motions that make the computational cost for obtaining the CWE prohibitively expensive. The limitations of analytical method for complex geometries motivate research in this thesis into methodologies that provide computationally simple analytical solution to generate CWE of complex part design and workpiece surface. The analytical methods of the CWE calculation are developed for various machining stages from 2.5D rough milling until finish milling operation.

The instantaneous length of cut is defined by determining two engagement points, the lowermost engagement (LE)-point, which is denoted by C_f , and the uppermost engagement (UE)-point, which is represented by n_f , as shown in Fig. 1-1. The LE-point is an engagement point that is located at the lowermost of CWE, meanwhile the UE-point is an engagement point that is located at the uppermost of CWE. The CWE models are developed for two types of cutting tools, flat-end cutter and toroidal cutter. The effects of helical angle, screw angle and inclination angle are taken into consideration in the model development.

The engagement points are determined using the parametric equations of the cutting tool and the base surface/rest surface information. In this study, the base surface of the proposed model is based on faceted model, while the information of the surface of rest of material, which is the part where the cutter is engaged, is based on Z-map data. The algorithms are developed by assuming all needed information, such as vertices, vertical and normal vector (this terminology will be explained in Chapter 4 and Chapter 5 in more detailed) are derived and

computed from the base surface and rest surface information. However, the method to obtain this data is not discussed in this study.

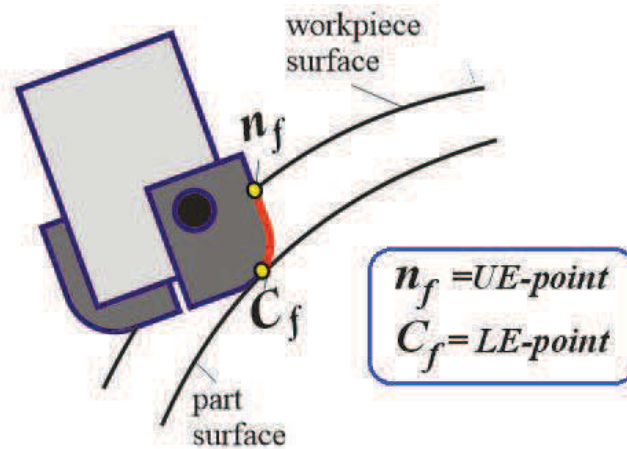


Fig. 1-1 UE-point and LE-point

2. To develop cutting force prediction model

To apply the CWE generator models to support the cutting force prediction model. In this study, *the linier edge mechanistic cutting force model* is used with the cutting force composed of the tangential, radial and axial components. The specific cutting and edge force coefficients for each force component are calculated using the experimental cutting forces data. In this model, the average cutting forces per tooth are measured and the effect of run-out on measurement can be minimized by dividing the total force per spindle revolution by the total number of teeth.

CHAPTER 2

LITERATURE REVIEW

Contrary to the advancement in machine tool technology and milling tool development, machining parameters such as feedrate, cutting speed, width of cut, are selected conventionally to avoid the risk of damaging workpiece, cutting tool and even the machine tool during the machining process. There is an increasing demand for virtual machining application that are capable in predicting the performance measures such as cutting forces, surface quality, tool deflection and power demands. Altintas [7] outlined a detailed flow chart of a comprehensive machining simulation and optimization scheme that consider not only the geometric factors but also mechanics and dynamics of milling, controller performance and feed drive dynamic as well as volumetric errors of a machine tool to compensate the machining errors and reduce the cycle time by adjusting the machining parameters (Fig. 2-1). Virtual machining has two main parts, geometric modeling and process modeling. The process modeling needs precise information about the CWE from the geometric modeling to predict the cutting forces. The main scope of this thesis is focused on the study of geometric and physical simulation of the machining optimization. CWE calculation becomes more challenging task when machining a complex part from a complex workpiece in multi-axis milling. In this chapter, some of important research contributions in this field will be reviewed, especially research into CWE generation, in-process workpiece modeling and feedrate optimization.

2.1. Feedrate Optimization/Scheduling

One of the optimization method in a free-form surface machining, which has become popular in recently, is feedrate scheduling. Selecting the most suitable feedrates values for machining of die, mould and other free-form surface parts, where the amount of material removal is constantly changing, has the potential for

great advantages. Even though an important progress is being done in machining science and technology during the last three decades, but the task to determine the optimal feedrates for machining processes is still not easy.

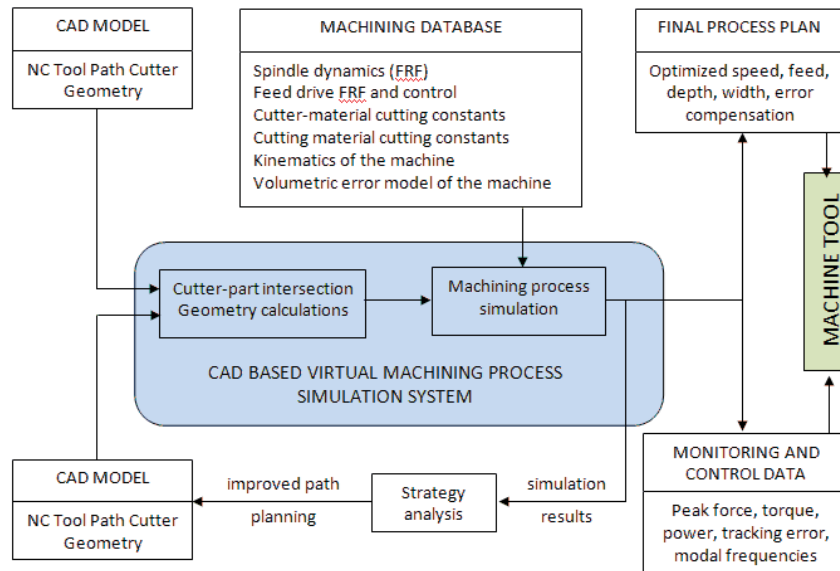


Fig. 2-1 A comprehensive process simulation and optimization flow chart by Altintas [7]

Mostly the modern CAD/CAM systems still apply conservative method of selecting a constant and low milling feedrate for a number of tool paths, based on the un-optimised cutting geometry. Currently, the CL file generators are based on only the geometric and volumetric analysis, but not on the physical processes of the free-form surface milling yet. During the machining process, instantaneous cutting force has to be controlled within a specified value for reducing the possibility of the tool deflection and avoiding tool damage. Milling force has become one of the most important process parameter that gives significant effect to the surface quality. Keeping constant cutting force in surface milling is very important for obtaining better cutting stability and hence improving the machined surface topography, texture and geometry. The conservative method select constant feedrate based upon the maximum cutting force, which is acquired during the whole machining of part. It will save the cutter but this results in longer machining time, with wide fluctuations, premature tool wear due to light chip load, which reduces productivity [29]. Therefore, in a complex surface machining,

it is assumed that inconstant feedrate is rescheduled so as to keep a fixed milling force. Piecewise feedrates that sustain safe cutting could supply substantial time savings to manufacturers. Lately, to increase the machining efficiency, variable feedrate optimization instead of fixed feedrate become very important under constraints of surface roughness, texture, dimensional accuracy and dynamic milling force.

2.1.1. Feedrate Optimization Methods

CNC machining optimization has been studied since about 60 years ago. The feedrate scheduling strategies can be classified into two groups: online adaptive control based optimization and computer simulation based (offline adaptive control) optimization strategy.

Online adaptive control (AC) is a hardware-based method to achieve optimal and safe cutting parameters using various sensors. In online AC, cutting parameters are consistently adjusted, based on the continual measurement of cutting zone parameters with the help of sensors. Online AC senses machining conditions and changes the feedrates values in real time. AC method is appropriate for certain types of very rigid cutting tool that can handle heavy load, such as face mills or large diameter end mills. But it includes the setup problem of adaptive control apparatus [30]. Besides that, there are a number of subjects that need to be considered before deciding to use AC system [31]:

- Sensors are costly;
- Fixing the sensor close to the cutting zone is preferable, but it is very difficult,
- The sensors do not have adequate robustness to work in adverse conditions in the workspace;
- Each CNC machine requires one AC;
- Optimization is done for every part being produced;
- Retro fitment by third party is difficult.

In contrast to online AC, offline AC optimization is flexible and versatile. Offline AC does the same economically and can create output compatible to any CNC milling centre. Virtual machining packages such as VeriCUT reduce machining

time more than 50%. Therefore, virtual machining can drastically cut down NC programming time and machining time of dies, mould and aerospace parts [31]. Hence, the offline method is largely used in optimization of feedrate in surface machining processes.

2.1.2. Classification of Control Parameters and Optimization Approaches

From the literature can be concluded that feedrate scheduling consist of two stages. The first stage is the calculation of an optimized feedrate based on a reference value (reference cutting force, material removal rate (MRR), chip thickness, chip volume, etc), and the second is the modification of NC code due to the new feedrate values. Feedrate rescheduling in a sculptured surface machining consider only one constraint at all of the machining parameter such as keeping fixed chip thickness f , keeping constant surface roughness R_a , or keeping resultant cutting force (F_r). MRR, chip thickness, surface roughness, tool deflection and resultant force, these parameters can be categorized as feedrate scheduling control parameters. Different feedrate scheduling strategies have various feedrate control parameters and should be integrated for better results based on machining time and cost optimization models [32].

Recently, in feedrate scheduling related studies, the aim has been focused to obtain precise and accurate results using a combination of several feedrate rescheduling strategies. Feedrate scheduling, which is also called as feedrate optimization, is a process which changes the NC code of the machined part in order to cut at varying feedrate values in placed of fixed feedrate value. The offline method for performing optimization of cutting condition can be categorized extensively into three classifications [24]:

1. *Volumetric method*: Feedrate is proportional to either average or instantaneous material removal rate [10, 25-28].
2. *Vector force method (mechanistic)*: Feedrate is set to values which keep either average or instantaneous milling force to predetermine values [7, 20, 21, 29, 30].
3. *Rule-based method*: Which can implement also the principles of artificial intelligence technique, genetic algorithm, response surface, etc [31, 32].

2.1.3. Volumetric Based Feedrate Optimization Methods

Implementing feedrate scheduling in a free-form surface milling has become popular, and it is also used in some commercial CAM software such as MasterCAM, PowerMill, etc. Feedrate optimization strategy based on the material removal rate (MRR) is the commonly used by most researchers. Besides MRR, other geometrical information such as cross cut geometry and cut volume are also used to performed feedrate optimization. Due to the risk of simplification, MRR model is easy to apply but less accurate and precise than vector force model (mechanistic) models.

Study on feedrate optimization is initiated by Wang [34]. The aim of his study was a real-time solid modeling-based simulation of end milling for scheduling the MRR via adaptive feedrate control. The optimization system works as an offline adaptive controller before CL files are downloaded to the CNC control unit. The material removal extracted from the solid model was used to analyze the average cutting force. Relationship of the cutting force and the MRR was used based on the assumption that average cutting forces are proportional to the MRR, and then, the feedrate is automatically optimized to increase the productivity under some boundary conditions.

Similar to Wang's study, Fussel et al. [10] developed a computer system to generate feedrates that can improve the performance of CNC cutting of free-form surfaces using end milling process. Li [42] proposed an offline feedrate optimization based on MRR integrated with commercial CAD/CAM for three-axis end machining. This study offered an improve approach by relating the average power with the MRR. The machining force was predicted using empirical model after the chip parameters used to predict the cutting force was extracted. Then feedrate was adjusted to fulfill the machining requirements such as productivity, accuracy and quality. Ip et al. [36] developed a fuzzy-based MRR approach to enhance the machining performance using spindle power and specific energy. Ip [43] proposed a new MRR optimization strategy to regulate the variation of cutting speed and maintain a fixed cutting force by optimizing feedrate by taken into consideration tool life, wear and surface quality. Lan and Hsu [44] proposed a mathematical model and the decision criteria to increase the

optimal MRR control of a cutter. Chen et al. [45] proposed a feedrate optimization by considering the maximum surface roughness.

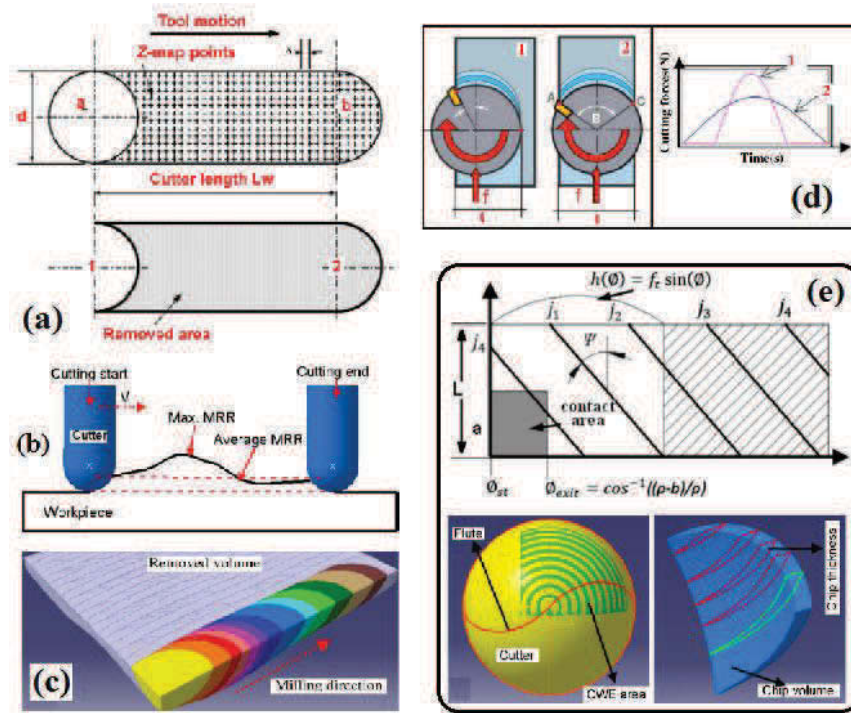


Fig. 2-2 MRR calculation method, a) using dixel space, b) average MRR vs max. MRR [46], c) removed volume [46], d) The same MRR but different force [47], e) CWE for ball-end mill and chip thickness varies as a function of engagement angle [48]

2.1.3.1. MRR Calculation Methods

The method to calculate or predict MRR in free-form surface can be categorized into three different methods. For the first method, the value of the MRR as can be seen in Fig. 2-2a must be computed for each tool movement. A_i is the dixel area, z_2 and z_1 are the z values before and after the cutting tool movement, and j is the number of dexels changed by this particular cutting tool movement:

$$V_m = \sum_{i=1}^j ((z_2 - z_1) \times A_i) \quad [cm^3] \quad (2-1)$$

$$Q = \frac{V_m}{time} = \frac{V_m}{L_w/f} \quad [cm^3] \quad (2-2)$$

where f is feedrate and Q is an average material removal rate for the time of the cutting tool movement. When the workpiece is a complex surface as illustrated in Fig. 2-2b, the average MRR may drift considerably from the peak MRR. This method is apparently not applicable for finish machining, but can be implemented in rough machining operation.

In the second method, the MRR value is calculated by defining the intersection between cutter swept volume and workpiece. This method requires to obtain the area of the cutting tool that is in contact with the workpiece and then the intersection area in the direction of the tool movement is swept as can be seen in Fig. 2-2c. This swept volume is divided by the frequency of tooth passing (t_p) to define the average MRR. The cut thickness at any tool location is calculated by dividing the scalar product of the feedrate (f) with the surface normal vector (N_s) by the number of teeth (n_t) multiplied by the cutting speed (N) [49].

$$MRR = \frac{\int h(\phi, z) dA}{t_p} \quad (2-3)$$

$$h(\phi, z) = \frac{f(\phi, z) \times N_s(\phi, z)}{n_t N} \quad (2-4)$$

This strategy was used in feedrate rescheduling method where the feedrate is created from CAM software only in the existing G-codes. The cut volume changes with the surface curvature, feedrate, and scallop height, which is produced by the previous NC tool path. The new feedrate in every NC block is generated to obtain a constant cut volume. When the travel distance in one NC block is long, a new NC block together with a new feedrate is attached in between two initial NC blocks. Feedrate scheduling is performed simultaneously with tool path verification, and its calculation time is also considered.

Both of the MRR calculation methods that were discussed use an average MRR during some limited duration introduce potential error. This error can be explained by referring to Fig. 2-2d. This figure shows two conditions where the MRR is equal but with very different force profile. In the other word, different milling forces can be generated under various conditions even with the same MRR. Fig. 2-2e shows the graph of engagement area. The instantaneous MRR is the rate which each tooth removes material, a value which briefly varies with the

position of the cutting flutes relative to the engagement area. Then the instantaneous MRR can be defined by integrating the cut thickness along each teeth that is actively intersected in the engagement area as depicted below,

$$IMRR(\theta) = \sum_1^{n_t} \int h(\phi, z) r \omega dL \quad (2-5)$$

Even in an adjusted NC code, the cut volume per tooth changes because an NC block has a numbers of rotations with a constant feedrate, however, the cutting depth per tooth changes because of the scallop height created by the previous tool path and the workpiece geometry. To obtain a constant cut volume per tooth more accurately, addition CC-points can be added within two existing NC blocks at a set number of rotations. The resultant cutting forces from feedrate optimization were rationally around the expected cut volume. Study to compare the model of cut volume per tooth and cut volume per NC block to modified the feedrate values were reported by [50, 51]

2.1.3.2. MRR Based Feedrate Scheduling Implementation

The feedrate programmed to the CNC machine is a reference input to the system. In every NC code using the geometric simulation, the volume of material removed is determined at every sampling interval, from the B-Rep of the engagement area representing the amount of material removed. The MRR can be determined and the cutting force can be predicted at every sampling interval if the cut volume is known. The optimum feedrate value is computed by [46],

$$f_{r_opt} = f_{r_current} \times \left[\frac{F_{max_limit}}{F_{predicted}} \right] \quad (2-6)$$

In the first approach, the MRR values in between two consecutive CC points were computed, and these values were used for feedrate scheduling without attaching new NC blocks. Feedrate optimization based on MRR per NC block is performed, and new feedrate is added in each existing NC block.

In the second approach, besides the reference MRR values, several parameters such as segment length, minimum distance, maximum-minimum feedrate values, etc. were considered in the feedrate scheduling process with new

additional NC blocks. In this approach, the optimum machining is obtained in two steps. First, feedrate scheduling based on the MRR is conducted, and a new feedrate is added in each existing NC block. When the feedrate and MRR value produce a significant change in between two consecutive NC blocks, a new NC block is attached to regulate the MRR between them.

In analyzing the results of MRR based approach, the feedrate reduced in regions where the MRR increased and vice versa. The MRR based feedrate optimization without adding new NC block is preferred for rough machining due to the simpler and short calculation time. Meanwhile the second approach is more suitable for semi-finish machining.

To achieve an optimum feedrate values, which are obtained through the feedrate optimization, to be applied in real machining, the capability of the machine tool interpolator is very importance. Uneven MRR means that unregulated cutting force, and hence, it will deteriorates the surface form quality. In addition to it, this condition can faster the tool wear or even tool damage. This is the reason why the constant MRR is required and, therefore it should be considered in the design of parametric NC interpolator.

2.1.4. Force-Based Feedrate Scheduling Methods

Most studies in feedrate scheduling were developed based on the volumetric analysis that commonly using the MRR value. In volumetric based approach, the machining optimization is performed simply, feedrate rise as less material being removed and reduce as more material is being removed to keep MRR fixed. Optimal feedrates, however, cannot be gained in the real operation because the physical machining force prediction is very complex when only the MRR is utilized. The vector force models are generally more accurate and precise, but they are also more difficult to integrate on the shop floor.

Force based feedrate scheduling models, which use geometrical and physical quantities, provide better results in term of machining optimization. A mechanistic cutting force prediction model for feedrate optimization is required to achieve a useful and reliable feedrate values. Cutting force optimization plays a

key role in process planning for minimizing cutting tool deflection and dynamic vibration, thereby increasing surface form quality and efficiency,

2.1.4.1. Geometric Requirement for Mechanistic Cutting Force

In the modeling and computing of the mechanistic cutting force, an accurate geometrical information is very importance. The information needed to calculate the instantaneous cut geometry consists of [6]:

1. In-cut segment of the cutting edges
2. Tool angular position
3. Cut thickness (undeformed radial chip thickness)

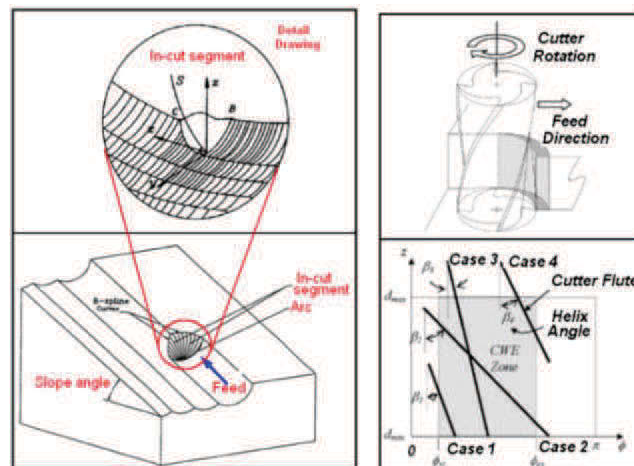


Fig. 2-3 Detailed extraction of in-cut segment [52]

There are two important items in the calculation of cutting force based mechanistic, the in-cut segment value and the cutter workpiece engagement. Precise cutter workpiece engagement and in-cut segment geometric information give direct influence on the precision of cutting force calculation. In a free-form surface machining, defining the cutter workpiece contact area are much more complex. Immersion geometry is calculated using the surface between the cutting tool and updated part geometry. In ball-end milling process, the engagement surface has three edges (AB, BC and AC) as depicted in Fig. 2-3. For every location of cutting edge motion, the engagement points between the cutting edge and the edges of the contact surface are extracted. In-cut segment is the height of these points from the cutting tool tip. The engagement boundaries (z_1 and z_u),

which are the lowermost and uppermost limits of the in-cut segment are provided by geometric simulation approach.

$$F_x, F_y, F_z = \int_{z_1}^{z_u} dF_x, dF_y, dF_z \quad (2-7)$$

2.1.4.2. Feedrate Scheduling Based on Mechanistic Cutting Forces

The offline feedrate optimization strategy manages the original constant feedrate based on the reference machining force that is set before. For the objective of enhancing the resultant cutting force to the reference value, a simple linear relation is obtained between the feedrate and the reference cutting force. It is described that a correlation between the feedrate and cutting force can be established for the selection of the most effective feedrate values for the applications of a free-form surfaces machining.

The feedrate value is simultaneously regulated by the tool path based on the computation of the cutting forces. The feedrate adjustment is initiated by loading the CL-file, after which every NC block in the CL file is simulated one by one. After calculating the milling forces in every NC block, the existing NC block of the CL file is divided into smaller blocks with optimal feedrates that adjust the peak value of the cutting forces to the reference milling force. The reference milling force is computed using the cutting tool geometry data and then the calculated machining configurations is employed to schedule the feedrate. Some studies have proposed feedrate scheduling strategy using the cutting force model in flat-end milling [1, 2, 8].

Moreover, several researchers have used feedrate scheduling for ball-end milling process. Lim and Menq [53] took cutting force and geometrical restrictions into account while concurrently regulating feedrates to optimize the machining direction in a sculptured surfaces machining. It was reported that the milling time could be significantly reduced for highly curved surfaces by cutting along the machining direction of low force-low error. However, this study did not present any experimental test for validation the proposed model. Guzel and Lazoglu [54] presented an improved theoretical model for the prediction of milling force system for a sculpture surface machining processes. This milling

force model was built upon the previous paper of Lazoglu [55]. Then the cutting force model was used in the offline piecewise variable feedrate optimizing for increasing the machining efficiency [56].

Erdim et al. [57] proposed a new analytical cutter workpiece engagement model for a monotonic free-form surfaces. They developed an offline feedrate optimization system for a sculptured surface machining based on the milling force model, which was reported upon the previous paper of Guzel and Lazoglu [54]. Moreover, authors compared the force-based feedrate optimization approaches. They concluded that force based feedrate scheduling control the cutting force magnitudes more reliable than the MRR technique. Lim and Hsiang [58] proposed a cutting path adaptive feedrate strategy, which improves the milling performance and efficiency of a sculpture surface machining when subjected to both force and dimensional tolerance constraints.

Kim et al. [59] managed the spindle speed with respect to the effective tool diameter. It depicted the realization of increasing machining efficiency in high-speed milling of sculptured surface products. Chen et al. [45] studied the feedrate optimization of high speed ball-end milling process. They found that the feed-interval scallop height is an importance parameter to limit the feedrate for high productivity machining using CBN cutting tools. Fussell et al. [60] and Jerard et al.[61] developed a feedrate optimization and selection system using a cutting force model for ball-end milling. The comparisons between the simulations and experimental results in this work showed significant inaccuracies in the prediction and regulation of machining forces. The feedrate optimization system used tool deflection, surface roughness, tool wear and machine power data to set constraints on the cutting force and the feedrate for rough, semi-finish and finish machining phases.

2.1.4.3. Force-based Feedrate Scheduling Algorithms and Implementation

The flow chart shown in Fig. 2-4 was employed to perform a feedrate scheduling using mechanistic cutting force model. The model presented in this figure was aimed to keep the resultant cutting force at the expected constant reference level along the NC tool path for every NC block. The mechanistic milling force is

computed for the existing feedrate value and compared with the reference milling force. If the difference is significant, a new feedrate value is utilized to calculate the cutting force, which is then compared with the reference force again. The new feedrate can be calculated as shown in Fig. 2-4. This step is repeated until the difference reduces within a predetermined tolerance.

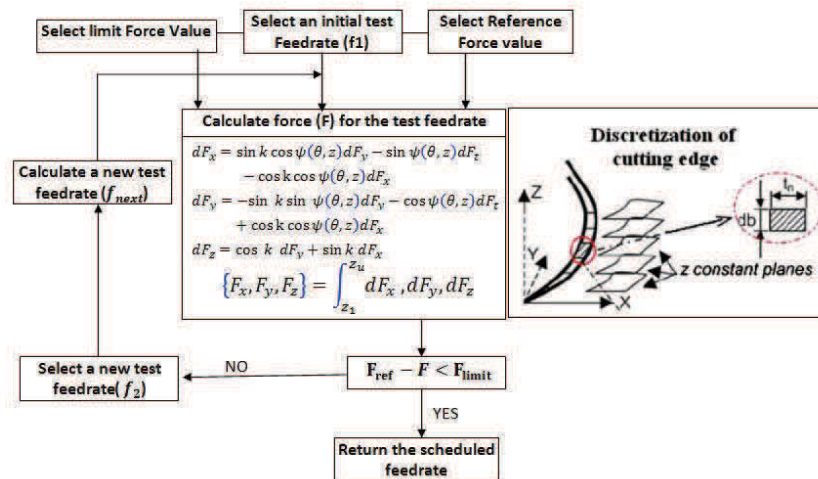


Fig. 2-4 Block diagram of feedrate adjustment based on mechanistic cutting force model [46]

Due to the cut thickness parameter is one of the most important parameters in supporting the calculation of mechanistic milling force, the flow chart in Fig. 2-4 can also be formed by selecting the cut thickness as the reference parameter. At every discrete rotational position, the cut thickness of all CWE segment is required for cutting force calculation. Consequently, the maximum cut thickness during a given cutting tool move may be obtained by storing the calculated maximum value. If the value at any tool position is obtained to exceed the maximum permissible value and the current cutting force is less than the upper limit on the acceptable force range, the feedrate iterations are stopped. The output feedrate value is then adjusted to the value that generates the maximum admissible thickness. Since there is a linear relationship between the feedrate and cut thickness at any tool position, the expected feedrate value is calculated using [62]:

$$f_{out} = f_{current} \left(\frac{h_{desired}}{h_{max}} \right) \quad (2-8)$$

f_{out} is the feedrate as an output to the updated NC block file for the current move, $f_{current}$ is the current iteration feedrate value that resulted in excessive cut thickness, $h_{desired}$ is the predetermined maximum cut thickness value and h_{max} is the maximum cut thickness computed during the current tool movement.

2.1.5. Discussion

Offline feedrate scheduling is a new methodology to automatically provide optimum feedrates for CL file modification. It has been one of the important topics in virtual machining. The two feedrate scheduling method can be compared based on several criteria such as machining tolerances and machining time. From the literature is known that volumetric method is insufficient for determining the best feedrate values. The feedrate scheduling systems used in most CAD/CAM software have limitations in creating the adjusted feedrates because they are based on the MRR [34, 35].

Since the volumetric based feedrate scheduling model does not rely on the physics of cutting tool, this deficiency makes the cutting forces not to be kept at a constant limiting level. Optimum feedrate values cannot be achieved by the operation because the mechanistic milling force prediction is very complicated when only the MRR is used. A feedrate scheduling strategy based on the cutting force prediction is thus needed to predict an effective and trustworthy feedrate. Cutting force acting on the milling tool is one of the variables that bring important milling process data [63].

Several studies [57, 64, 65] performed feedrate optimization during a free-form machining and they conclude that feedrate scheduling based on the cutting force is more precise compared with based on the MRR. The MRR based feedrate strategy tends to give higher feedrate values than that cutting force based feedrate strategy. Due to the MRR strategy is less precise; the feedrate obtained from the optimization can be excessive that can cause unwanted effect such as chipping, wear, cutter breakage or over cut due to excessive cutter deflection and dynamic run-out. MRR-based feedrate is suitable for rough milling because it is simpler and shorter calculation time. Meanwhile feedrate scheduling based force is preferred for semi finish milling because this operation needs more precise result,

even though the computational time is longer. Recently, in feedrate scheduling-related studies, the more precise and accurate results has been obtained using a combinations of different approaches such as the MRR, chip, force, acceleration and deceleration.

2.2. Geometric Modeling for Supporting Virtual Machining

Instantaneous cutting forces are calculated by the feedrate, spindle speed, and the CWE. The goal of CWE data generation is to obtain the engagement conditions between milling cutter and the in-process workpiece for supporting process modeling. For extracting the in-cut segment, CWE boundaries are intersected with the cutter edges either in 2D or in 3D Euclidian space. Then those CWE boundary and the cutter edges are mapped into two dimensional spaces. Finally, for obtaining the in-cut segments, each cutting edge is intersected with the CWE boundary in this space [8, 66]. In 3D-space approach intersections between CWE boundary and cutter edges are performed in 3D Euclidian space [52].

2.2.1. Curve (Wireframe) Modeling

Parametric as well as non-parametric curve representation is found in the literature. Parametric representation has demonstrated more advantages than non-parametric ones, especially when used in the context of engineering application, including CAD/CAM.

Curve is also divided into analytic and synthetic. The latter can represent more general and complex shapes. Synthetic curves when formulated in a certain way are very practical and suitable for design and reverse design. The requirement for synthetic curves in design arises in two occasions. First, when a curve is represented by a collection of measured data points. Second, when an existing curve must change to meet new design requirement [67].

Mathematically, a synthetic curve is used to represent a curve fitting problem to create a smooth curve that interpolates or approximates a given set of data points. Polynomials are most suitable for this task. They are easy to store, differentiate and integrate, and allow for a very practical and powerful curve

representation and design tool to be implemented. Bezier and B-spline curves are the most widely used formulations for generating synthetic curves as polynomials or piecewise continuous polynomials. They have been adopted as the standard of CAD/CAM technology and are now supported by major CAD/CAM and solid modeling packages.

Fundamentally, B-spline curves are the natural extension and generalization of Bezier ones. Indeed, they consist of piecewise continuous Bezier curves. Different degrees of continuity can be produced at the junction points. C^1 -continuity is the minimum acceptable order for curves used in engineering applications. However, C^2 -cubic B-spline is the most widely used as they allow for true 3D curves (non planar or twisted curves).

The inherent polynomial nature of Bezier, B-spline and NURBS curves can be seen in the deviation of these curves from a sequence of linear interpolation. Let P_0 and P_1 be two points in E^3 and $u \in R$, then $P_0^1(u)$ given by:

$$P_0^1(u) = (1-u).P_0 + u.P_1 \quad 0 \leq u \leq 1 \quad (2-9)$$

The operation is very simple as well as attractive from storage point of view. Because of these two points control resulting (linear) curve, they are usually called control points. For higher order polynomial, the linear interpolation can be expressed by:

$$P_0^n(u) = (1-u).P_0 + u.P_1 \quad 0 \leq u \leq 1 \quad (2-10)$$

2.2.2. Solid Modeling

A solid model is an unambiguous (complete) representation and therefore can provide enough information to be implemented, in principle, any geometric procedure. Solid modeling systems are used to model a shape having a closed volume, called a *solid*. There are many fundamental issues related to the design of a solid modeling representation and more generally, a solid modeler. In geometric modeling, E^3 subsets are the abstract geometric models used to model physical objects. However, only few subsets of E^3 are adequate models of physical solids. They are the ones that capture mathematically the following properties: 1) Rigidity;

2) Homogeneous three dimensionality; 3) Finiteness; 4) Closure under rigid motion and regularized Boolean operation; and 5) Boundary determinism [69].

Some studies in Solid model based CWE extraction for supporting process modeling have been presented by [52, 66, 70]. The CWE extraction in those studies represents the initial workpiece geometry using B-rep model. The geometric and topological algorithms of this model were used for both the in-process workpiece and CWE geometry. For updating the in-process workpiece, the swept volume of the cutter is initially generated for a given tool path segment and then this volume is subtracted from the current workpiece using regularized Boolean subtraction. The cutter workpiece engagement computation was carried out using this new workpiece state until the start of the following tool path segment. If the tool path has self engagement, then for generating the correct CWE, it need to decompose the tool path into non-engaging smaller segments. From the literature of the CWE extractions using a solid model can be categorized into two groups: 2 1/2-axis and 3-axis methods.

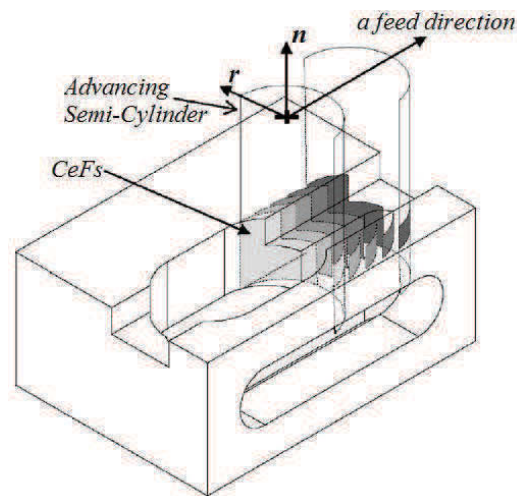


Fig. 2-5 Extraction of ceF boundary using advancing semi cylinder technique [8]

2 1/2-Axis Methods

B-rep based approach for calculating CWE in 2 1/2-axis milling with a flat-end mill has been reported by Spence et al. [8]. Later Yip-Hoi et al. [66] proposed another B-rep based method for extracting CWE in 2 1/2-axis milling. They proposed an extended method of Spence et al. [8] by performing the regularized Boolean intersection operation between a semi cylindrical cutter surface and the

in-process workpiece as shown in Fig. 2-5. In this work, they used solid modeler's (ACIS) surface/surface intersection algorithm to obtain the engagement boundary on the cutter surface. Then the engagement boundaries, which are represented by the engagement angle and the depth of cut, are mapped from 3D Euclidian space into 2D space. This information is then decomposed into smaller rectangular regions for supporting the force model as presented in [39]. This methodology can be applied to a wider range of workpiece geometries such as when the initial workpiece geometry is not rectangular prismatic. However, the method is only applicable for 2 1/2-axis with flat-end mill and the engagement boundaries are limited to straight lines and circular arcs.

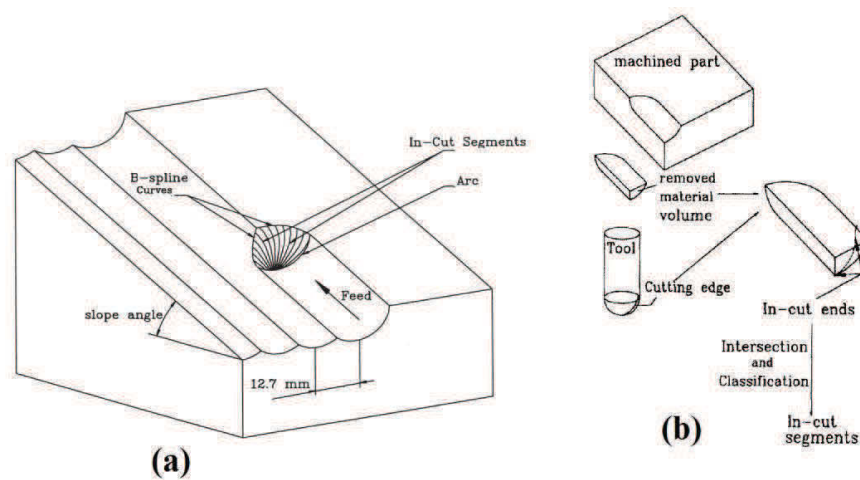


Fig. 2-6 a) Instantaneous chip geometry extraction for 3-D ball-end milling [52],
b) procedure for extracting in-cut segments of the cutting edge(s) [71]

3-axis method

Process simulation system for ball-end milling performs 2-axis or an ascending 3-axis motion has been developed by Imani et al. [52]. ACIS as geometric engine was used to model the geometric of the workpiece, the cutter and CWE. The engagement extraction is computed in two steps: first, the boundary of contact face between the spherical portion of the Ball-End mill and the in-process workpiece are obtained. This boundary consists of one circular edge and two B-spline edges as illustrated in Fig. 2-6a. For the second step, the engagement points between interpolated cutting edge and boundary curves of the contact face are determined. It is conducted using edge-edge intersections with a prescribed

tolerance. Finally the cutting edge is decomposed into in-cut and out-cut segments.

Another study was reported by El-mounayri et al. [71]. They developed a geometric approach for three-axis machining process simulation using a ball-end mill. They used solid models for representing the in-process workpiece and the removal volume. The cutting edges are represented by Bezier curves in 3D Euclidean space. The Bezier curves are intersected with the removal volume for obtaining the in-cut segments of the cutting edges as presented in Fig. 2-6b. Further, these segments are used to evaluate the instantaneous cutting forces.

2.2.3. Polyhedral Model Based Methods

Another alternative for modeling CWE that is starting to receive more attention are Polyhedral Models. Several researches [16-18] on polyhedral based CWE extraction method for supporting the process modeling have been reported. The polyhedral modeling may offer a good compromise between manageable computational speed, robustness and accuracy. These models have become pervasive in supporting engineering applications. They are found in all CAD applications as faceted models for visualization and are used extensively in simulation, CAE and rapid prototyping. In this modeling approach, workpiece surfaces are represented by a finite set of polygonal planes called facets as shown in Fig. 2-7. The most commonly used shapes are the triangles, and because of this, the term facet is usually understood to mean triangular facet. Converting the mathematically precise models to the triangulated model is called tessellation. For tessellation the original surfaces of the model are sampled for sets of points and then these points are connected for constructing triangles. The STL (Stereo lithography Tessellation Language) format for rapid prototyping is the most well-known file format for the triangulated models. In the STL model each facet is described by three vertices and a normal direction of the triangle.

Yao [16] presented a geometric algorithms for estimating cutter engagement values for three-axis ball-end milling processes of tessellated free-form surfaces. The surfaces are broken down into a series of small triangles. The CWE portion is estimated in three steps: finding the triangles that engage with the

cutter, then engaging those triangles with the cutter for obtaining the engagement curve segments, and finally employing those curve segments to create the closed engagement region.

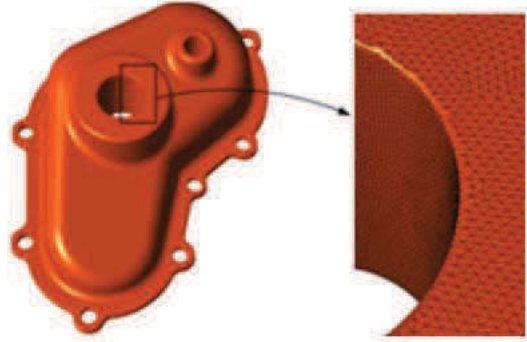


Fig. 2-7 Faceted representation of a model [17]

Later Yip-Hoi et al. [18] reported a polyhedral model based CWE computation in 2 1/2-axis and 3-axis milling. To reduce the size of data and computation time, the proposed method works on removed volumes instead of the in-process workpiece. In polyhedral model representation there is an issue about cordal error. In this case the cutter does not intersect the facets on the side wall surfaces of the removal volume. To solve this problem, they enlarged cutter radius slightly. It makes the entry angles are slightly larger while the exit angle is less than what they should be.

2.2.4. Discrete Vector Based Methods

In this method, the workpiece is broken into a set of evenly distributed discrete z direction vectors (Fig. 2-8). The length of the vectors represents the depth of the workpiece. The spacing between the vectors can be defined with regard to the desired accuracy, local surface curvature of the workpiece and size of cutting tool. The engagements are determined by finding intersections between the cutting tool geometry and vectors along the normal at discrete points on the surface. The intersections are calculated by a vector/surface intersection instead of surface/surface intersection in solid modeling.

Several studies [48, 11, 10, 72, 73] used discrete vector based method to develop the CWE extraction for supporting process modeling. Baek et al.

presented a Z-Map update method for linearly [74] and circularly [75] moving APT type tools in 3 axis milling. Machining process was simulated through numerically calculating the intersection points between the Z-Map vectors and the tool swept envelope. In this methodology, both the tool rotation axis and the z-Map vectors are restricted to lie along the vertical z-axis of a Cartesian coordinate system.

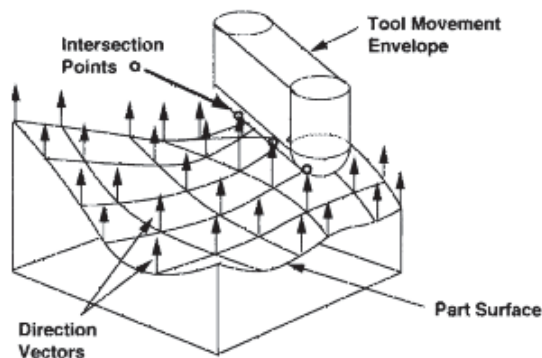


Fig. 2-8 Workpiece representation with Z Direction Vectors (ZDV) approach [11]

The vector based approach is widely used in geometric simulation. However, the accuracy of this model is largely depends on the selected grid size. Although mathematically it is more simple and shorter computation time than a solid modeler based approach. This technique suffers from inaccuracies due to the rasterization effect that commonly occurred in many discretized problems [72]. The accuracy can be improved by increasing the resolution of the grid size, but it comes with the expense of larger memory and calculation time.

2.2.5. Analytical Based Method

The numerical method has the limitation that it cannot handle very large stock parts and at the same time maintain high accuracy due to the limitations on the computational resources [28]. Few approaches have been developed using analytical techniques that do not require sampling. However, they do not work for a complex geometries. There are two main advantages of using analytical techniques. First, the functions can be extracted to determine cutter workpiece engagement at any point along the cutter path without explicitly resolving to an

expensive Boolean operation. Secondly, it is not based on numerical or sampling method, hence it is more accurate than sampling techniques.

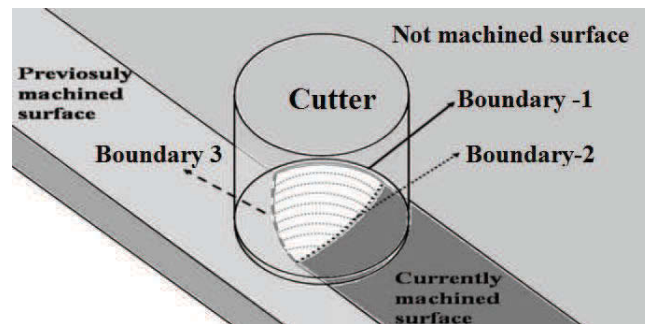


Fig. 2-9 Top, front and detail view of boundaries [22]

Gupta et al. [28] developed an analytical method for computing cutter engagement function in 2.5D machining. In this work the analytical approaches were used for determining the cutter engagement function in the case: circular cut and linear half space, and circular cut and circular half space. Ozturk and Lazoglu [22] proposed an analytical method to determine the chip load of ball-end mill during free-form machining. The chip load was obtained by defining three engagement boundary, tool entry boundary, exit boundary and workpiece surface boundary as presented in Fig. 2-9. Another study was performed by Tunc and Budak [24]. A simple analytical method called the bounding point coordinate was used. Using this method, the depth of cut in every instantaneous tool location can be predicted by defining the coordinate of cutter contact point. The tests showed that the proposed method can predict the depth of cut well.

2.2.6. Discussion

The purpose of CWE data generation is to identify the engagement condition between the cutter and the in-process workpiece during the milling operation for prediction the cutting force and further it can be used for machining optimization. From the literature, it can be seen that research work for CWE extraction can be classified into three main methods, solid modeler based approach, polyhedral based method and vector based method. There is always tradeoff between the complexity of computation and accuracy in this approach.

Solid modeling gives more accurate information on cutter workpiece engagement (CWE). 3D part model can be represented easily, precisely and accurately. But it has drawback in high computation time. The computation time drastically increased due to surface-surface intersections. The most complex CWE calculation found during free-form surface machining, especially machining in five-axis milling. Due to the surface geometry change continuously during free-form surface makes modeling CWE extraction using solid model is not so easy. On the other hand, few studies on polyhedral model based CWE extractions that have been conducted. And this method has a robustness issue in CWE extractions because of the chordal error.

Discrete vector model makes the calculation become faster than solid modeling because it is based on vector-surface intersection instead of surface-surface intersection. However, the computation time and memory consumption increases intensely as the precision and accuracy is to be improved. In free-form surface machining, determine tool workpiece engagement become much more difficult because of the complex tool path and target surface geometry. Although large studies have been reported in modeling cutter workpiece engagement, but a good compromise between manageable computational speed and accuracy is still a challenge.

From the above discussion it can be seen that comprehensive methods for extracting CWE using solid model, polyhedral mode and discrete method have been fully developed. Meanwhile few studies are discussed about analytical method. Analytical approaches for computing cutter engagement were proven much faster and more accurate compared with the discrete approaches. But they do not work for free-form surface geometries. Even though the analytical method has the advantage compare to the discrete method, but study on CWE using this method has not been well developed especially for a complex surface.

CHAPTER 3

DEFINING TOOL ORIENTATION

In three-axis NC-milling, the orientation of the tool axis is normally fixed. Consequently, complex parts with several surface orientations, requires more setups and hence longer cycle time. For machining a free-form cavities or a concave surface, ball-end cutting tools are widely used. However, the drawback of using ball-end mill is producing high scallops on a machined surface. Reducing the scallop to reach a predetermined surface quality is normally accomplished by increasing the number of cutting passes, which leads to longer machining time. Therefore, five-axis NC machines are becoming increasingly popular due to their ability to handle geometrically complex part and workpiece surface. In five-axis machining, the tool orientation relative to the workpiece can be controlled by two additional degrees of freedom that enable the possibility to position a tool freely in the available working space. It could significantly reduce the number of setup needed and hence higher machining efficiency can be achieved.

3.1. Coordinate System in Five-Axis Milling

In five-axis machining, the tool can be rotated in any direction. Part with sculptured surfaces can be machined efficiently by controlling the tool to move and rotate dynamically with respect to the part surface normal (curvatures). In order to analytically represent the moving surface generation of the cutting tool, appropriate operators for the coordinate system transformations are required. Therefore, three coordinate systems, as illustrated in Fig. 3-1, are employed to represent the position and orientation of the cutting tool. They are the workpiece coordinate system (WCS), which is the reference coordinate frame, the tool coordinate system (TCS), and the local coordinate system (LCS). The WCS is a fixed framed represented by the basis vector x , y , z , while the TCS and the LCS

are denoted by u , v , w and X , Y , Z , respectively. The tool inclination angle (α), or which is called as lead-angle by some references, and the screw angle (β), which is also called as tilt angle, are normally used when a sculptured surface part is machined using five-axis milling. They are the angles formed by the TCS and the LCS as illustrated in Fig. 3-1a.

The orientation of the cutting tool relative to WCS (ϑ) is shown in Fig. 3-1b and it is calculated using the tool rotation angles about the x -axis (θ_A) and the y -axis (θ_B),

$$\vartheta = \cos^{-1}(\cos \theta_A \cos \theta_B) \quad (3-1)$$

The operator $[M]$ to map the coordinate system from the TCS to the WCS involving the tool rotation about the x -axis, the y -axis and a translation at T is expressed as follows,

$$\begin{aligned} [M] &= \text{Rot}(X, \theta_A) \cdot \text{Rot}(Y, \theta_B) \\ &= \begin{bmatrix} \cos \theta_B & 0 & \sin \theta_B & x_T \\ \sin \theta_A \sin \theta_B & \cos \theta_A & -\sin \theta_A \cos \theta_B & y_T \\ \cos \theta_A \sin \theta_B & \sin \theta_A & \cos \theta_A \cos \theta_B & z_T \\ 0 & 0 & 0 & 1 \end{bmatrix} \end{aligned} \quad (3-2)$$

where $T(x_T, y_T, z_T)$ is the cutter location point (CL-point) that is located at the bottom center of the cutting tool. The tool coordinate frame, with orthogonal basis vector u , v , w , is defined as,

$$\begin{aligned} w &= [M] [0 \ 0 \ 1 \ 0]^T \\ &= [\sin \theta_B \quad -\sin \theta_A \cos \theta_B \quad \cos \theta_A \cos \theta_B]^T \\ v &= \frac{w \times V_T}{|w \times V_T|} ; \end{aligned} \quad (3-3)$$

$$u = v \times w$$

V_T is the linear velocity from one CC-point to the next and it is obtained by,

$$V_T = \frac{C_{C(i+1)} - C_{C(i)}}{f} ; \text{ where } (i = 1, 2, 3, \dots) \quad (3-4)$$

where $C_C(x_{C_C}, y_{C_C}, z_{C_C})$ and f denote the coordinates of the CC-point and the feedrate, respectively. To calculate the instantaneous CWE, the tool path is interpolated linearly. For linear interpolation of cutting tool movement

(translational and rotational), the intermediate position and orientation of the cutting tool in between two CC-points are defined as follows,

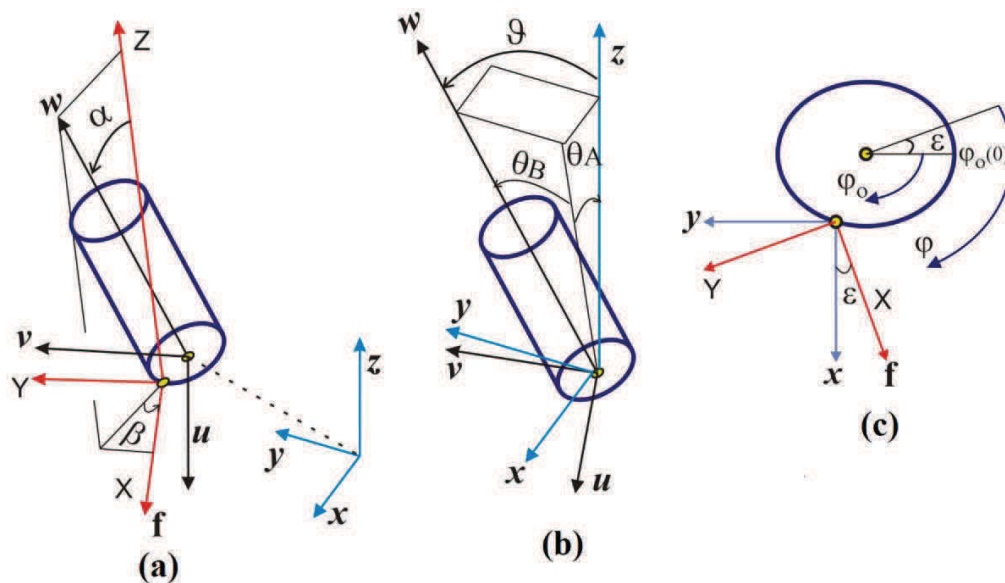


Fig. 3-1 Illustration of the relationship among the coordinate systems, (a) three coordinate systems, (b) tool orientations relative to the WCS, (c) entry angle

$$\begin{bmatrix} C_C \\ \theta_A \\ \theta_B \end{bmatrix} = \begin{bmatrix} C_{C(i)} \\ \theta_{A(i)} \\ \theta_{B(i)} \end{bmatrix} + p \begin{bmatrix} C_{C(i+1)} - C_{C(i)} \\ \theta_{A(i+1)} - \theta_{A(i)} \\ \theta_{B(i+1)} - \theta_{B(i)} \end{bmatrix} \text{ where } (0 \leq p < 1) \quad (3-5)$$

where p denotes the tool path interpolation parameter.

The tool's moving direction influences the area of the cutting tool that engages with the workpiece. In the real machining, the tool can be set to move in any direction, especially during a free-form surface machining. Therefore, the entry angle (ε), which is the displacement of the f direction from the x -axis as depicted in Fig. 3-1c, needs to be calculated as follows:

$$\varepsilon = \tan^{-1} \left[\frac{y_{C_C(i+1)} - y_{C_C(i)}}{x_{C_C(i+1)} - x_{C_C(i)}} \right] \quad (3-6)$$

where φ is the tool rotation angle or the engagement angle that is equal to $\varphi_o + \varepsilon$, and φ_o ($0 < \varphi_o < 180$) is the engagement angle when the tool moves straight on the x -axis.

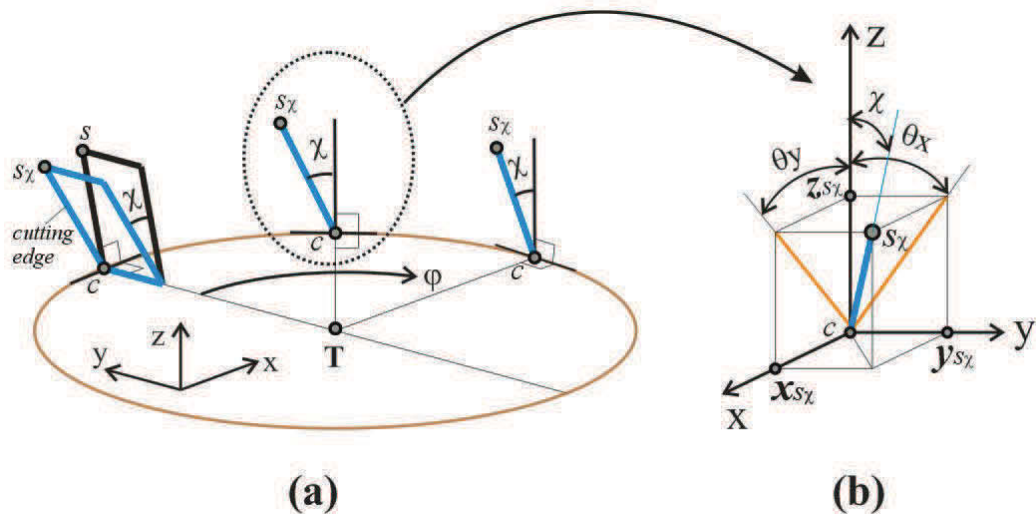


Fig. 3-2 Effect of helical angle to the cutting edge orientation with respect to the engagement angle

3.2. Effect of Helical Angle to the Tool Orientation

The milling cutters with straight teeth have disadvantage in which each edge begins to cut the material on its entire length that creating very strong efforts with a discontinuities of the load on the tool. It can be followed by the shock effect that causes vibration that is dangerous to the quality of the machined surface. For this reason, the cutter with helical angle is introduced to eliminate such problem. Helical angle (γ), which is also called lag angle in solid cutter, makes the cutting tool engages with the workpiece gradually. The existence of the helical angle makes the length of cut larger. In this section, the impact of the helical angle to the actual tool orientation will be discussed.

3.2.1. Identifying the Tool Mapping Operator and the Tool Orientation Angles during Plain Milling

When a helical angle is introduced to the cutting tool, it changes the orientation of the cutting edge. The orientation of the cutting edge is not in the same direction to the orientation of the cutting tool. By assuming that the tool moves in the X -direction, a helical angle makes the tool rotates about the Y -axis as depicted by Fig. 3-2. The actual cutting edge orientation at every engagement angel can be

determined by calculating two representative points on the cutting edge, $s_\chi(x_{s_\chi}, y_{s_\chi}, z_{s_\chi})$ and $c(x_c, y_c, z_c)$. Parametric equation of the cylindrical cutting tool is used to define the coordinate of both points. Point s_χ is point s that is rotated about the Y -axis by helical angle. Point s is an arbitrary point on the cutting edge when $\varphi = 0$, while point c is a point at the bottom of the cutting edge. Let's take the coordinate of point s and point c for a flat-end tool and a toroidal tool as follow:

$$\begin{aligned} s &= (0, R, 10) \text{ and } c = (0, R, 0) \rightarrow \text{flat-end tool} \\ s &= (0, r_m, 10) \text{ and } c = (0, r_m, 0) \rightarrow \text{toroidal tool} \end{aligned} \quad (3-7)$$

where R and r_m denote the radius and minor radius of cutting tool, respectively. Then the coordinate of point s_χ and point c with respect to the engagement angle are defined by performing transformation about the Z -axis. Therefore, the both transformations, about the Y -axis (helical angle) and the Z -axis (engagement angle), are expressed as follows,

$$\begin{aligned} s_\chi &= \text{Rot}(Z, \varphi) \cdot \text{Rot}(Y, \chi) \cdot [s] \\ s_\chi \begin{bmatrix} x_{s_\chi} \\ y_{s_\chi} \\ z_{s_\chi} \end{bmatrix} &= \begin{bmatrix} \cos \varphi & -\sin \varphi & 0 \\ \sin \varphi & \cos \varphi & 0 \\ 0 & 0 & 1 \end{bmatrix} \begin{bmatrix} \cos \chi & 0 & \sin \chi \\ 0 & 1 & 0 \\ \sin \chi & 0 & \cos \chi \end{bmatrix} \begin{bmatrix} x_s \\ y_s \\ z_s \end{bmatrix} \end{aligned} \quad (3-8)$$

$$\begin{aligned} c &= \text{Rot}(Z, \varphi) \cdot [c] \\ c \begin{bmatrix} x_c \\ y_c \\ z_c \end{bmatrix} &= \begin{bmatrix} \cos \varphi & -\sin \varphi & 0 \\ \sin \varphi & \cos \varphi & 0 \\ 0 & 0 & 1 \end{bmatrix} \begin{bmatrix} x_c \\ y_c \\ z_c \end{bmatrix} \end{aligned} \quad (3-9)$$

The mapping operator is determined by calculating the cutting edge rotation angles about the X -axis and the Y -axis as depicted in Fig. 3-2b. They are calculated as follows,

$$\begin{aligned} \theta_{A_x} = \theta_x &= \tan^{-1} \left(\frac{y_{s_\chi} - y_c}{z_{s_\chi}} \right) \\ \theta_y &= \tan^{-1} \left(\frac{x_{s_\chi} - x_c}{z_{s_\chi}} \right) \end{aligned} \quad (3-10)$$

$$\theta_{B\chi} = \tan^{-1} \left(\frac{(x_{s\chi} - x_c) \cos \theta_x}{z_{s\chi}} \right) = \tan^{-1} (\tan \theta_y \cos \theta_x)$$

The cutting edge orientation relative to the Z -axis in WCS, as expressed in Eq.(3-1), yields to,

$$\vartheta_\chi = \cos^{-1} (\cos \theta_{A\chi} \cos \theta_{B\chi}) \quad (3-11)$$

During plain cutting ($\theta_A = \theta_B = 0$), the orientation angle of the cutting edge at every engagement angle are equal to the helical angle ($\vartheta = \chi$). The mapping operator when a helical angle exist with respect to $\theta_{A\chi}$ and $\theta_{B\chi}$ is expressed by,

$$[M]_h = \text{Rot}(X, \theta_{A\chi}) \cdot \text{Rot}(Y, \theta_{B\chi})$$

$$[M]_h = \begin{bmatrix} \cos \theta_{B\chi} & 0 & \sin \theta_{B\chi} \\ \sin \theta_{A\chi} \sin \theta_{B\chi} & \cos \theta_{A\chi} & -\sin \theta_{A\chi} \cos \theta_{B\chi} \\ -\cos \theta_{A\chi} \sin \theta_{B\chi} & \sin \theta_{A\chi} & \cos \theta_{A\chi} \cos \theta_{B\chi} \end{bmatrix} \quad (3-12)$$

3.2.2. Identifying the Tool Mapping Operator and Tool Orientation Angles during Free-Form Milling

The characteristic of a free-form milling is the tool can be oriented in any direction. The tool orientation is defined using the tool orientation angles, θ_A and θ_B . When a helical angle exists, the orientation angles of the cutting edge is changed. Once again, the actual cutting edge rotation can be determined with the aid of point s_χ and point c . To obtain the coordinate of point s_χ and point c as shown in Fig. 3-2, they are rotated by θ_A and θ_B . Then, Eq.(3-8) and Eq.(3-9) changed to become,

$$s_\chi(x_{s\chi}, y_{s\chi}, z_{s\chi}) = \text{Rot}(X, \theta_A) \cdot \text{Rot}(Y, \theta_B) \cdot \text{Rot}(Z, \varphi) \cdot \text{Rot}(Y, \chi) \cdot [s] \quad (3-13)$$

$$c(x_c, y_c, z_c) = \text{Rot}(X, \theta_A) \cdot \text{Rot}(Y, \theta_B) \cdot \text{Rot}(Z, \varphi) \cdot [c] \quad (3-14)$$

Once point s_χ and point c are determined, all of the cutting edge orientations ($\theta_x, \theta_y, \theta_{A\chi}, \theta_{B\chi}, \vartheta$) and the mapping operator are defined using Eq.(3-10) – Eq.(3-12).

3.3. Cutting Tool Geometry and Selection in Five-Axis Milling

According to APT (automatically programmed tools) definition [77], milling cutter is composed of four parts: cylinder, upper cone, lower cone and corner torus as shown in Fig. 3-3a. The geometric definition and mathematical description of the generalized cutter are presented below [78],

r : the cutter radius

r_t : the cutter corner radius

l : the distance between the cutter tip and the pivot point along the cutter axis

e : the radial distance from the cutter axis to the cutter corner center

h : the distance from the cutter tip to the length of the cutter arbor along the cutter axis

l_k : the length of the cylinder part, denote corner torus center as measured

α_t : the angle from a radial line through the cutter tip to the cutter bottom, ($0 \leq \alpha_t \leq 90$)

β_t : the tap angle between the cutter side and the cutter axis ($-90 \leq \beta_t \leq 90$)

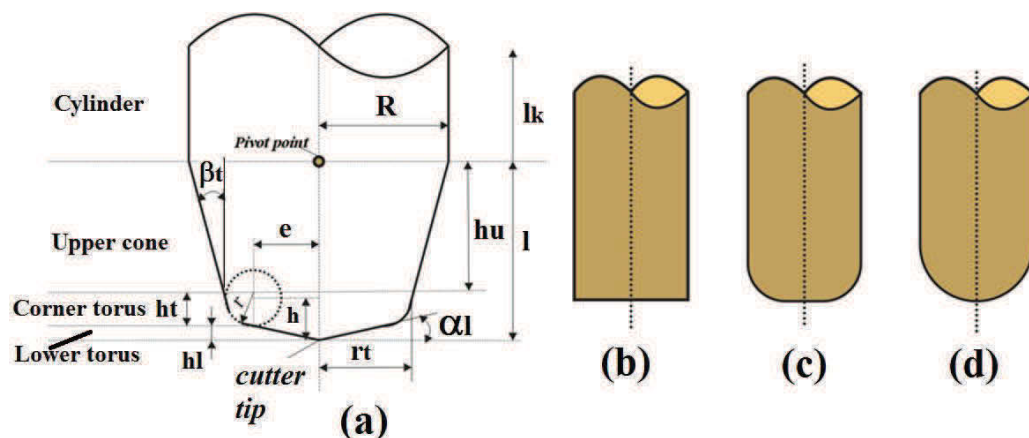


Fig. 3-3 Cutting tool geometry, (a) generalized cutting tool model based on APT, (b) flat-end tool, (c) toroidal tool, (d) ball-end tool

Selecting a milling cutter is not a simple task. There are many variables that need to be considered. But essentially the machinist is trying to choose a tool that cut the material to the required specification for the least cost. Many types of

cutting tool geometry that can be used in five-axis milling operation. Among them, however, three cutting tool types in term of geometry are commonly used: flat-end cutting tool, toroidal cutting tool and ball-end cutting tool as depicted in Fig. 3-3.

These types of tools have been studied for the effectiveness in the machining of sculptured surfaces [79-84]. The studies showed that, with the same tool inclination angle, a flat-end tool results in the smallest scallop height compared with a toroidal and a ball-end tools. The scallop height does not vary with the inclination angle when cutting using a ball-end tool, while it is significantly reduced for a toroidal tool at small inclination angles. In more detail, a flat-end tool even gives more scallop height reduction than the toroidal tool with the same inclination angle. The higher the corner radius of a toroidal tool, the higher the scallop height is, and vice versa.

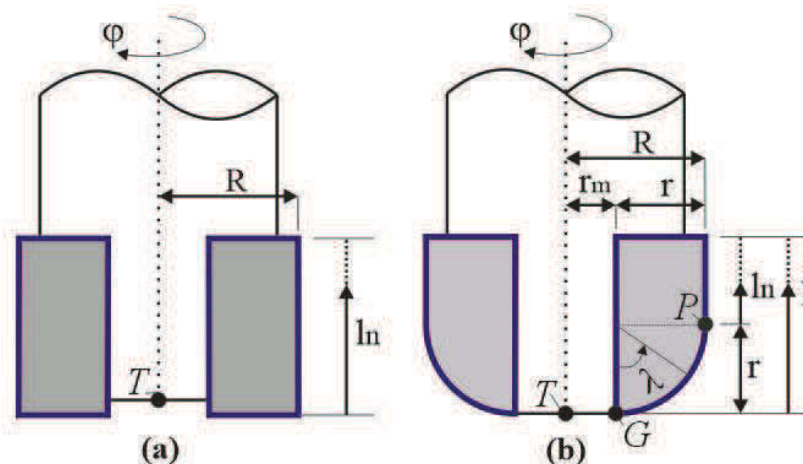


Fig. 3-4 The geometry of cutting tool, a) flat-end cutter, b) toroidal cutter

One of the critical problems in five-axis milling is the positioning of the tool in relation to the surface to be machined without having problems of undercut or overcut (gouging) [81]. To avoid these problems, traditionally, ball-end tools are used by preference. However, an important drawback of ball-end tools is the varying cutting speed along the tool tip; a poor surface roughness is the result. Therefore, a specified inclination angle larger than zero must be applied. On the other hand, the generated roughness when cutting using a flat-end tool has similar tendency as a toroidal tool. For this tool, the best roughness is obtained at the zero

inclination angle, and it becomes worse when increasing. A flat-end tool results in higher surface roughness than a toroidal tool.

From the above discussion, a toroidal tool and a flat-end tool are preferred to a ball-end tool, not only for roughing but also for semi finishing and finishing operation. In practice, the use of a flat-end tool is common due to its simplicity for gouging avoidance and calculating the preferred inclination angle for a sculptured surfaces as done by [85, 89].

3.3.1. Parametric Equation of Flat-End and Toroidal Cutting Tool

According to APT tool geometry in section 3.3, flat-end cutter can be defined as follows: $\beta_t = \alpha_l = r = h = e = 0$. This tool is universally applicable for roughing, semi-finishing and finishing operation. The geometry of flat-end tool is presented in Fig. 3-4a. The surface of a flat-end cutter is considered as a cylindrical surface and is defined by a parametric equation as follows,

$$S_C(\varphi; l) = \begin{bmatrix} R \sin \varphi \\ R \cos \varphi \\ l_n \end{bmatrix} ; 0 < l_n < l \quad (3-15)$$

where R is the radius of cutting tool, φ is the tool rotation angle or the engagement angle and l_n is the distance of a point on the cutting edge, which is measured from the bottom of cutting edge, and used to calculate the length of cut.

Meanwhile for a toroidal cutter, it can be described by referring to APT as follows: $\beta_t = \alpha_l = 0$; $r = h \neq 0$; $e = r_t$. The generic toroidal-end cutter is decomposed into cylindrical and toroidal parametric surfaces. The representation of the cylindrical surface with respect to the tool coordinate system (TCS) is described using Eq.(3-15) with $l_n = r + l$, while for the toroidal surface is defined by the following equation,

$$S_T(\varphi; \lambda) = \begin{bmatrix} (r_m + r \sin \lambda) \sin \varphi \\ (r_m + r \sin \lambda) \cos \varphi \\ r - r \cos \lambda \end{bmatrix} \text{ where } 0 < \lambda < 90 \quad (3-16)$$

where r is the minor radius of the cutter, r_m is the distance between the cutter centre point to the minor radius, and λ denotes the toroidal angle. Due to the cutter

location (CL) data and the workpiece surface information are provided in the workpiece coordinate system (WCS), the cutter surfaces are transformed from the TCS to the WCS.

$$S_C'(x'_{S_C}, y'_{S_C}, z'_{S_C}) = [M] S_C(\varphi; l) \quad (3-17)$$

$$S_T'(x'_{S_T}, y'_{S_T}, z'_{S_T}) = [M] S_T(\varphi; \lambda) \quad (3-18)$$

3.3.2. Effect of a Helical Angle to the Shape of Swept Surface

For a solid cutting tool, the shape of the swept surface, whether it is with or without a helical angle, is always similar. A different condition is found when a non-solid cutting tool (index-able milling tool) is used. The helical angle gives an effect to the swept surface. As depicted in Fig. 3-5, when a helical angle exist, the tool radius at the bottom side is different to the one at the upper side (R_χ). The radius of the cutting tool equal to R is only located at the bottom side. The tool radius increases as increasing the tool height (l). Therefore, the radius of the swept surface as a function of axial depth of cut, $R_{\chi(l)}$, is expressed as follows,

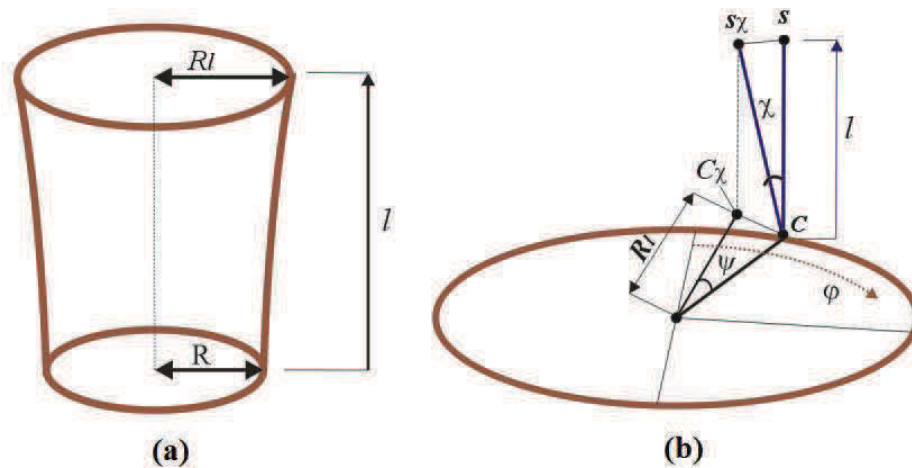


Fig. 3-5 Swept surface of flat-end tool with helical angle

$$\psi_c = \tan^{-1}((l_n \sin \chi)/R) \quad (3-19)$$

$$R_{\chi(l)} = R / \cos \psi_c \quad (3-20)$$

where ψ_C is the lag angle. The lag angle is the engagement angle of s_χ relative to the engagement angle of s . Then the parametric equation of swept surface for a helical flat-end tool is defined as follows,

$$S_{C_\chi}(\varphi; l) = \begin{bmatrix} R_\chi \sin \varphi \\ R_\chi \cos \varphi \\ l_n \cos \chi \end{bmatrix} \text{ where } 0 < l_n < l \quad (3-21)$$

For a helical toroidal cutting tool, the radius of cutting edge as a function of axial depth of cut is determined using the following equations,

$$\psi_T = \tan^{-1}(((r - r \cos \lambda) \sin \chi) / (r_m + r \sin \lambda)) \quad (3-22)$$

$$R_\chi(\lambda) = (r_m + r \sin \lambda) / \cos \psi_T \quad (3-23)$$

$$S_{T_\chi}(\varphi; \lambda) = \begin{bmatrix} R_\chi \sin \varphi \\ R_\chi \cos \varphi \\ (r - r \cos \lambda) \cos \chi \end{bmatrix} \text{ where } 0 < \lambda < 90 \quad (3-24)$$

The cylindrical surface of a helical toroidal cutter is defined using Eq.(3-19) - Eq.(3-21) with $r < l_n < l$.

3.4. Conclusion

Three coordinate systems used in the model development have been defined in this chapter. The equations to map the coordinate system were developed. The algorithm to calculate the tool orientation angles relative to the WCS was presented. The effect of helical angle, inclination angle and screw angle were taken into account in the method development. The existence of helical angle makes the orientation of the cutting edge is not in the same direction with that of cutting tool. Finally, the parametric equations to define the surface of the cutting tools have been determined. These equation will be used in the next chapter in defining the coordinate of the Le-point and UE-point.

CHAPTER 4

ANALYTICAL METHOD FOR OBTAINING THE LE-POINT AND THE UE-POINT FOR ROUGH AND SEMI-FINISH MILLING

There are generally three main stages in the high speed machining of dies/mould machining: rough milling, semi-finish milling and finish milling. In order to perform a complete process simulation of a given machining cycle, the CWE model for all of machining stages will be derived. The characteristic of the workpiece surface and the tool orientation in each stage may be different. The tool paths of a five-axis milling are generated in computer aided manufacturing (CAM) software resulting in continuously varying tool orientation and the CWE. Due to the complex surface geometry, the engagement between the cutting tool and the workpiece vary continuously, especially in roughing and semi finishing operation. Therefore, a different method will be applied for each machining stages.

The method to determine the orientation of the cutting tools with respect to the WCS and the TCS have been defined in the previous chapter. The effect of helical angle to the tool orientation was comprehensively discussed. In this chapter, the method to calculate the cutter workpiece engagement points, LE-point and the UE-point, will be discussed. The discussion will be only focused on roughing and semi-finishing milling. For a complex workpiece surface, which is normally performed during finish milling, will be discussed in the next chapter.

During rough milling, the workpiece surface is represented by the coordinate of points (vertex) that are located on the wall surface. Meanwhile vertical vectors are used during semi finish milling with straight staircase profile. For semi finish milling with non-straight staircase profile, the shape of the wall surface is represented by a number of discrete points. All the surface data are

assumed provided (given) and the method to obtain the discrete data will not be discussed in this study.

4.1. Calculating the Geometry of Cut

One of the objective of CWE calculation is to determined the geometry of cut. This information can be used to support the method to predict the instantaneous cutting force. The equation to calculate the geometry of cut for toroidal and flat end cutter will be derived in this section. The geometry of cut involving the length of cut, the depth of cut and the cut thickness, are calculated using variables of the engagement points: the length of CWE on the cylindrical side (l_n), the toroidal angle of the LE-point (λ_c), and the toroidal angle of the UE-point (λ_n). The method to obtain these variables will be discussed in the following sections.

For a flat-end cutting tool without neither helical angle nor inclination angle, the axial depth of cut (D) and the length of cut (L) are equal, and they are expressed by,

$$D = L = l_n \quad (4-1)$$

The length of cut is always equal to l_n whether the tool is set with or without both the helical angle and the inclination angle. On the other hand, the axial depth of cut of a toroidal cutting tool is always different with the length of cut in spite of the helical angle and the inclination angle do not exist. It is occurred because of its toroidal side. The axial depth of cut is calculated as follows,

$$D = r - r \cos \lambda_n + l_n \quad (4-2)$$

where λ_n is the toroidal angle of the UE-point. And the length of cut is determined as follows,

$$L = (\lambda_n/180)\pi R + l_n \quad (4-3)$$

In this study, the axial depth of cut is measured along the surface normal axis. Therefore, when the inclination angle exists, then it makes the axial depth of cut smaller. The word “smaller” is used because the length of cut is determined first, then the axial depth of cut is calculated by referring to the length of cut.

When the cutting tool has a helical angle, then Eq.(4-1) and Eq.(4-3) are also applicable to calculate the length of cut. Meanwhile the axial depth of cut is expressed as follows,

$$\begin{aligned} D &= l_n \cos \chi \rightarrow (\text{flat-end}) \\ D &= (r - r \cos \lambda_n + l_n) \cos \chi \rightarrow (\text{toroidal tool}) \end{aligned} \quad (4-4)$$

When the cutting tool with the inclination angle but without the helical angle, then the length of cut is defined as follows,

$$\begin{aligned} L &= l_n + l_b \rightarrow (\text{flat-end}) \\ L &= [(\lambda_n - \lambda_c)/180]\pi R + l_n + l_b \rightarrow (\text{toroidal tool}) \end{aligned} \quad (4-5)$$

The axial depth of cut is expressed using the following equations,

$$\begin{aligned} D &= l_n \cos \alpha \rightarrow (\text{flat-end}) \\ D &= (r (\cos \lambda_c - \cos \lambda_n) + l_n) \cos \alpha \rightarrow (\text{toroidal tool}) \end{aligned} \quad (4-6)$$

In five-axis milling, there is a possibility that the helical angle and the inclination angle are used together. When it is occurred, then the cut geometry can be defined after the orientation angle of the cutting edge with respect to the helical angle and inclination angle is determined. The orientation angle (ϑ_D) is determined using the method to obtain the cutting edge orientation in section 3.2. Then the representative points as expressed in Eq.(3-13) and Eq.(3-14) yield to,

$$s_\chi(x_{s_\chi}, y_{s_\chi}, z_{s_\chi}) = \text{Rot}(Y, \alpha) . \text{Rot}(Z, \varphi) . \text{Rot}(Y, \chi) . [s] \quad (4-7)$$

$$c(x_c, y_c, z_c) = \text{Rot}(X, \theta_A) . \text{Rot}(Y, \theta_B) . \text{Rot}(Z, \varphi) . [c] \quad (4-8)$$

Eq.(3-10) and Eq.(3-11) are then used to obtain the orientation angle relative to the surface normal. Once the cutting edge orientation was determined, the axial depth of cut is defined by,

$$\begin{aligned} D &= l_n \cos \vartheta_D \rightarrow (\text{flat-end}) \\ D &= (r - r \cos(\lambda_n - \lambda_c) + l_n) \cos \alpha \rightarrow (\text{toroidal tool}) \end{aligned} \quad (4-9)$$

The cutting force prediction model is performed based on the cut area generated at an instantaneous tool location. Before the cut area is calculated, the cut thickness need to be determined. According to Kumanchik and Schmitz [90], the cut thickness in a milling operation is defined as the distance between the

current tooth path and the previous tooth path along the line segment that connects the tool center to the current tooth cutting edge. However, this definition is only applicable for machining with a perpendicular tool orientation. Inclination angle should be taken into consideration, it can influence the size of the cut thickness. The tool inclination angle makes the cut thickness smaller than the distance of two consecutive tooth paths. Therefore, the cut thickness (h) is expressed as a function of the engagement angle as follows,

$$h = f \cos \alpha \sin \varphi \quad (4-10)$$

Finally, the cross cut area as a function of the engagement angle is calculated by multiplying the cut thickness by the length of cut.

$$A_{(\varphi)} = L_{(\varphi)} \cdot h_{(\varphi)} \quad (4-11)$$

4.2. Obtaining the LE-Point

As mentioned in the introduction that the length of cut is determined by defining two engagement points, the LE-point (C_f) that is located at lower side of CWE, and the UE-point that is located at the upper side of CWE. In this section, the method to determine the coordinate of the LE-point (C_f) is developed. Erdim et al. [57] mentioned that, when the cutter moves upwards or downwards with a feed inclination angle, as in upward (positive inclination angle) and downward (negative inclination angle) ramping, the feed direction vector is not perpendicular to the cutter rotation vector, and the cutting edge element produces different undeformed chip geometry. Gani et.al [91] mentioned that the tool inclination in five-axis milling has a large influence on the cross cut geometry. It will not only change the chip thickness, but also the length of cut. In term of cutting force, previous studies [57, 92] showed that a negative inclination angle tend to give higher cutting force. It is believed due to the larger contact area between the cutter and the workpiece.

4.2.1. Identifying the LE-Point and the Length of Bottom CWE of a Flat-End Cutting Tool

The LE-points of a flat-end cutting tool with respect to the inclination angle and as a function of the engagement angle are illustrated in Fig. 4-1. It can be seen that the tool without the inclination angle ($\alpha = 0$) and the tool with a positive inclination angle ($\alpha > 0$) have the LE-point in the same location. In these cases, the LE-points are located at the bottom of front side of cutting tool. The coordinate of the LE-point is calculated using the parametric equation of a cylindrical cutting tool as presented in Eq.(3-17), and it yields to,

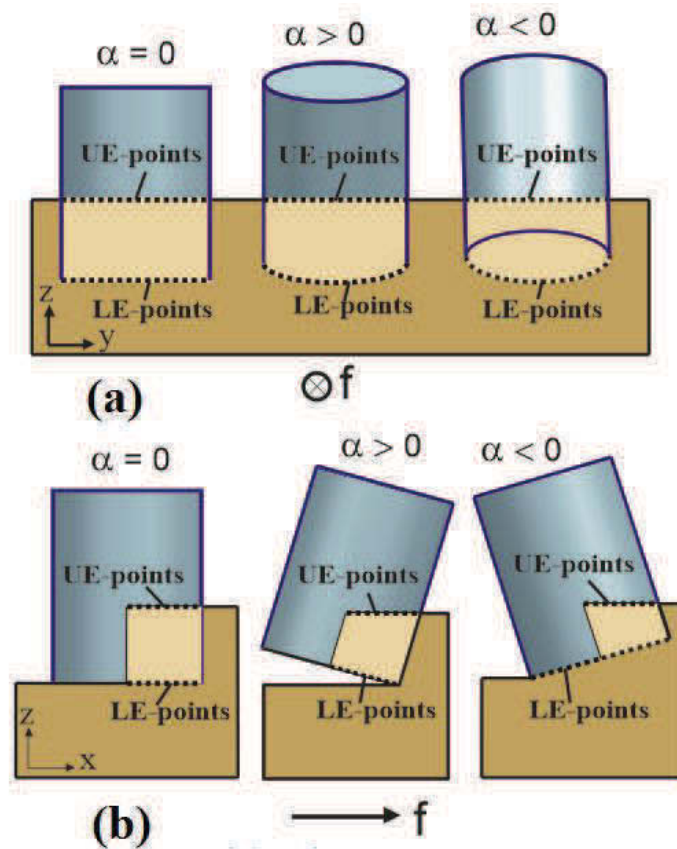


Fig. 4-1 Effect of inclination angle to the CWE region in flat-end tool,
(a) front view, (b) side view

$$C_f(x_{C_f}, y_{C_f}, z_{C_f}) = [M]S_C(\varphi; 0) + T \quad (4-12)$$

A different case is depicted by the tool with negative inclination angle ($\alpha > 0$). The CWE is not only occurred on the front cutting edge, but also on the

back cutting edge at the bottom side. In this case, the CWE is divided into two sections: the first section is the upper side of front cutting edge, which is located in between the UE-point (n_f) and the LE-point of front cutting edge (C_f). This section is called the front CWE (l_f). The second section is located at the bottom side of both front and back cutting edge, which is in between C_f to the LE-point of back cutting edge (C_b), or it is called as the bottom CWE (l_b). The existence of bottom CWE is depend on the number of cutting teeth, cutting edge geometry at the bottom side, and the engagement angle. The engagement angle of the back cutting edge (φ_b) is calculated as follows,

$$\varphi_b = \varphi + 180 \left(\frac{n_t + |\sin(90 \times n_t)|}{n_t} \right); \text{ where } \varphi_b \in \{180, 360\} \quad (4-13)$$

where n_t denotes the number of cutting teeth. Then, the coordinate of C_b is calculated using Eq.(4-12) with $\varphi = \varphi_b$. Meanwhile the length of the bottom CWE is a summation of the length of front and back cutting edge at the bottom side (r_t).

$$l_b = 2 r_t \quad (4-14)$$

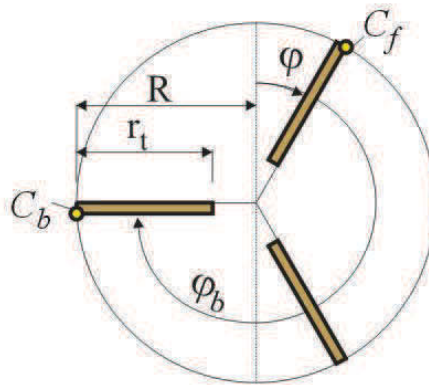


Fig. 4-2 Bottom view of flat cutting tool

4.2.2. Identifying the LE-Point and the Length of Bottom CWE for Toroidal Cutting Tool

The LE-points of a toroidal cutting tool with respect to the inclination angle and as a function of the engagement angle are depicted in Fig. 4-3. Identifying the

coordinate of C_f for the tool without the inclination angle ($\alpha = 0$) is relatively simple. In such condition, C_f is located at the bottom of the front cutting edge as shown in Fig. 4-3. In this case, the mapping of parametric equation of the toroidal cutting tool in Eq.(3-18) is used to defined the coordinate of LE-point, and it yields to,

$$C_f(x_{C_f}, y_{C_f}, z_{C_f}) = [M] S_T(\varphi; 0) + T \quad (4-15)$$

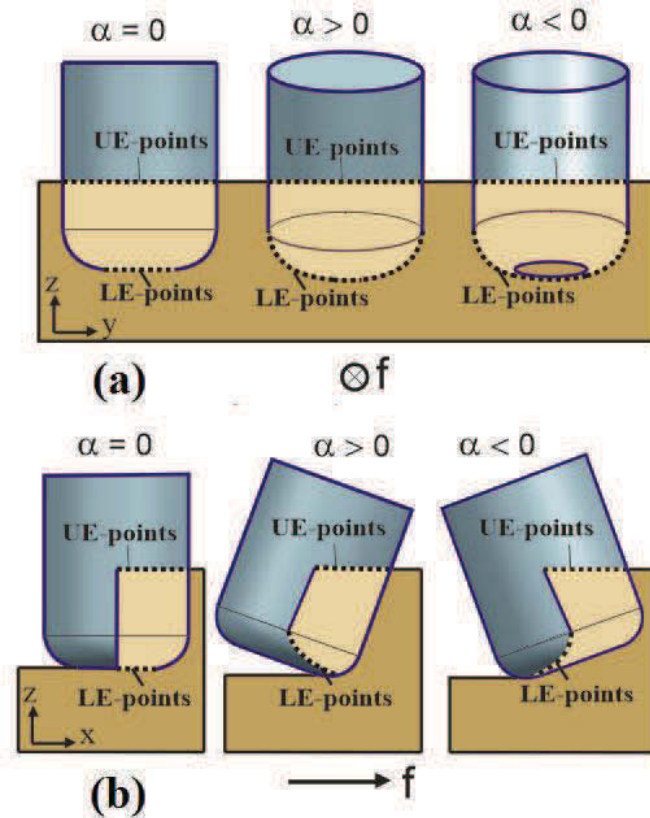


Fig. 4-3 Effect of an inclination angle to the CWE region in toroidal tool,
(a) front view, (b) side view

When the tool inclination angle exists, it changes the location of the LE-point. As can be seen in Fig. 4-3, when $\alpha > 0$, the LE-point is located at the front cutting edge with $\lambda > 0$. While if $\alpha < 0$, the LE-point is located at the back cutting edge with $\lambda > 0$. Bottom view of the lower engagement point for negative inclination angle is depicted in Fig. 4-4. In this case, C_f is determined using Eq.(4-15) with $\lambda = 0$.

The method to define the LE-point was derived using the method to define a swept envelope. As mentioned in other studies [93-95], a swept envelope is constructed by three points: the forward boundary (*egress point*), the envelope boundary (*grazing point*) and the backward boundary (*ingress point*). The *grazing point* is considered as the LE-point at every engagement angle. It is obtained using the tangency function $F_{(\vartheta,\varphi,p)} = N_{S_T(\vartheta,\varphi,p)} \cdot V_{S_T(\vartheta,\varphi,p)} = 0$, which consists of the cutter surface normal $N_{S_T(\vartheta,\varphi,p)}$ and the cutter moving vector $V_{S_T(\vartheta,\varphi,p)}$. Using the same method, the toroidal angle of the LE-points at every engagement angle are calculated. Even though the toroidal cutter is constructed by two surfaces, toroidal side and cylindrical side, the LE-point is always located on the toroidal surface. When the inclination angle is negative, the engagement angle used in the calculation is the engagement angle of the back cutting edge ($\varphi = \varphi_b$). The method to define φ_b (Eq.(4-13)) for a flat-end tool can also be used for a toroidal cutter.

The surface normal of an arbitrary point Q on toroidal surface in the TCS is described by,

$$N_{S_T} = \frac{\partial S_T / \partial \lambda}{|\partial S_T / \partial \lambda|} \times \frac{\partial S_T / \partial \varphi}{|\partial S_T / \partial \varphi|} = \begin{bmatrix} \sin \lambda \cdot \cos \varphi \\ \sin \lambda \cdot \sin \varphi \\ -\cos \lambda \end{bmatrix} \quad (4-16)$$

When Eq.(4-16) is transformed to a moving frame, it yields to,

$$N_{S_T'(\vartheta,\varphi,p)} = \sin \lambda \cdot \cos \varphi \cdot u + \sin \lambda \cdot \sin \varphi \cdot v - \cos \lambda \cdot w \quad (4-17)$$

The velocity of an arbitrary point Q on the toroidal surface is determined as follows,

$$V_{S_T} = V_T + \omega \times \overrightarrow{TQ} \quad (4-18)$$

where ω and \overrightarrow{TQ} denote the angular velocity and the position vector from T to Q , respectively. Because the tool orientations for any instantaneous position was adjusted in Eq.(3-5), it is assumed that $\omega = 0$. Therefore, the velocity vector in Eq.(4-18) is equal to V_T and the tangency function is as follows,

$$F_{(\vartheta,\varphi,p)} = \sin \lambda \cdot \cos \varphi \cdot (V_T \cdot u) + \sin \lambda \cdot \sin \varphi \cdot (V_T \cdot v) + \cos \lambda \cdot (V_T \cdot w) = 0 \quad (4-19)$$

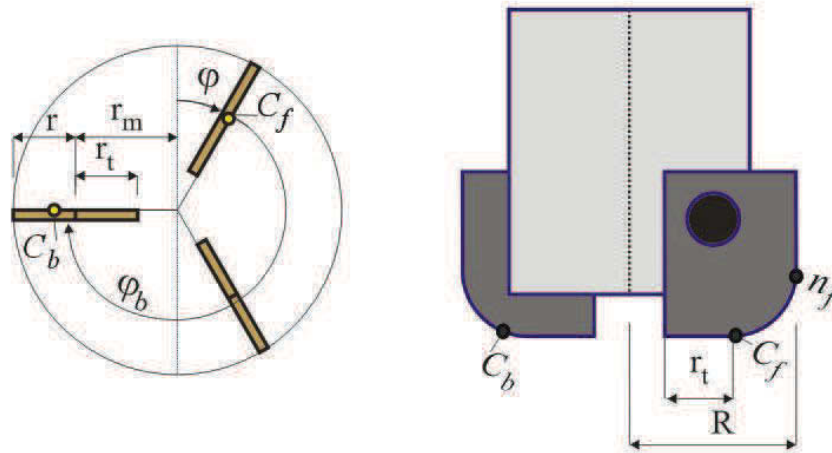


Fig. 4-4 Geometry of cutting tool at the bottom side,
(a) bottom view, (b) front view

Finally, the toroidal angle of the LE-point as a function of engagement angle is calculated as follows,

$$\lambda_c = \tan^{-1} \left[\frac{V_T \cdot w}{\cos(\varphi) \cdot (V_T \cdot u) + \sin(\varphi) \cdot (V_T \cdot v)} \right] \quad (4-20)$$

By adding $|\lambda_c|$ and φ into Eq.(4-15), then the coordinate of LE-points are obtained. The length of bottom CWE is a summation of the length of front and back cutting edge at the bottom side (r_t) and the CWE at toroidal side of back cutting edge and it is expressed as follows,

$$l_{b(\varphi_b)} = 2 r_t + (|\lambda_c| \pi r) / 180 \quad (4-21)$$

4.2.3. Application and Discussion

Based on the formulae derived in the previous sections, a simulation program to define the coordinate of LE-point was developed using MATLAB. The tests were performed to check the effect of several variables to the location of the LE-point. A toroidal cutter with diameter 20 mm and a minor radius 5 mm was used to test the effect of an inclination angle to the location of LE-point and the length of cut. It can be seen in Fig. 4-5a that the inclination angle gives a significant effect to the LE-point. A negative inclination angle makes the LE-point located at the back

cutting edge. The minus sign (-) for toroidal angle with negative inclination angle, as shown in Fig. 4-5a, was aimed to indicate that the LE-point is located at the back cutting edge. Increasing inclination angle tends to increase the toroidal angle of LE-point.

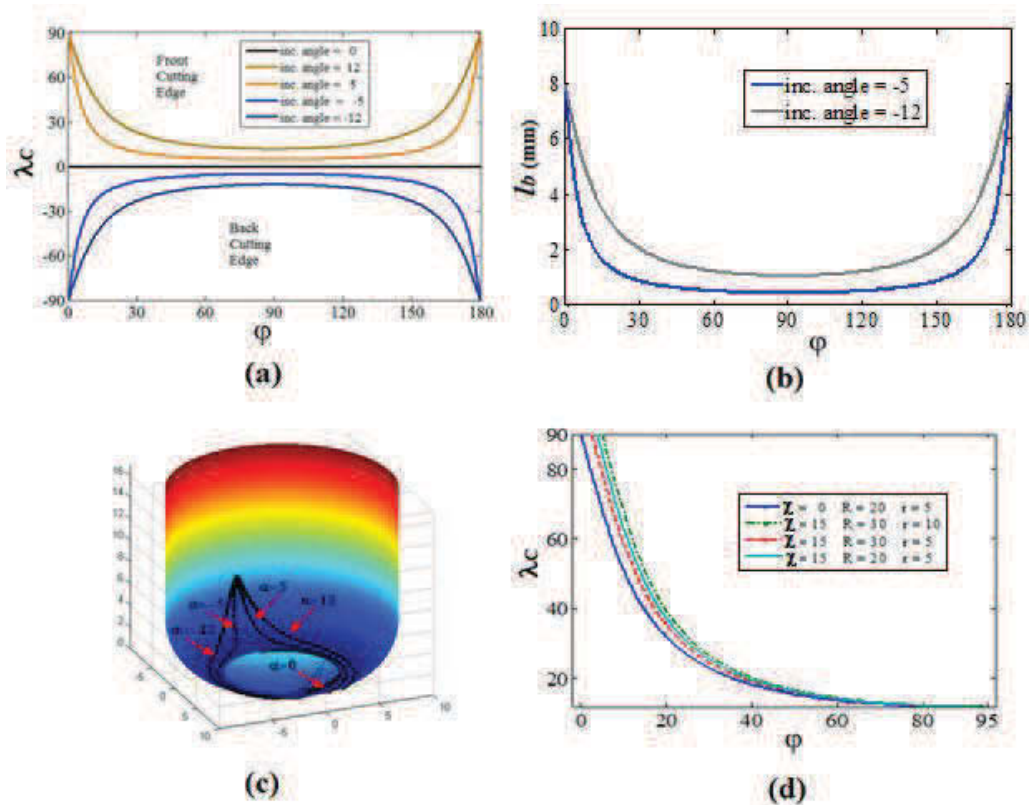


Fig. 4-5 Test on effect of some variables to LE-point, a) effect of inclination angle to λ_c , b) Effect of inclination angle to length of bottom CWE, c) LE-point on toroidal tool, d) Effect of helical angle to λ_c

Since λ_c is obtained, then the length of bottom CWE for every engagement angle were determined using Eq.(4-21), and the result is presented in Fig. 4-5b. In this test, r_t was assumed zero. The length of the bottom CWE is only exist when the tool has a negative inclination angle ($\alpha < 0$). When $\alpha \geq 0$, then $l_b = 0$. From Fig. 4-5b can be seen that the profile of the graph for the length of the bottom CWE is similar to the one for its toroidal angle. The illustration of the LE-point for every engagement angle on the toroidal cutter is depicted in Fig. 4-5c.

Furthermore, the test was performed to check the effect of several variables, such as helical angle, radius and minor radius of the cutting tool, to the

LE-point. Four combinations of variables were tested and the results are shown in Fig. 4-5d. From this figure can be concluded that a helical angle makes the CWE start at $\varphi > 0$ (lag angle). Increasing helical angle and minor radius will increase the lag angle. On the other hand, increasing the radius of cutting tool will decrease the lag angle.

4.3. 2.5d Rough Milling (Flat-End Cutter)

The 2.5D milling operation is a common machining operation. In five-axis machining operation, 2.5D milling is normally performed during rough machining. In rough machining, raw material is removed as quickly as possible while leaving stock material for a semi-finishing allowance. The machining during this stage is less concern on the workpiece dimensional accuracy or surface quality. A study showed that approximately 50% of total cutting time in mould and die manufacturing is spent in the rough cutting stage [96, 97]. Therefore, increasing efficiency during rough machining will enhance overall throughout of the manufacturing process. Flat-end mill is generally employed for this operation due to the higher material removal rate and longer tool life.

In general, rough milling starts with a block material as the initial workpiece. Predicting the CWE during plain cutting with a block workpiece is a simple work. The axial depth of cut in the tool rotation is constant, and the length of cut is equal to the radial depth of cut. However, when a machining performs layer by layer cutting strategy, then the in process workpiece surface become more complex with staircase surface as shown in Fig. 4-6.

4.3.1. Obtaining the UE-Point During Rough Milling

For the rough milling, the workpiece surface is represented by the coordinate of the points that are located on the border wall as depicted in Fig. 4-6a. In every tool path, the border wall that has potential engages with the cutting tool should be determined. The potential border walls are the wall that are located in between $(T + r)$ and $(T - r)$. Where $T(x_T, y_T, z_T)$ is the coordinate of CL-point and r is the radius of the cutting tool. In the case as shown in Fig. 4-6b, only one wall that

has potential engage with the cutting tool, such as $v_t(x_{v_t}, y_{v_t}, z_{v_t})$ and $v_s(x_{v_s}, y_{v_s}, z_{v_s})$. By obtaining the representative points, two workpiece blocks, block A and block B, can be identified. Block A is a block where point $c(x_c, y_c, z_c)$ is located. Meanwhile block B is a block beside block A that has potential to engage with the cutting tool.

In every instantaneous tool location, the UE-point is calculated based on the coordinate of the LE-point (C_f). When a cutting tool without a helical angle performs plain cutting, the axial depth of cut and the length of cut have the same dimension. The UE-point is always located on the surface of the workpiece block A. The length of cut can be calculated by,

$$l_n = (z_A - z_C) \text{ , if } x_C < x_A \text{ and } z_C < z_A$$

$$l_n = (z_B - z_C) \text{ , if } x_C > x_A \text{ and } z_C < z_A$$
(4-22)

Then the coordinate of the UE-point (n_f) in the WCS is determined by mapping the parametric equation of a cylindrical surface as shown in Eq.(3-18), and it yields,

$$n_f(x_{n_f}, y_{n_f}, z_{n_f}) = [M]S_C(\varphi; l) \rightarrow l = l_n$$
(4-23)

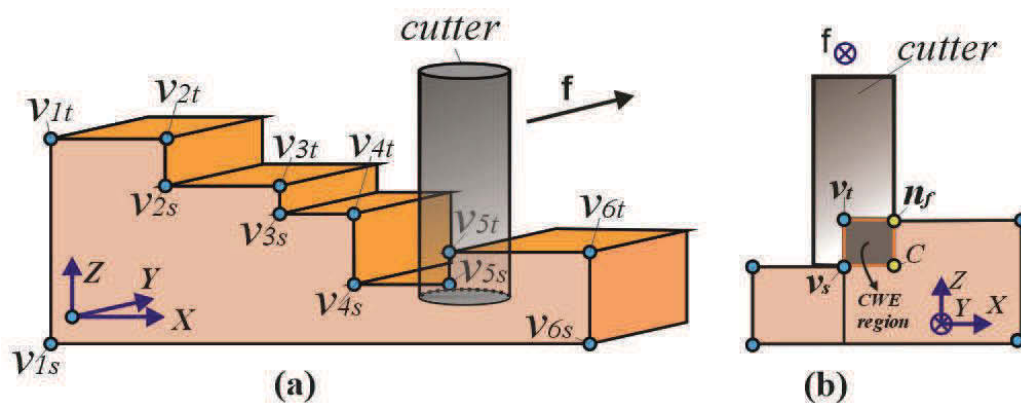


Fig. 4-6 a) Workpiece representation method for rough milling,
b) CWE region and CWE points

4.3.2. Effect of Helical Angle During Rough Milling

As discussed in the previous section, predicting CWE for a flat-end mill without helical angle during rough milling is a simple work. However, this method is not

applicable when a helical angle exists. The helical angle makes the calculation become more complex because the orientation of the cutting edge with respect to the engagement angle is continuously changed. Then, the equation to determine the UE-point yields to,

$$n_f(x_{n_f}, y_{n_f}, z_{n_f}) = [M]_h \cdot (0, 0, l_n) + C \quad (4-24)$$

where $[M]_h$ is a mapping operator when a helical angle exists. It is obtained using the method as explained in section 3.2.

The helical angle changes the orientation of the cutting edge and it makes the cutting edge can engage with more than one workpiece block. Moreover, the UE-point can be located either on the top surface or on the wall surface of the workpiece block. When the orientation of cutting edge is not along to the Z -axis in the WCS, then a method called the *Cylindrical-boundary* method is used to calculate the length of cut. The length of cut is required to calculate the UE-point as expressed in Eq.(4-24). It can be calculated if the distance between the LE-point to the surface where the UE-point located is known. This method consist of three methods depending on the axis used as the workpiece reference.

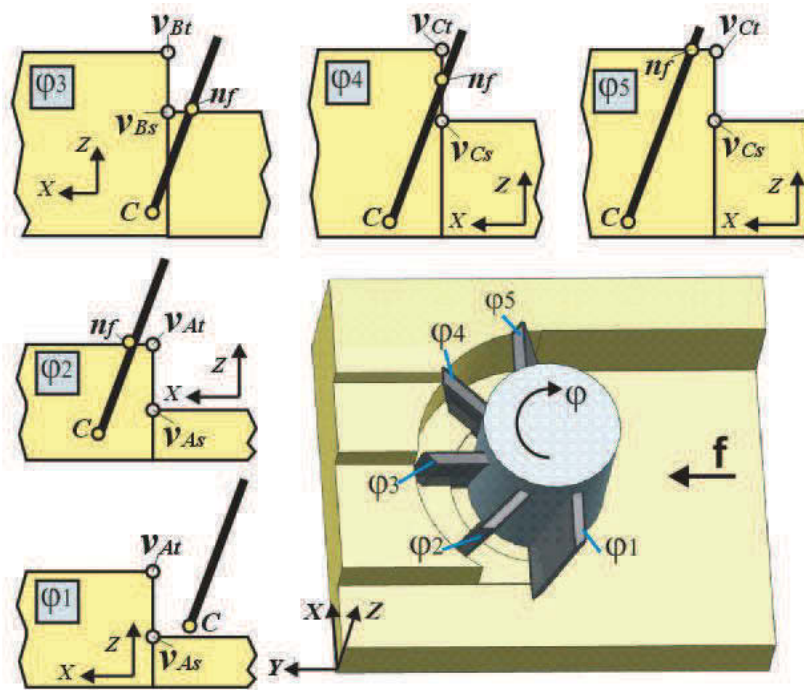


Fig. 4-7 Feasible Location of the UE-point during tool revolution

Z-Cylindrical method: this method is used when the distance between the reference point to the top surface in the z -axis is known. The equation to calculate the length of cut on the cylindrical side (l_n) is presented as follows,

$$l_n = (z_w - z_c) / \cos \vartheta \quad (4-25)$$

Where z_w and z_c are the z -axis of the workpiece surface and the z -axis of the LE-point, respectively. Meanwhile ϑ denotes the tool inclination angle relative to the z -axis in the WCS. The method to define ϑ has been discussed in the previous chapter.

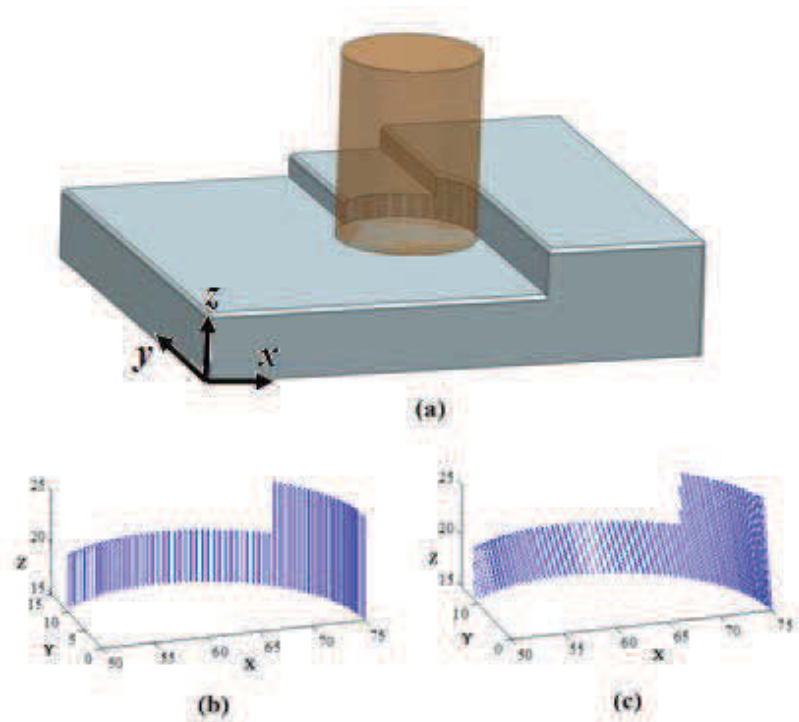


Fig. 4-8 Test model, a) part model, b) cut geometry without helical angle, c) cut geometry with helical angle

X-Cylindrical method: this method is used when the distance between reference points to the wall surface of the workpiece in the x -axis is known. By referring to Fig. 3-2, the equation to calculate l_n for the X -cylindrical method was derived as follows,

$$l_n = (x_w - x_c) / \tan \theta_Y \cos \vartheta = (x_w - x_c) / \sin \theta_{B_X} \quad (4-26)$$

Y-Cylindrical method: this method is used when the distance between a reference points to the wall surface in the y -axis is known. And the method to calculate l_n is expressed by,

$$l_n = \frac{(y_w - y_c)}{\tan \theta_x \cos \vartheta} = \frac{(y_w - y_c)}{(\sin \theta_{A_x} \cos \theta_{B_x})} \quad (4-27)$$

In the case as shown in Fig. 4-7, there are three border walls that have potential to engage with a cutting tool. Because the tool has a helical angle, the *Cylindrical boundary* method with the tool orientation angle relative to the z -axis is equal to the helical angle ($\vartheta = \chi$). Therefore, several checks should be performed to obtain the final UE-point. The entire steps to determine the UE-point is elaborated as follows,

1. **When $z_c > z_{v_s}$ and $x_c < x_{v_s}$ (at φ_1):** it means that there is no CWE.
2. **When $x_c < x_{v_s}$ and $z_c < z_{v_s}$:** the cutting edge engages with the surface of block B, and the length of cut is calculated using Eq.(4-25) with $z_w = z_{v_s}$.
3. **When $x_c > x_{v_s}$ and $z_c < z_{v_t}$:** there are three possible locations of the UE-point: on the top surface of block A (at φ_2 and φ_5), on the top surface of block B (at φ_4), or on the wall surface of block A (at φ_3). In beginning, it is assumed that the UE-point is located on the top surface of block A. Then l_n is calculated using Eq.(4-25) with $z_w = z_{v_t}$. Once l_n is obtained, the coordinate of the UE-point can be calculated. This point is then checked to find and correct the error. If $x_n < x_w$, it means that the actual UE-point is not located on the top surface of block A. It can be on the wall surface or on the top surface of block B. Therefore, using the second assumption that the engagement point is located on the wall surface, l_n is defined using Eq.(4-26). Once again, the UE-point is calculated using Eq.(4-24). The final examination is performed to check the possibility of the actual UE-point is located on the surface of block A. The second assumption is incorrect if $z_n < z_{v_s}$. It means that n_f is located on the top surface of block A.

When a large cutting tool is used to machine a high staircase workpiece (the distance between the border wall is small), then there is a possibility that the UE-point is not located neither on the block A nor on the block B. It can be located on the block next to the block B. Then, using the same method, the calculation is continued until the final engagement is obtained.

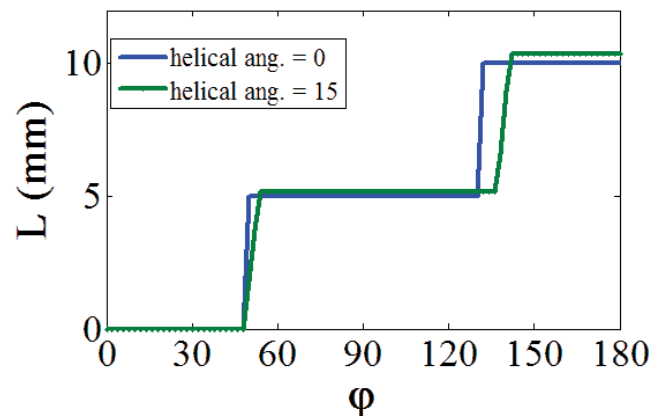


Fig. 4-9 The length of cut (L) with and without helical angle

4.3.3. Application and Discussion

The formulae derived in this section have been used to develop a simulation program using MATLAB. One part design as shown in Fig. 4-8a was cut using a flat-end cutting tool with 30 mm diameter. The tests were performed for a cutting tool with $\chi = 0$ and that with $\chi = 15$. The shape of cut as a function of engagement angle when $\chi = 0$ is depicted in Fig. 4-8b. While Fig. 4-8c presents the shape of cut when $\chi = 15$. It can be seen that the shape of cut when the tool without a helical angle is perpendicular, while the tool with a helical angle produced a tilted cut.

The lengths of cut for both tests are shown in Fig. 4-9. From this graph can be seen that a helical angle gave an effect to the length of cut. When the UE-point is located on the top surface, the length of cut obtained from the tool with a helical angle is larger than that without a helical angle. On the other hand, when it is on the wall surface, the length of cut increases gradually, and hence it can be either higher or smaller.

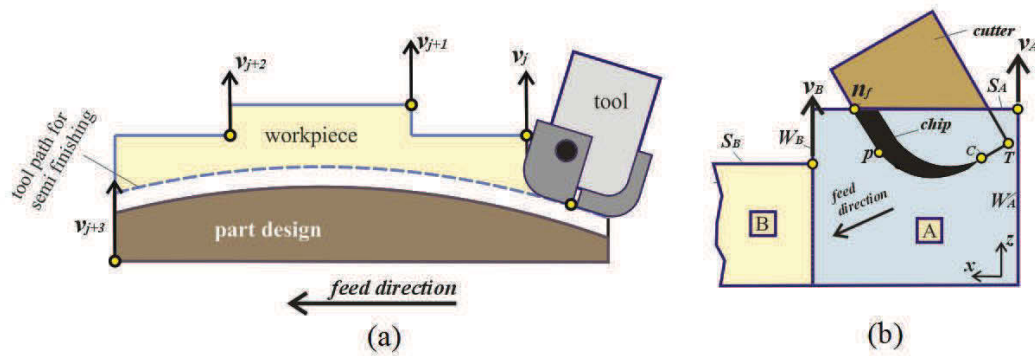


Fig. 4-10 Workpiece representation method

4.4. Semi-Finish Milling with Straight Staircase Profile

Semi-finish milling is a machining process to remove the steps and shoulder remaining from the roughing stage and a finishing allowance of uniform thickness is left. This operation is important in maintaining a relatively constant metal removal rate for subsequent finishing [98]. The characteristic of semi-finish in a sculptured surface machining is an extreme variation of cutting force. It is occurred due to the dynamic Cutter Workpiece Engagement (CWE) is produced by both the sculptured part surface and the staircase workpiece surface. Even though semi-finishing is less concern on surface quality, but extreme cutting force variation will give adverse affect to the cutting tool. Therefore, controlling the generated cutting force along the tool path become more important.

In this study, the staircase workpiece as depicted in Fig. 4-10a, which is normally produced by rough milling, was used in the model development. A number of normal vectors, which are located on the border of the workpiece surface, are used as references for further calculations. At every instantaneous tool position, two vectors, $v_A(x_A, y_A, z_A)$ and $v_B(x_B, y_B, z_B)$, are identified. The vector v_A is located before $C(x_C, y_C, z_C)$. While v_B is located either following or prior to v_A , depending on the tool orientation. Both vectors are used to define two workpiece blocks that have potentially engage with the cutting tool. After two vectors (v_A and v_B) are identified, then the workpiece is divided into two subsequent blocks, the block A and the block B as presented in Fig. 4-10b. Because of the tool orientation and the shape of workpiece surface, the UE-point

can be located either on the top surface of block A (S_A), the wall surface of block A (W_A), the top surface of block B (S_B) or the wall surface of block B (W_B). A flowchart describing the steps used to obtain the CWE points for both flat-end and toroidal cutter are presented in Fig. 4-12 and the details will be given in the subsequent sections.

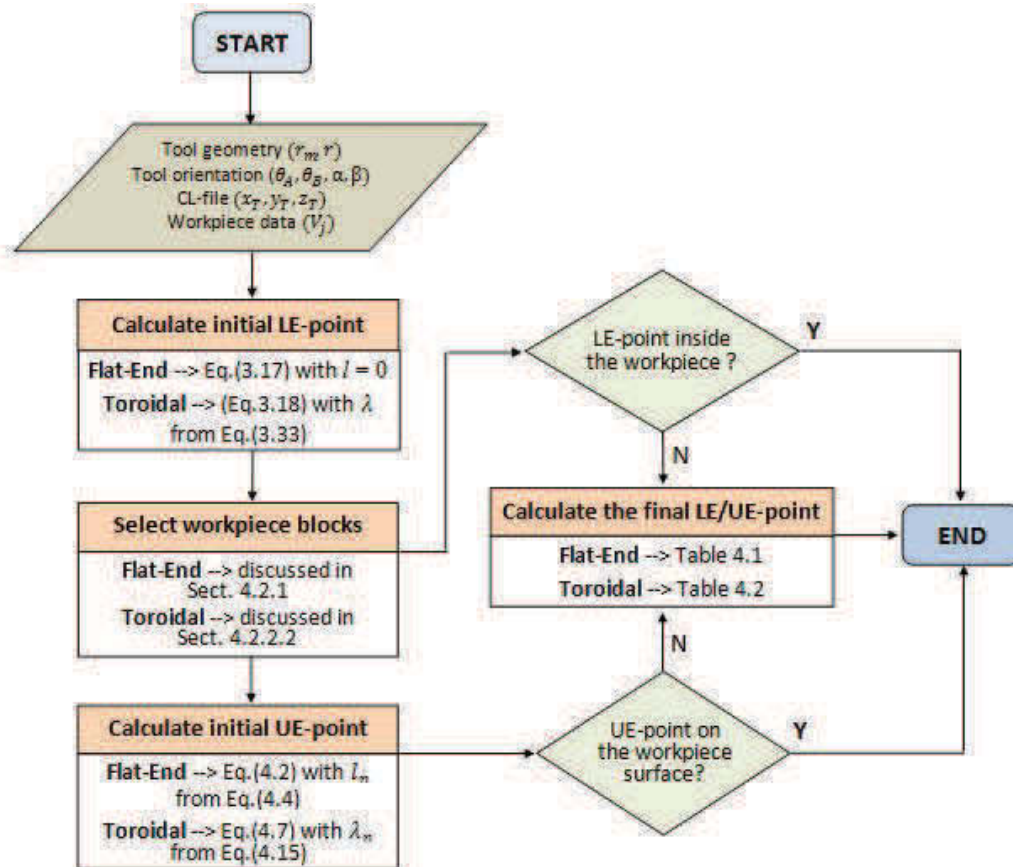


Fig. 4-11 Flowchart for obtaining CWE points for flat-end cutter

4.4.1. Obtaining the UE-Point of Flat-End Cutter During Semi Finishing

During a semi-finish milling with flat-end tool, the block B is defined only based on the orientation of cutting edge. When θ_B is positive, v_B is located after v_A as depicted in Fig. 4-12a. Otherwise, v_B is located before v_A as shown in Fig. 4-12b.

Initially the UE-point is calculated by assuming that it is located on S_A . The UE-point at that stage is called the initial UE-point, $n_i(x_{n_i}, y_{n_i}, z_{n_i})$. It is called 'initial' because it needs to be checked further to determine if the initial

assumption is correct or not. If it is correct, then n_i is the final UE-point (n_f). Otherwise, the recalculation is performed to obtain the final UE-point, $n_f(x_{nf}, y_{nf}, z_{nf})$, must be performed.

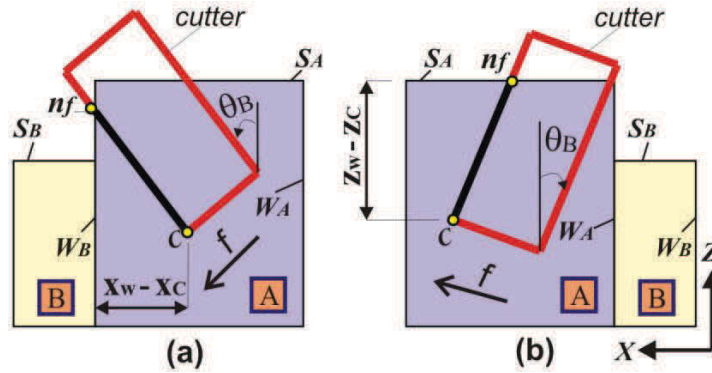


Fig. 4-12 Two possible locations of the UE-point for flat-end cutter, a) wall of workpiece, b) top of workpiece

The coordinate of the UE-point is calculated using Eq.(4-23) after the length of cut (l_n) is determined. For a flat-end cutter $l = l_n$, a method called the *Cylindrical-boundary* method is used to define the length of cut as elaborated in section 4.3. However, Eq.(4-25) - Eq.(4-27) are calculated using the tool orientation angle when the tool with a helical angle. Therefore, when the tool without inclination angle, then ϑ, θ_A and θ_B are used as tool orientation instead of $\vartheta_\chi, \theta_{A\chi}$ and $\theta_{B\chi}$.

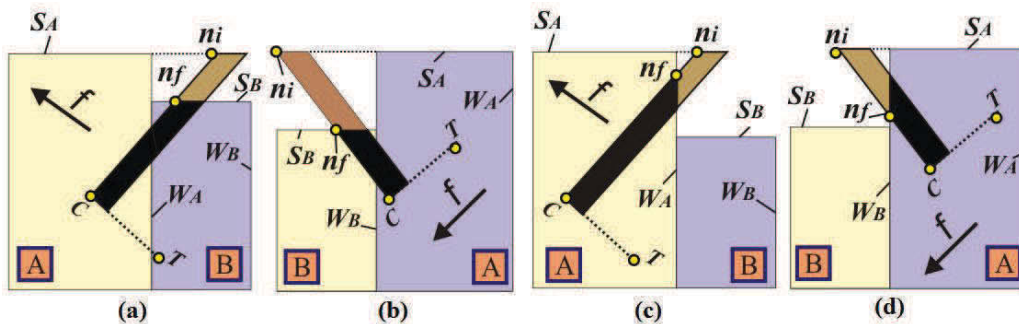


Fig. 4-13 Location of the UE-point when $z_A > z_B$

Once n_i is obtained, then it is checked to determine whether or not it is on S_A or not. The initial assumption is deemed incorrect if $x_{n_i} < x_A$ when the tool has a negative θ_B , or if $x_{n_i} > x_B$ when the tool with positive θ_B . In this case, the final UE-point needs to be recalculated. The final UE-point can be identified after point

$n_w(x_{n_w}, y_{n_w}, z_{n_w})$ is obtained. The engagement point n_w is on the wall of block A when θ_B is negative, or on the wall of block B when θ_B is positive. Following this, n_w can be determined after the length of cut on the wall surface (l_w) is calculated using the *Z-Cylindrical* method. The coordinate n_w is then defined using Eq.(4-23) with $l = l_w$. Finally, several conclusions regarding the cutter workpiece engagement can be made.

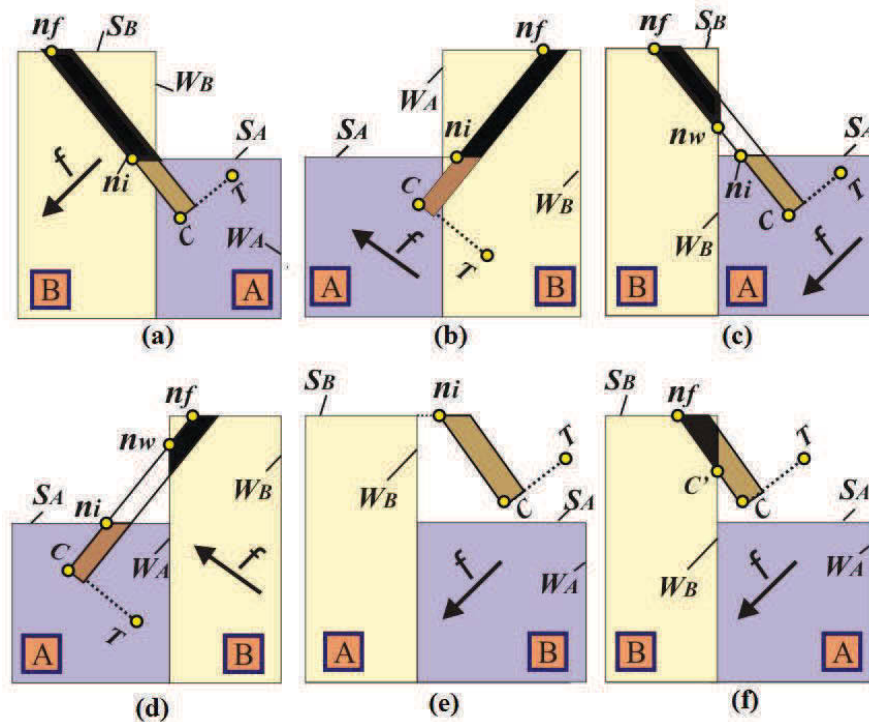


Fig. 4-14 Location of the UE-point when $z_A < z_B$

All of the CWE conditions for the flat-end cutter are illustrated in Fig. 4-13 and Fig. 4-14. The methods to identify the location of the UE-point and to define the lengths of cut are presented in Table 4-1. The length of cut l_A and l_B are the length of cut when the UE-point is on S_A and S_B , respectively. Both of them are calculated using the *Z-cylindrical* method. For cases B.3 and B.4, the tool engages with both workpiece blocks, but some part of the tool (in between the engagement points) are out of the workpiece as depicted in Fig. 4-14c and Fig. 4-14d. Another circumstance, which is shown in B.6, is a case when the tool is located above S_A but some part of it engage with block B. In this case, the LE-point moves from C_f to C_f' .

Table 4-1 Method to identify and calculate CWE for flat-end cutter

No.	Indication	Location of the UE-point	l_n
$z_A > z_B$			
A.1	$x_{n_i} < x_A, z_{n_i} > z_B, z_{n_w} < z_B$	W_A (Fig. 4-13a)	$l_n = l_B$
A.2	$x_{n_i} > x_B, z_{n_i} > z_B, z_{n_w} < z_B$	W_B (Fig. 4-13b)	$l_n = l_B$
A.3	$x_{n_i} < x_A, z_{n_i} > z_B, z_{n_w} > z_B$	S_B (Fig. 4-13c)	$l_n = l_W$
A.4	$x_{n_i} > x_B, z_{n_i} > z_B, z_{n_w} > z_B$	S_B (Fig. 4-13d)	$l_n = l_W$
$z_A < z_B$			
B.1	$x_{n_i} > x_B, z_{n_w} < z_A < z_B$ and $z_C < z_A$	S_B (Fig. 4-14a)	$l_n = l_B$
B.2	$x_{n_i} < x_A, z_{n_w} < z_A < z_B$ and $z_C < z_A$	S_B (Fig. 4-14b)	$l_n = l_B$
B.3	$x_{n_i} < x_B, z_A < z_{n_w} < z_B$ and $z_C < z_A$	W_B and S_B (Fig. 4-14c)	$l_n = l_B - (l_W - l_A)$
B.4	$x_{n_i} > x_B, z_{n_w} < z_A < z_B$ and $z_C < z_A$	W_A and S_B (Fig. 4-14d)	$l_n = l_B - (l_W - l_A)$
B.5	$z_C > z_A$ and $z_w > z_B$	None (Fig. 4-14e)	$l_n = 0$
B.6	$z_C > z_A$ and $z_w < z_B$	S_B (Fig. 4-14f)	$l_n = (l_B - l_A)$

Although the procedures, which were explained above, are assumed only two workpiece blocks have potential to engage, however, when large cutting tool is selected to cut high staircase workpiece, then the procedure can be continued to check the engagement point with the block next to block B. Obviously, the calculation time increase as the staircase increase, and vice versa.

4.4.1.1. Application and discussion

A part design with complex surface as depicted in Fig. 4-15a was tested. The tool path was generated using Siemens-NX. Because of the complexity of the surface profile, the tool was rotated in both the x -axis (θ_A) and the y -axis (θ_B) during the machining process. In this test, the tool was set with inclination angle 10° .

Machining conditions used in the test were feedrate 0.3 mm/tooth, and cutting speed 5000 rpm. A two teeth flat-end cutter with diameter 20 mm was employed as cutting tool.

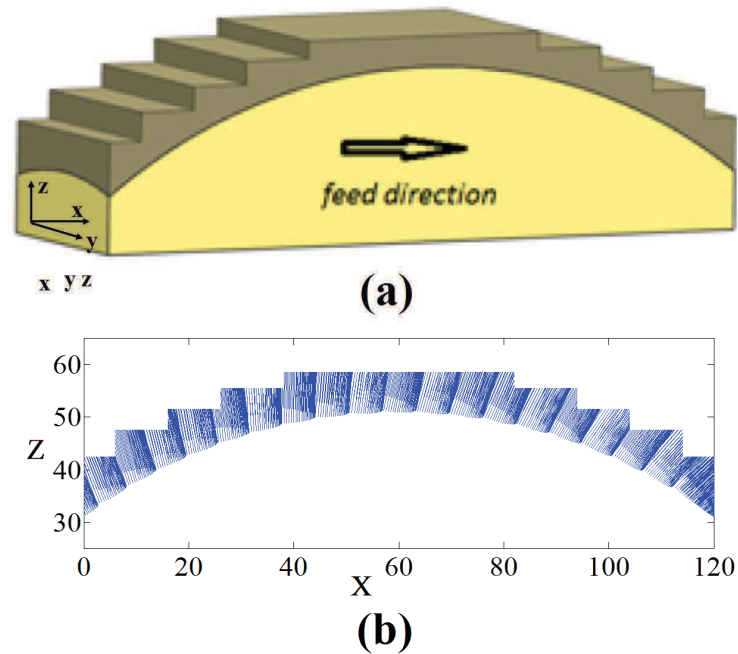


Fig. 4-15 Test model, a) Part model, b) chip geometry generated by the program simulation

Using the simulation program, which is called Analytical Boundary Simulation (ABS), the shape and size of cross cut geometry can be generated. The shapes of cut that were generated using the program simulation are shown in Fig. 4-15b. The shapes of cut shown in this figure are the CWE for every CC-point at $\varphi \in \{0, 180\}$. It can be seen that the shape of cut on the top side resemble the shape of the workpiece surface, and the one at the bottom side resembles the shape of the part surface. This is an indication that the proposed method is accurate.

The lengths of cut progression for one tool pass are depicted in Fig. 4-16a. Using the same part and workpiece surface, the length of cut for cutting tool without a helical angle and the one with a helical angle were generated and presented in Fig. 4-16b. The helical angle used in this calculation was 11° , meanwhile other variables were kept similar. The complexity of the part and workpiece surface made the length of cut changes dynamically. The existence of

the helical angle changed the profile of the graph of the length of cut significantly especially at the bottom side as can be seen in Fig. 4-16. It was due to the helical angle made the engagement occurred gradually.

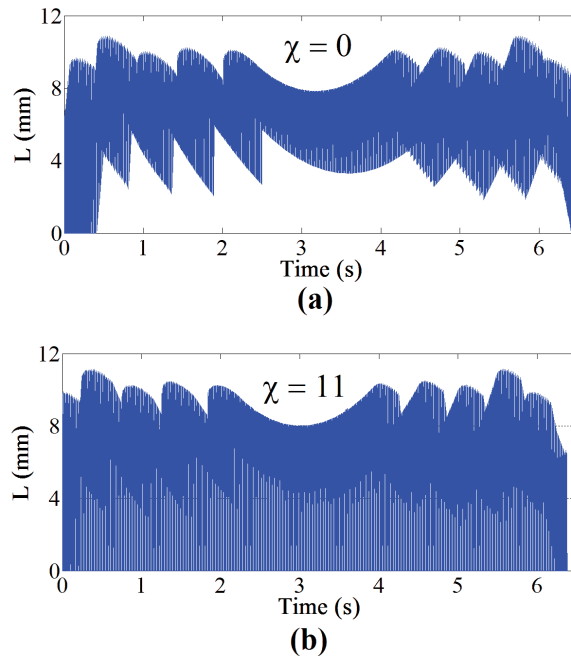


Fig. 4-16 The length of cut progression (L), a) without helical angle ($\chi=0$),
b) with helical angle ($\chi=11$)

Even though the shape of cut was similar to the part and workpiece design, the accuracy of the proposed model need to be verified. Fig. 4-17 depicts two verification methods that were performed to check the accuracy of the proposed model. First, the accuracy was tested by comparing the coordinate of the UE-points with respect to the workpiece surface as presented in Fig. 4-17a. The graph shows that all of the UE-points, for all CC-point at $\varphi = 0$, are precisely close to the workpiece surface line. This proved that the proposed model is accurate.

To ensure that the generated UE-points belong to both the cutter and workpiece surface, another verification was performed using commercial CAD software Siemens-NX. As shown in Fig. 4-17b, the coordinates of the UE-point were checked from the extraction model that was obtained from the intersection between the cutter model and the workpiece model. The extraction model was obtained by placing the cutter model at the instantaneous CC-point and adjusting its orientation. After that, the intersection between the workpiece model and the

tool model can be extracted. The cutter model was manipulated by making groove at the front side so that the engagement angle of the cutter-workpiece intersection can be easily identified. Once the extraction model is obtained, then the coordinate of the UE-point can be checked and compared with those generated by the ABS. All of the UE-points from Fig. 4-17a were verified and the results confirm the accuracy of the proposed model.

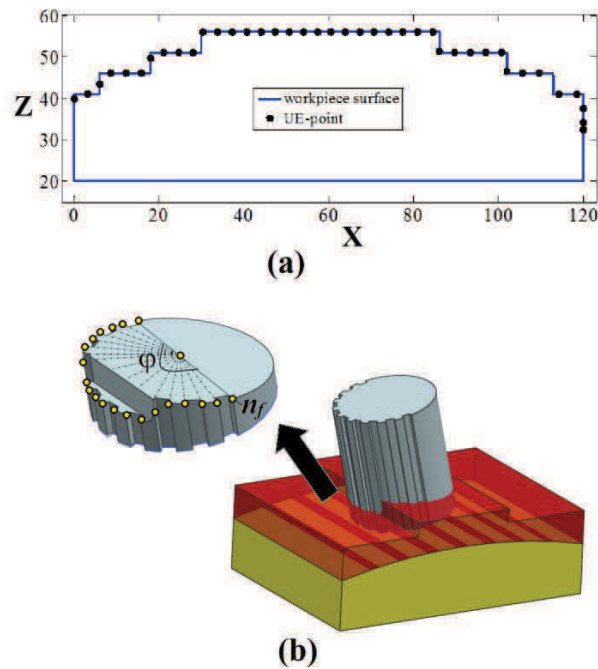


Fig. 4-17 Two types of model verification, a) comparing the UE-point with respect to workpiece surface, b) verification using Siemens-NX

The shapes and length of cuts as a function of the engagement angle for selected CC-points when the tool has not helical angle are depicted in Fig. 4-18. For CC-3, the tool started engage with the workpiece at $\varphi = 8$. It was due to the CC-point was located out of the workpiece and θ_B was negative. CC-34 shows a complete engagement and the lengths of cut fluctuate drastically because the cutting tool contacted with two workpiece blocks. Meanwhile for CC-46, only some parts of cutting tool that engaged with the workpiece. The front side was located out of the workpiece limit (the length of workpiece is 120 mm).

Fig. 4-19 shows the comparison of the shape and length of cut for CC-12, which were obtained from the cutting tool with a helical angle ($\chi = 11$) and those

were obtained without helical angle. Fig. 4-19c shows the length of cut at $\varphi \in \{0, 190\}$. This figure shows clearly that a helical angle gives a significant effect to the initial and final cutter workpiece engagement, and also when the UE-point is located on the wall surface of the workpiece. Typical of the tool with a helical angle is the tool enters to and exit from the workpiece gradually. It is different compared to the tool without a helical angle that the tool enters to the workpiece ($\varphi = 0$) with maximum engagement, and exit totally at $\varphi = 180$. As can be seen in Fig. 4-19c, when the tool with helical angle, the engagement is still occurred at $\varphi > 180$. In this case, C_f moves to C_f' . For CC-12, the tool exits totally at $\varphi > 188.8$. Due to the tool engages gradually, it makes the profile of the length of cut at the bottom side as displayed in Fig. 4-16b is different.

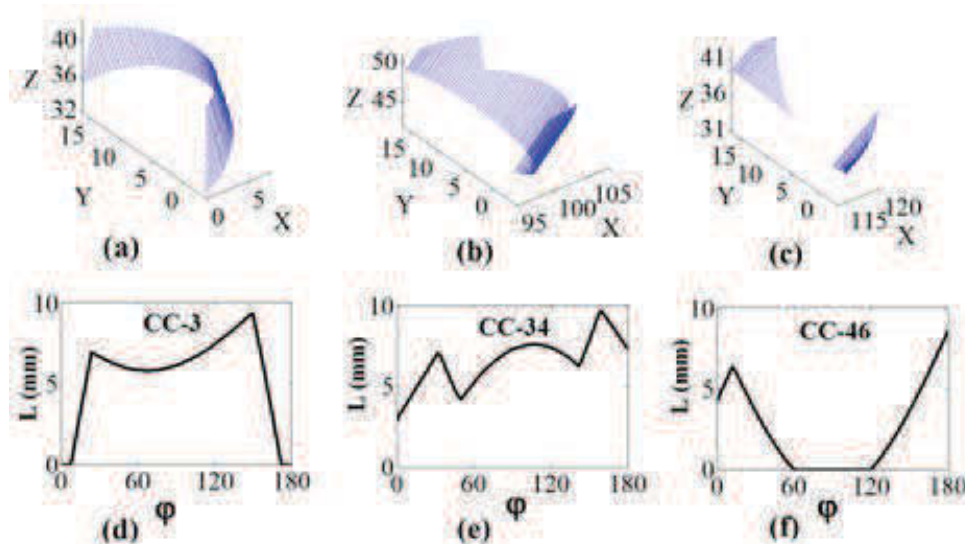


Fig. 4-18 Chip geometry of selected CC-points, a,b,c) the shape of cut at $\varphi \in \{0, 180\}$, d,e,f) the length of cut (L) at $\varphi \in \{0, 180\}$

Another test using a concave part surface and a workpiece with higher staircase profile, as depicted in Fig. 4-20a, was also performed. It was aimed to check the applicability of the proposed method with others circumstances. The same cutting tool was used to perform this test. To avoid gouging, the tool was inclined with the inclination angle 12° . The shape of cut geometry and length of cut for one tool pass are presented in Fig. 4-20b and Fig. 4-20c. The cut geometry, once again, is similar to the shape of part surface and workpiece surface.

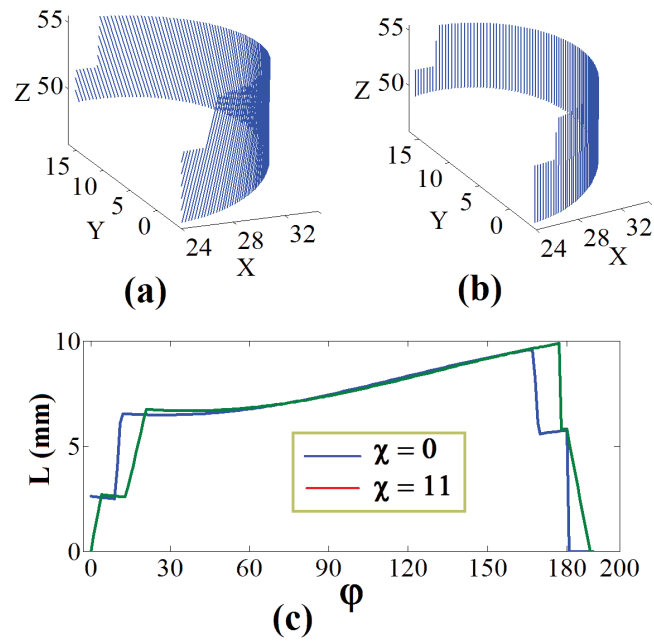


Fig. 4-19 Cut geometry of CC-12 at $\varphi \in \{0, 190\}$, a) with helical angle ($\chi = 11$), b) without helical angle, c) the length of cut (L)

The shape of cut as a function of the engagement angle for several CC-points are depicted in Fig. 4-20d. For CC-5, the tool engaged with two workpiece blocks. In this case, the tool orientation was negative θ_A and the surface of block B was lower than the surface of block A. Another condition is presented by CC-23. Because the workpiece surface was high staircase, the cutting tool engaged with three workpiece blocks. For CC-30, the orientation of the cutting tool, θ_A , was negative and the surface of block B was higher than the surface of block A. In this case, the cuts, which are highlighted in CC-30, show the condition when the cutting tool engages with both of workpiece blocks but some parts of cutting tool in between the LE-point and the UE-point are out the workpiece. This is the case as explained by Fig. 4-14c.

4.4.2. Obtaining the UE-Point for Toroidal Cutter During Semi-Finish Milling

Because the equations for the cylindrical and toroidal surface are different, the method used to calculate CWE on the toroidal side is different from that on the cylindrical side. Therefore, the location of n_f whether it is on toroidal side or the

cylindrical side is determined before the calculation is made. This is performed by checking the coordinate of the UE-point relative to point C and point P (see Fig. 4-21). Where point $P(x_p, y_p, z_p)$ denoting the end point of toroidal cutter on the WCS, which is calculated using Eq. (3-18) with $\lambda = 90$. In order to check the UE-point position easier, point P and the UE-point are transformed into TCS. If the UE-point is located above point P , it means that the UE-point is located on the cylindrical side, as depicted in Fig. 4-21a. Cylindrical boundary method, which is used to define the length of cut for a flat-end cutter, can also be utilized to calculate the length of cut for the cylindrical side of a toroidal cutter. However, the length of cut on the cylindrical side is measured from point P to n_f instead of from point C to n_f .

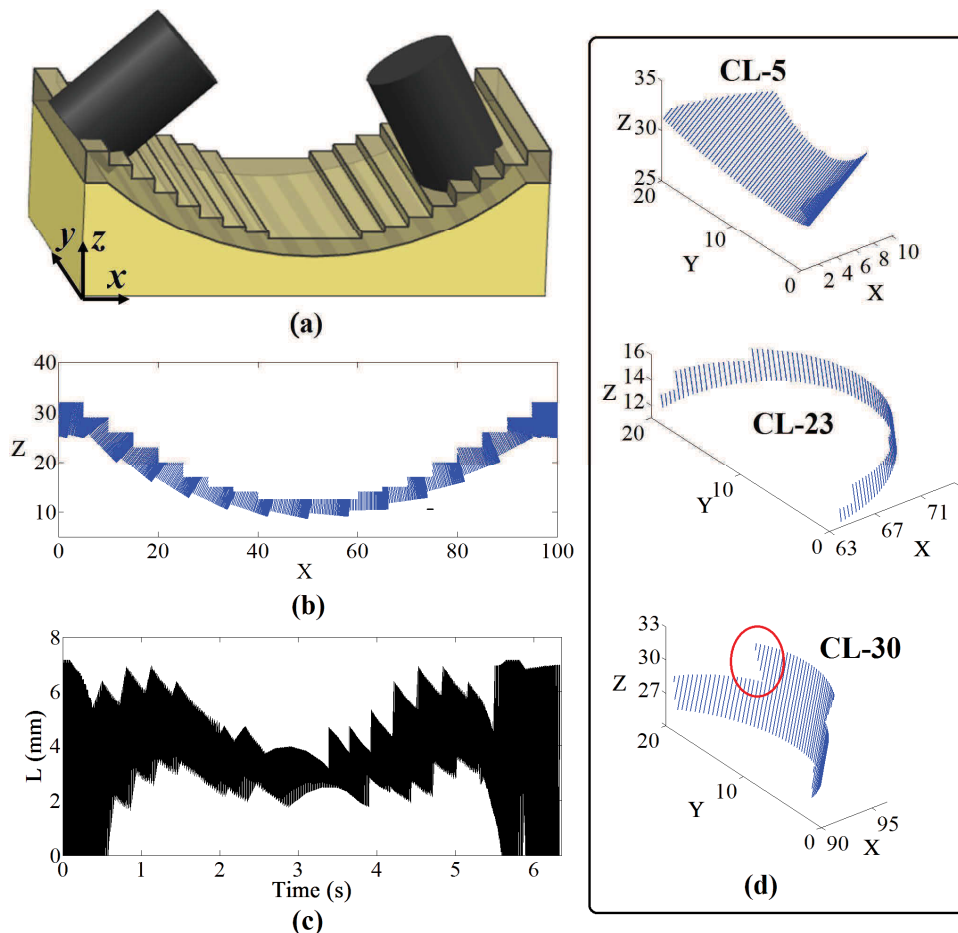


Fig. 4-20 Test model 2, a) part model,

b) cut geometry generated by the program, c) the length of cut progression (L),

d) cut geometry for several CC-points at $\varphi \in \{0, 180\}$

On the other hand, when the UE-point is located below point P , it means that the UE-point is located on the toroidal side, as shown in Fig. 4-21b. In this case, the UE-point is calculated using the mapping operation of toroidal side as shown in Eq. (3-18), and it yields to

$$n_f(x_{n_f}, y_{n_f}, z_{n_f}) = [M] S_T(\varphi; \lambda_n) \quad (4-28)$$

When the tool has helical angle, however, the UE-point is determined using the following equation,

$$n_f(x_{n_f}, y_{n_f}, z_{n_f}) = [M]_h \begin{bmatrix} r \cdot \sin \lambda \\ r \cos \lambda \\ r - r \cos \lambda \end{bmatrix} + C \quad (4-29)$$

The UE-point, as presented in Eq.(4-29) and Eq. (4-30), can be calculated after the toroidal angle (λ) is determined. The method to define the toroidal angle of the UE-point will be discussed in the following section.

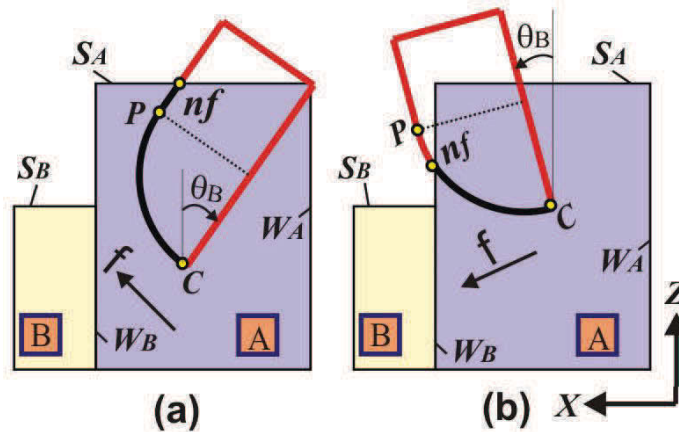


Fig. 4-21 Two possible locations of the UE-point for toroidal cutter,
a) wall of workpiece, b) top of workpiece

4.4.2.1. Toroidal Boundary Method

Toroidal angle of the UE-point (λ_n) is calculated using a method called the *Toroidal-Boundary Method*, which consists of the *Z-toroidal* and the *X-toroidal method*. The toroidal angle can be determined if at least one of the axis components of the UE-point, $n_f(x_{n_f}, y_{n_f}, z_{n_f})$, is known. For example, when the UE-point is located on the top of workpiece block as shown in Fig. 4-21a, then

z_{nf} is equal to z_A . In this case, λ_n is calculated using the *Z-toroidal*. Meanwhile, the *X-toroidal* method is used when the UE-point is located on the wall of the workpiece block.

Z-toroidal method. If z'_{S_T} in Eq.(3-18) is identified, then the toroidal angle is calculated by extracting Eq.(3-18) in order to obtain z'_{S_T} . Because the purpose of this method is to define the coordinate for n_f , the symbol z'_{S_T} is replaced by z_{nf} , and the toroidal angle is expressed using the following equations:

$$z_{nf} = [-\cos \theta_A \sin \theta_B \quad \sin \theta_A \quad \cos \theta_A \cos \theta_B \quad z_T] S_T(\varphi; \lambda) \quad (4-30)$$

By substituting $S_T(\varphi; \lambda)$ from Eq.(3-16), Eq.(4-30) is altered as follows,

$$\begin{aligned} & [-r \cos \theta_A \cos \theta_B] \cos \lambda \\ & + [r \cos \varphi \sin \theta_A - r \sin \varphi \sin \theta_A \sin \theta_B] \sin \lambda \\ & = (z'_{G_T} - z_T) - [r \cos \theta_A \cos \theta_B \\ & + r_m \cos \varphi \sin \theta_A - r_m \sin \varphi \cos \theta_A \sin \theta_B] \end{aligned} \quad (4-31)$$

Eq.(4-31) is simplified to give,

$$a \cos \lambda + b \sin \lambda = c \quad (4-32)$$

Where:

$$\begin{aligned} a & = -r \cos \theta_A \cos \theta_B; \\ b & = r \cos \varphi \sin \theta_A - r \sin \varphi \cos \theta_A \sin \theta_B \\ c & = (z'_{G_T} - z_T) - [r \cos \theta_A \cos \theta_B + r_m \cos \varphi \sin \theta_A \\ & \quad - r_m \sin \varphi \cos \theta_A \sin \theta_B] \end{aligned} \quad (4-33)$$

To solve the above problem, the sum of the two trigonometric functions in Eq. (4-32) is expressed as a single trigonometric function as follows,

$$k \cos(\lambda - \tau) = (k \cos \tau) \cos \lambda + (k \sin \tau) \sin \lambda \quad (4-34)$$

By referring to Eq. (4-32) and Eq. (4-34), k and τ can be expressed by,

$$k = \sqrt{a^2 + b^2}; \quad \tau = \tan^{-1}(b/a) \quad (4-35)$$

Finally, the toroidal angle of the point on the toroidal surface is determined by,

$$\lambda = \tau + \cos^{-1}(c/k) \quad (4-36)$$

X-toroidal method. Following the same procedure for the *Z-toroidal method*, the toroidal angle can be determined if x_{nf} is known. Then the following equations be derived,

$$x_{n_f} = [\cos \theta_B \quad 0 \quad \sin \theta_B \quad x_T] S_T(\varphi; \lambda) \quad (4-37)$$

$$\begin{aligned} & (-r \sin \theta_B) \cos \lambda + (r \sin \varphi \cos \theta_B) \sin \lambda \\ & = (x_T - x_{n_f}) + (r_m \sin \varphi \cos \theta_B - r \sin \theta_B) \end{aligned} \quad (4-38)$$

Where:

$$\begin{aligned} a &= -r \sin \theta_B; \\ b &= r \sin \varphi \cos \theta_B; \\ c &= (x_T - x_{n_f}) + (r_m \sin \varphi \cos \theta_B - r \sin \theta_B) \end{aligned} \quad (4-39)$$

Hereinafter, the toroidal angle will be defined using single trigonometric function as expressed in Eq.(4-34)–Eq.(4-36).

4.4.2.2. Identification and Calculation of the Final UE-Point

Similar to a flat-end cutter, initially the UE-point is calculated by assuming that it is located on the surface of block A. Block B for a tool with positive θ_B is located next after block A. However, because of its toroidal side, it is possible that the tool engages with the block next after block A even though the tool has a negative θ_B . This is checked by calculating λ_W using the *X-toroidal* method with x_{n_f} equal to the coordinate of the vector next to v_A . If $0 < \lambda_W < 90$, then the block next after A is selected to be block B. Otherwise, block B is located before block A.

Various possible conditions of the CWE are depicted in Fig. 4-22 and Fig. 4-23. The methods used to identify the location of the UE-point as well as those used to calculate their coordinates are presented in Table 4-2. Mostly the appropriate method can be determined only by comparing the indication variables (v_A, v_B, n_i, P). However, in some cases, such as with A.3, B.1, C.1 and C.3, two possible methods can be used to obtain the toroidal angle of the UE point. In these cases, both methods are calculated in order to determine the correct one. For case A.3, the method which produces as smaller λ_{n_f} is chosen to calculate n_f . Meanwhile, for B.1 and C.1, the method that generates as larger λ_{n_f} is selected because to $z_A > z_B$. For case C.1, the method that gives a smaller l_n is chosen to calculate the final UE point.

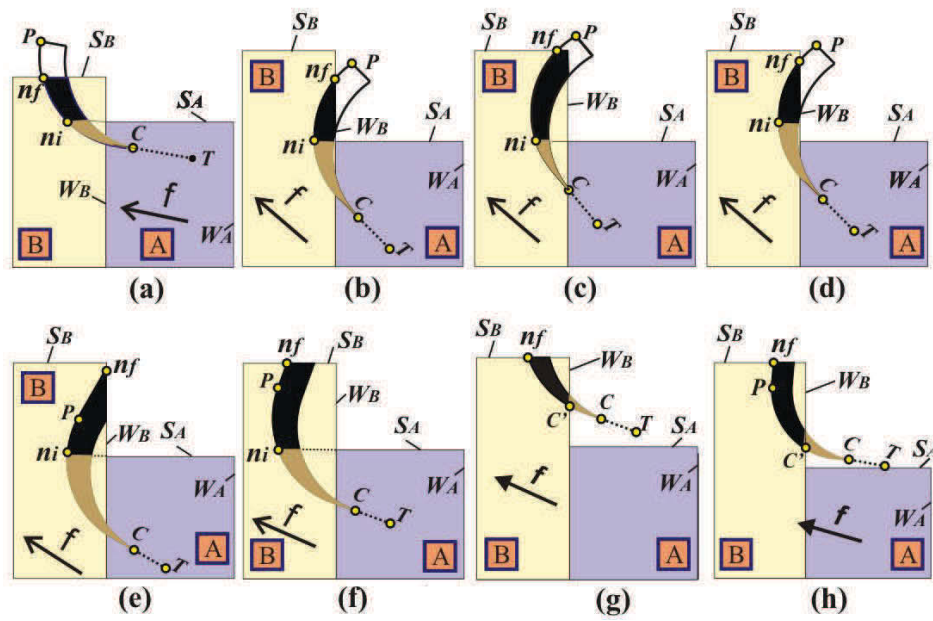


Fig. 4-22 Various possible conditions of CWE with toroidal cutter when $z_A < z_B$

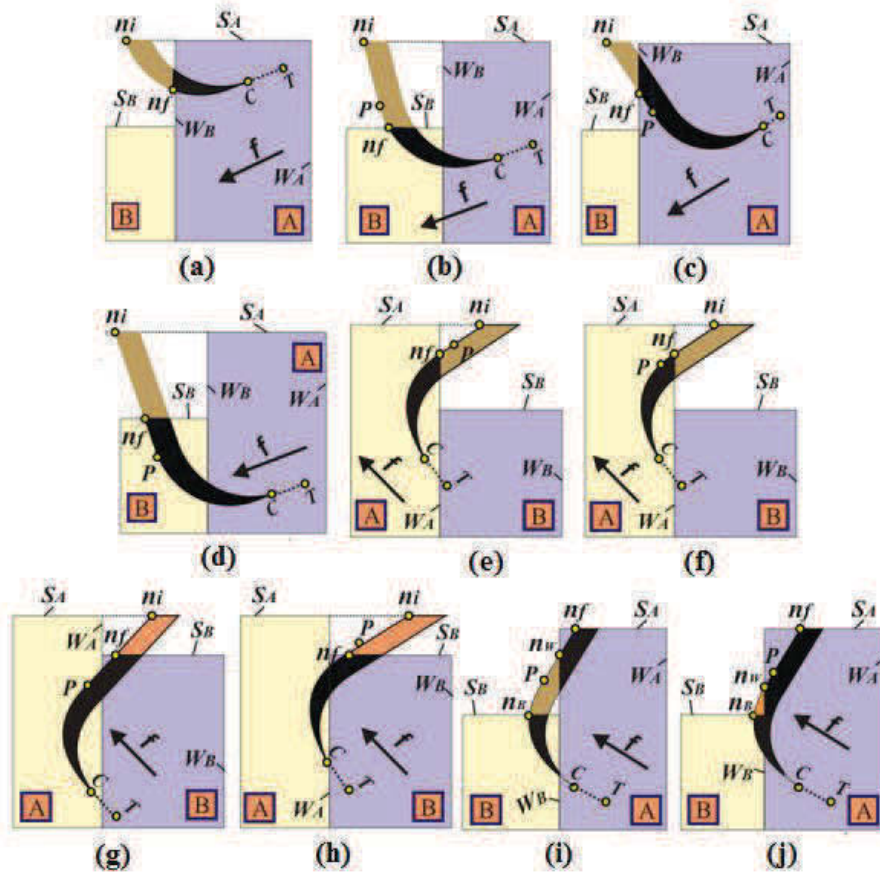


Fig. 4-23 Various possible conditions of CWE with toroidal cutter when

$$z_A > z_B$$

Table 4-2: Method to identify and calculate CWE for toroidal cutter

No.	Indication	Actual CWE location (Tool and Workpiece)	Method	z_{nf}/x_{nf} / z_W/x_W
A.	($x_{n_i} > x_B$ and $z_A < z_B$)			
1	$x_P > x_B$ and $z_P > z_B$	Tor. and S_B (Fig. 4-22a)	<i>Z-toroidal</i>	$z_{nf} = z_B$
2	$x_P < x_B$ and $z_P < z_B$	Tor. and W_B (Fig. 4-22b)	<i>X-toroidal</i>	$x_{nf} = x_B$
3	$x_P < x_B$ and $z_P > z_B$	Tor. and W_B (Fig. 4-22c) Tor. and W_B (Fig. 4-22d)	<i>X-toroidal</i> <i>Z-toroidal</i>	$x_{nf} = x_B$ $z_{nf} = z_B$
4	$x_P > x_B$; $z_P < z_B$ and $l_W < l_B$	Cyl. and W_B (Fig. 4-22e)	<i>X-Cylindrical</i>	$x_W = x_B$
5	$x_P > x_B$; $z_P < z_B$ and $l_W > l_B$	Cyl. and S_B (Fig. 4-22f)	<i>Z-Cylindrical</i>	$z_W = z_B$
6	$z_C > z_A$; $z_C < z_B$ and $z_P > z_B$	Tor. and S_B (Fig. 4-22g) Tor. and W_B (CC-point)	<i>Z-toroidal</i> <i>X-toroidal</i>	$z_{nf} = z_B$ $x_{nf} = x_B$
7	$z_C > z_A$; $z_C < z_B$ and $z_P > z_B$	Cyl. and S_B (Fig. 4-22h) Cyl. and W_B (CC-point)	<i>Z-Cylindrical</i> <i>X-Cylindrical</i>	$z_W = z_B$ $x_W = x_B$
B.	($x_{n_i} > x_B$ and $z_A > z_B$)			
1	$x_P > x_B$ and $z_P > z_B$	Tor. and W_B (Fig. 4-23a) Tor. and S_B (Fig. 4-23b)	<i>X-toroidal</i> <i>Z-toroidal</i>	$x_{nf} = x_B$ $z_{nf} = z_B$
2	$x_P < x_B$ and $z_P > z_B$	Cyl. and W_B (Fig. 4-23c)	<i>X-Cylindrical</i>	$x_W = x_B$
3	$x_P < x_B$ and $z_P < z_B$	Cyl. and S_B (Fig. 4-23d)	<i>Z-Cylindrical</i>	$z_W = z_B$
C.	($x_{n_i} < x_A$ and $z_A > z_B$)			
1	$x_P < x_A$ and $z_P > z_B$	Tor. and W_A (Fig. 4-23e) Tor. and S_B (Fig. 4-23f)	<i>X-toroidal</i> <i>Z-toroidal</i>	$x_{nf} = x_A$ $z_{nf} = z_B$
2	$x_P > x_B$ and $z_P > z_B$	Cyl. and W_B (Fig. 4-23g)	<i>X-Cylindrical</i>	$x_W = x_B$
3	$x_P > x_B$ and $z_P < z_B$	Cyl. and W_A (Fig. 4-23h) Cyl. and S_B	<i>X-Cylindrical</i> <i>Z-Cylindrical</i>	$x_W = x_A$ $z_W = z_B$
D.	($0 < \lambda_W < 90$ and $z_A > z_B$)			
1	$z_C < z_B$ and $x_P > x_B$	Tor. and S_B (n_B) (Fig. 4-23i) Cyl. and W_B (n_W)	<i>Z-toroidal</i> <i>X-Cylindrical</i>	$z_{nf} = z_B$ $x_W = x_B$
2	$z_C < z_B$ and $x_P < x_B$	Tor. and S_B (n_B) (Fig. 4-23j) Tor. and W_B (n_W)	<i>Z-toroidal</i> <i>X-toroidal</i>	$z_{nf} = z_B$ $x_{nf} = x_B$

Others circumstances are shown by case A.6 and A.7. Even though C is located above S_A , but it cannot be concluded that there is no engagement. The tool may engage with block B. In both cases, the LE-point move from C_f to C_f' . Consequently, the coordinate of C_f' need to be calculated. The toroidal angle of C_f' for case A.6 is obtained using the *X-toroidal method* with $x_{nf} = x_B$. On the other hand, because the LE-point is located on the cylindrical side, the *X-cylindrical method* with $x_W = x_B$ is used to calculate the LE-point for A.7.

Although the initial assumption that n_i is located on S_A , it is possible that some part of cutting tool in between the engagement points is out of the workpiece as depicted by Fig. 4-23i and Fig. 4-23j, this is occurred when $0 < \lambda_W < 90$. In this case, there are two more points that need to be determined: the engagement points on S_B (n_B) and the engagement point on W_B (n_W).

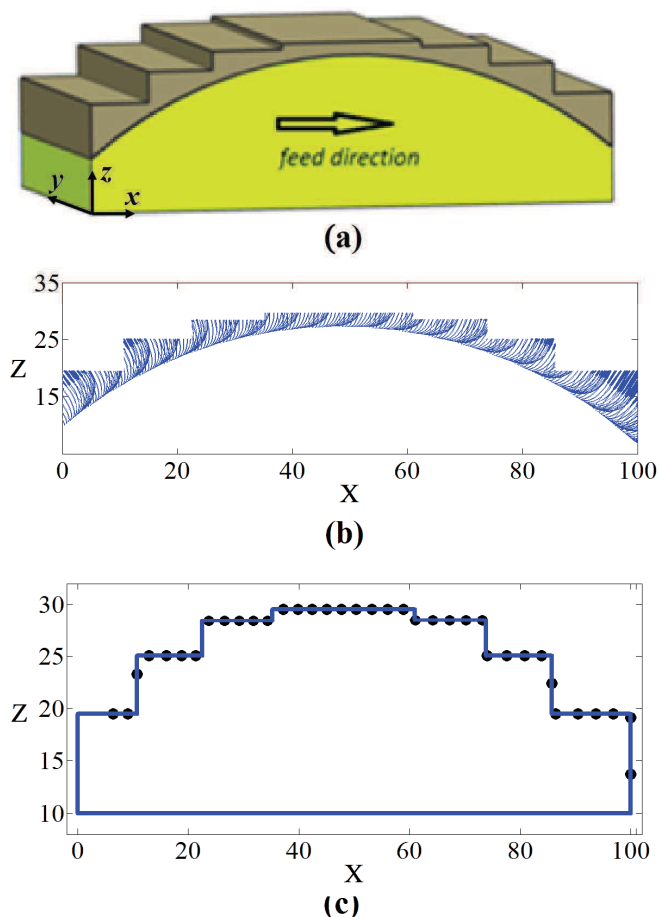


Fig. 4-24 Test model 1; a) Parts and workpiece for test model; b) CWE progression for one tool pass; c) verification

4.4.2.3. Application and Discussion

A one part with a surface profile, as shown in Fig. 4-24a, was tested. In this test, the tool was set normal to the part surface. Machining conditions used in the test were feedrate 0.3 mm/tooth and cutting speed 5000 rpm. Two teeth toroidal cutter with diameter 20 mm and minor radius 5 mm was employed as cutting tool.

Using the developed simulation program, Analytical Boundary Simulation (ABS), the shape and length of cut can be generated. The shapes of cut, which were generated using the ABS, are shown in Fig. 4-24b. It can be seen that the shape of cut geometry on the top side resembles the shape of workpiece surface and the one at the bottom side resembles the part surface. Once again, this is an indication that the proposed model was accurate.

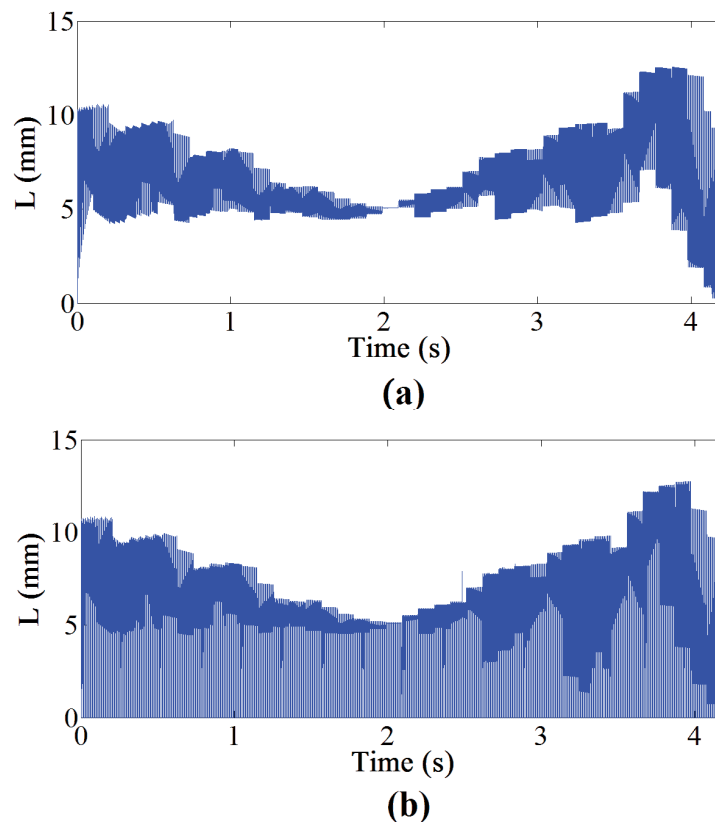


Fig. 4-25 The length of cut progression (L), a) without helical angle, b) with helical angle

Even though the result indicated that the proposed model was accurate, the verification was kept performed. Using the same method that was applied for semi finish with a flat-end tool, two verification tests were also accomplished in this

section. Fig. 4-24c depicts the verification result in which the location of the UE-point for every CC-point at $\varphi = 90$ were compared with respect to the workpiece surface. From this graph, it can be seen that all of the UE-points are located exactly on the workpiece surface. To prove the accuracy of the proposed method, a second verification procedure using Siemens-NX was also performed and good agreement was found.

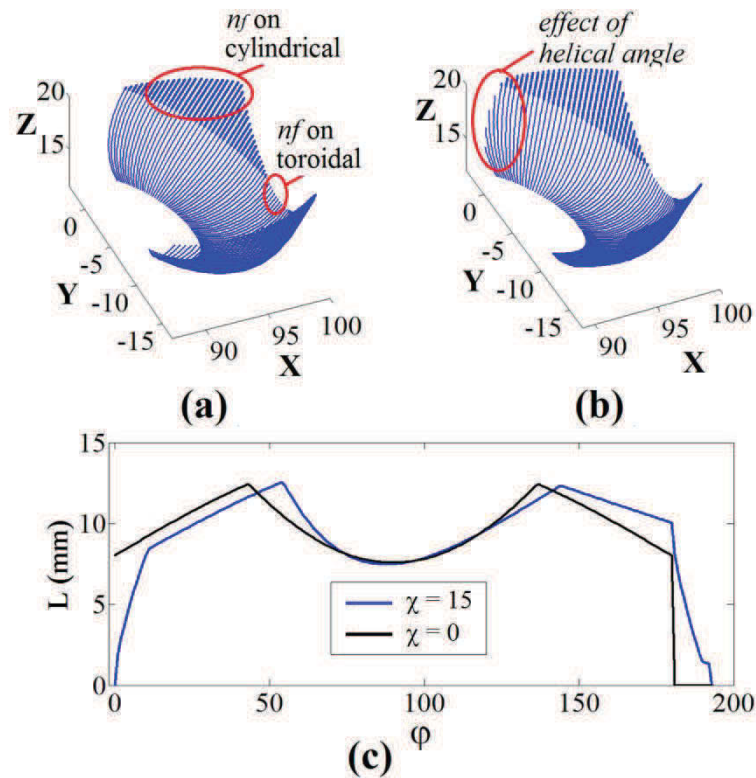


Fig. 4-26 CWE from CC-37 a) the shape of cut without helical angle, b) the shape of cut with helical angle, and c) the length of cut (L) as a function of engagement angle

The tool orientation and the workpiece surface changed continuously make the length of cut fluctuate significantly during machining, as presented in Fig. 4-25. The length of cut progressions, which were generated for the tool without the helical angle and that with helical angle 15° , are presented in (Fig. 4-25a) and (Fig. 4-25b), respectively. It can be seen that the helical angle changed the profile of length of cut progression. When the tool without the helical angle, the tool engaged the workpiece completely since beginning. When the helical angle exists, however, the tool engaged with the workpiece gradually. The effect

of helical angle to the length of cut, as presented in Fig. 4-25, can be analyzed more clearly using Fig. 4-26.

The shapes of cut geometry with respect to the engagement angle for CC-37 are displayed in Fig. 4-26. The shape of cut, which were generated using the tool without the helical angle and that with the helical angle 15° , are depicted in Fig. 4-26a and Fig. 4-26b. The effect of a helical angle on the shape of cut, which is highlighted in Fig. 4-26b, can be analyzed more clearly using the graph of the lengths of cut in Fig. 4-26c. When the tool without a helical angle, the length of cut are relatively larger since the tool enters to the workpiece. Meanwhile when a helical angle exist, the length of cut start from zero and then increase gradually. The CWE is still occurred at the engagement angle more than 180° . In this case, the tool exits totally from the workpiece at $\varphi = 192^\circ$. This figure answers the reason why the graphs in Fig. 4-25a and Fig. 4-25b are different.

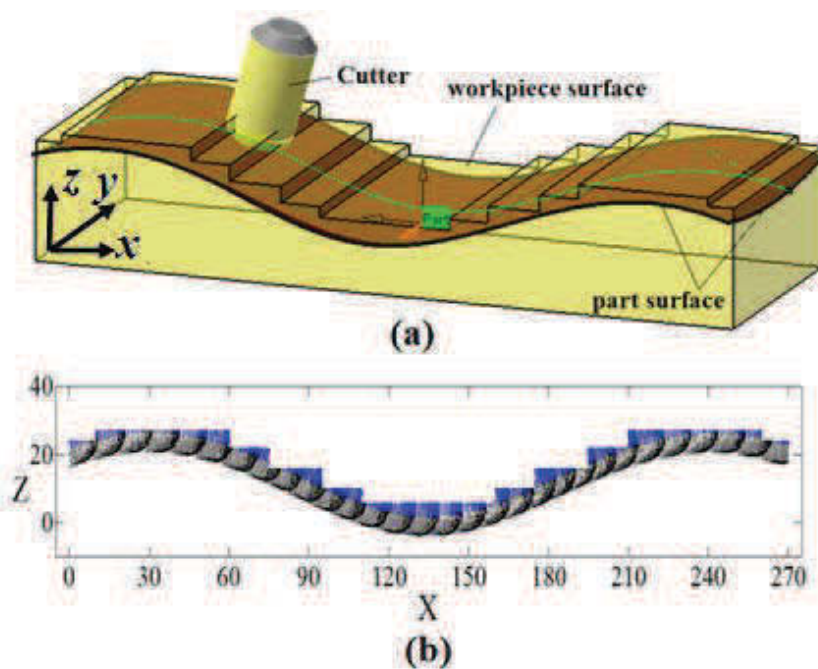


Fig. 4-27 Test model 2; a) Parts and workpiece for test model;
b) CWE progression for one tool pass

The cut with straight and thick line on the top, which is highlighted in Fig. 4-26a, indicates that the UE-point is located on the cylindrical side. In this case, the CWE occurred on both the cylindrical and toroidal sides. If there is no such line on the top, it mean that the engagement only occurred on the toroidal side.

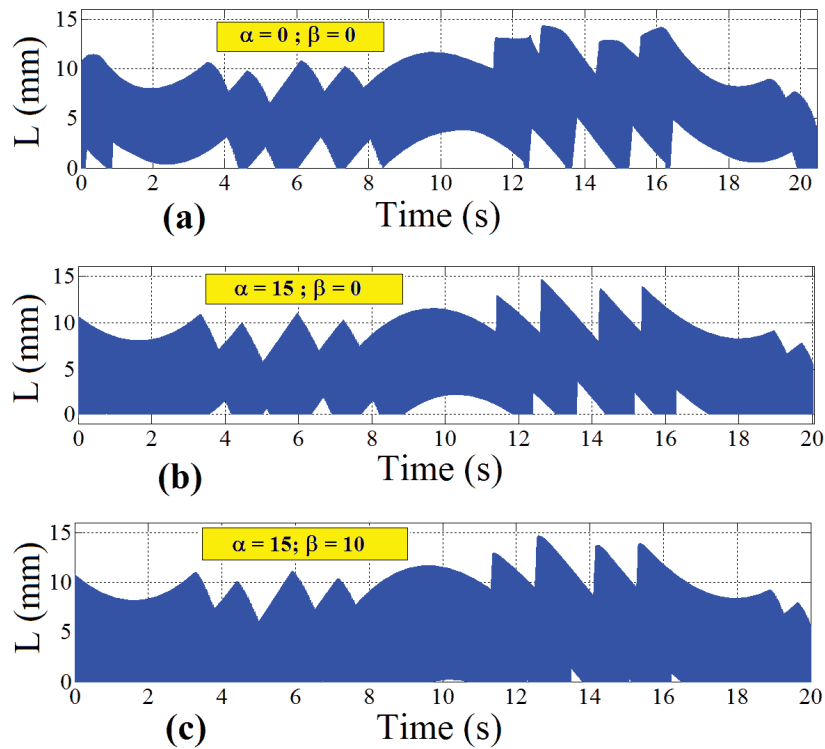


Fig. 4-28 The length of cut progression (L) from (a) Test A ($\alpha = 0$; $\beta = 0$), (b) Test B ($\alpha = 15$; $\beta = 0$), (c) Test C ($\alpha = 15$; $\beta = 10$)

Another test using a more complex part and workpiece surface, which is presented in Fig. 4-27a, was also performed. Machining conditions used in the test were feedrate 0.2 mm/tooth and spindle speed 4000 rpm. A two teeth toroidal cutter with a diameter 25 mm and minor radius 6 mm was employed as cutting tool. The shapes of cut that were generated using the program simulation are presented in Fig. 4-27b. In this figure, the tool was set with an inclination angle (α) = 0 and a screw angle (β) = 0.

Using the same part and workpiece model, the proposed method was tested using several combination of inclination angle and screw angle. The length of cut progression for all combinations, which were generated using ABS, are presented in Fig. 4-28a ($\alpha = 0$; $\beta = 0$ /Test A), Fig. 4-28b ($\alpha = 15$; $\beta = 0$ /Test B), and Fig. 4-28c ($\alpha = 15$; $\beta = 10$ /Test C). In these graphs, the CWE data were generated for every 8×10^{-5} second of tool motion. It can be seen that each graph shows a different profile. This was occurred because the existence of inclination angle and screw angle changed the instantaneous tool orientation angles (θ_A and

θ_B), and the tool orientation angles influence largely both the UE-point and LE-point. Hence, obviously, it changed the instantaneous length of cut. This condition can be explained clearly by referring to Fig. 4-29.

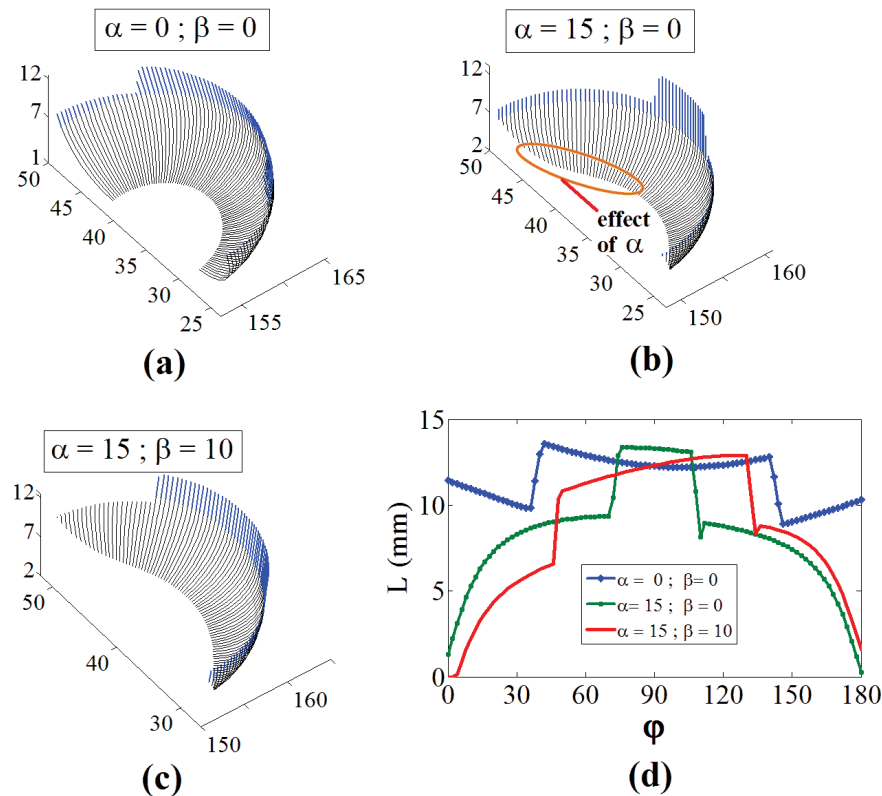


Fig. 4-29 Geometry of cut (a) Test A, (b) Test B, (c) Test C, and (d) the length of cut (L) for CC-35

Fig. 4-29 displays the shape and length of cut as a function of engagement angle for CC-point 35. In this figure, the shapes of cut for all combinations of the tool orientation angles, which were generated using ABS, are presented. Fig. 4-29a shows the shape of cut for *Test A*. It can be seen that the shape of cut at the bottom side resemble the shape of the bottom side of a cutting tool. Different phenomena are showed by Fig. 4-29b (*Test B*) and Fig. 4-29c (*Test C*). When an inclination angle exists, the location of the LE-point become very dynamic. Hence, the shape of cut at the bottom side does not resemble the shape of bottom side of a cutting tool. Fig. 4-29d presents the length of cut for all of the tests. Because *Test A* was set without an inclination angle, it produced relatively longer cut as compared to *Test B* and *Test C*. The inclination angle makes the length of

cut on the toroidal side smaller. Moreover, the existence of a screw angle in *Test C* makes the graph of the length of cut was not symmetrical.

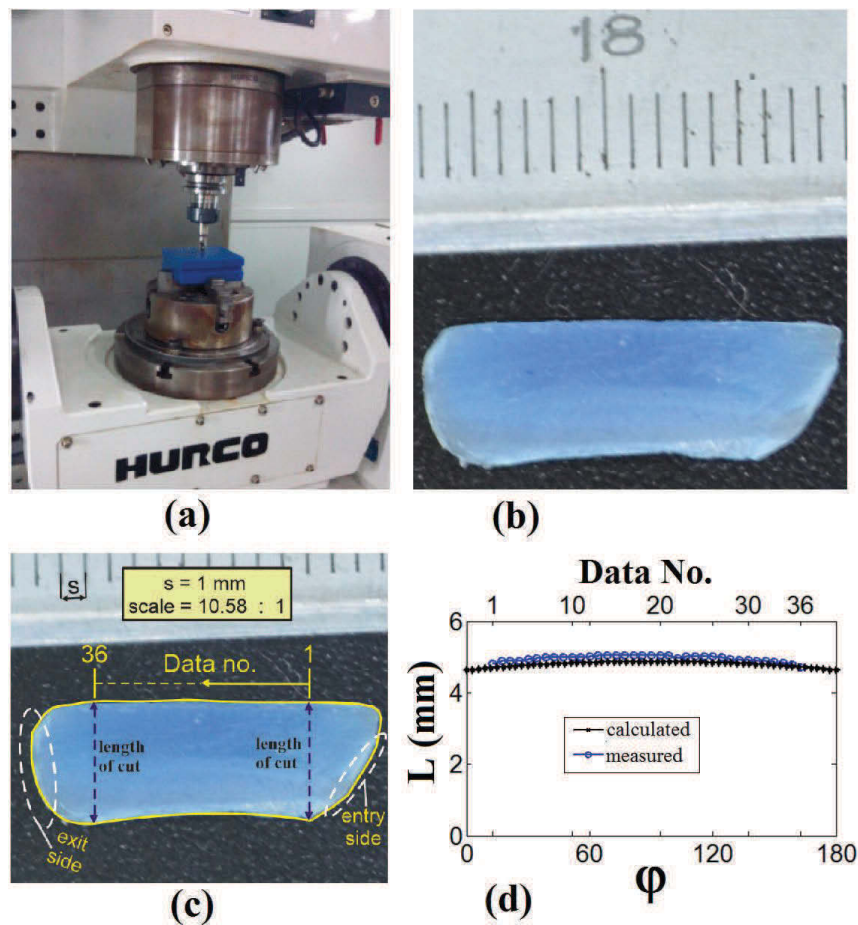


Fig. 4-30 The real machining verification, a) experimental setup, b) chip from machining, c) chip measured using Corel Draw X3, d) comparison of calculated and measured the length of cut

4.4.2.4. Experimental Verification

The accuracy of the proposed model was also verified experimentally by comparing the length of cuts that were calculated using ABS with those were obtained from the real machining test. For this purpose, a machining test has been performed using a five axis milling (Hurco VMX 30U - belong to Universitas Negeri Jakarta, Indonesia), as presented in Fig. 4-30a. The machining conditions used for the experimental were feedrate 0.2 mm/tooth and cutting speed 1000 rpm. A two teeth toroidal cutter with major radius 6 mm and minor radius 2 mm

was used as the cutting tool. To obtain a good shape of the cut geometry from a machining process, a soft material, which is acrylonitrile butadiene styrene (ABS), was selected. The shape of chip from the experimental work is depicted in Fig. 4-30b. This figure was captured using Camera Nikon D5100.

Because the material was soft, some part of chip were damaged especially on the side when the tool enter and exit the workpiece material, as highlighted in Fig. 4-30c. Therefore, the length of cut was only measured at the middle side of the chip. It is impossible to define the length of cut as a function of engagement angle from the chip that was obtained from the experimental work. Hence, the length of cut data was labeled using data number.

Thirty six data were measured using CorelDraw X3. The measurement was calibrated using a vernier caliper that was also captured with the chip as can be seen in Fig. 4-30c. The calibration was performed to define the magnification of the image, and it was found that the scale of the image was 10.58 :1. Then, the actual length of cut was determined by dividing the length of cut that was measured using CorelDraw X3 with the scale of the image. Fig. 4-30d shows the comparison of the calculated and measured length of cuts. From this graph can be seen that both of them have a good agreement. In general, the deviations were less than 4%.

4.4.2.5. Comparison with Z-Mapping Method

The main objective of the researches on the analytical method for the CWE generation is intended to solve the issue regarding the long computational time that normally arise when using a solid model and a discretization method. Therefore, to ensure the efficiency of the proposed method over the existing one, computational times were compared to the Z-mapping method. Z-mapping is a discretization method that is powerful for generating CWE [22]. As mentioned in the introduction, the computational time of a discretization method is largely influenced by the grid size selection, which is dependent on the required accuracy. On the other hand, with the analytical method described in this study, there is no need to select a grid size; therefore there is no correlation between the grid size and the computational time.

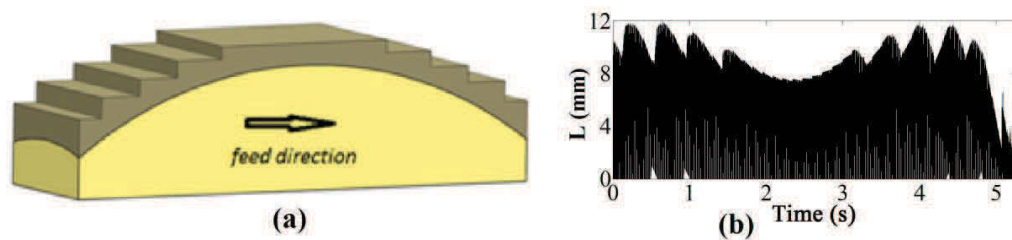


Fig. 4-31 Part model for computational time test

For comparison purposes, the CWE for a part design and a workpiece surface, as presented in Fig. 4-31a, were generated using both the ABS and the Z-mapping method. For this test, a two teethed toroidal cutter with a diameter 20 mm and minor radius 5 mm was employed as cutting tool. The simulation was performed using cutting speed 5000 rpm and feedrate 0.3 mm/tooth. The tool was set incline with the inclination angle 10° relative to the surface normal. For the Z-mapping method, the workpiece surface was discretized with a grid size of 0.1 mm. Both the ABS and Z-mapping methods were performed using Matlab on Intel Core i5 1.7 GHz laptop with 6 GB RAM. An uninterrupted test from CC-1 to CC-47 was carried out and the computational time in between two consecutive CC-points was recorded. This measurement was repeated three times for every method and the average results are presented in Fig. 4-32.

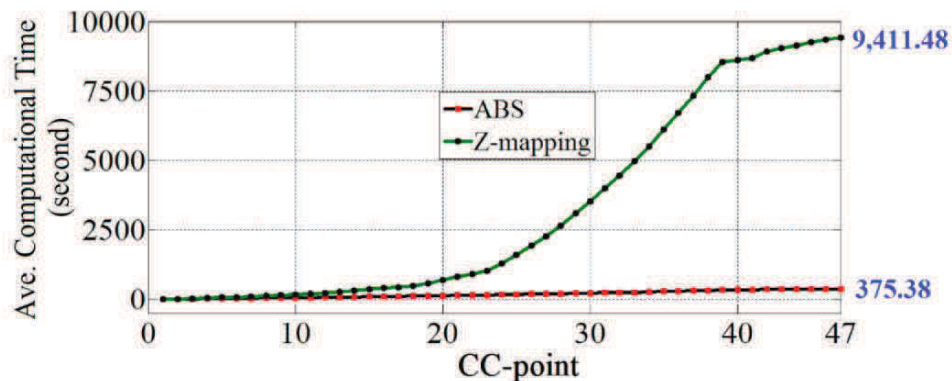


Fig. 4-32 Comparison of average computational time between ABS and Z-mapping

From the graph in Fig. 4-32 can clearly be seen that the computational time for ABS was much shorter than the Z-mapping method. The ABS took only 375.38 second to generate the length of cut as presented in Fig. 4-31, while Z-mapping took 9,411.48 second. Z-mapping was not a fast algorithm because it has to calculate and update a large amount of data. On the other hand, using analytical

method, the CWE was calculated directly from a combination of parametric equation of the cutting tool, tool orientation data and mathematic equation of the workpiece surface, which were discussed in the previous sections. This is the main advantage of the analytical method over the discrete method.

In this test, the intensity of the CWE data generated by ABS was set at 3.33×10^{-5} seconds of the tool motion or 1° of tool rotation. If necessary, the intensity of the CWE data can be reduced, and obviously the computational time will also decrease. Reducing the intensity in analytical method will not decrease the accuracy.

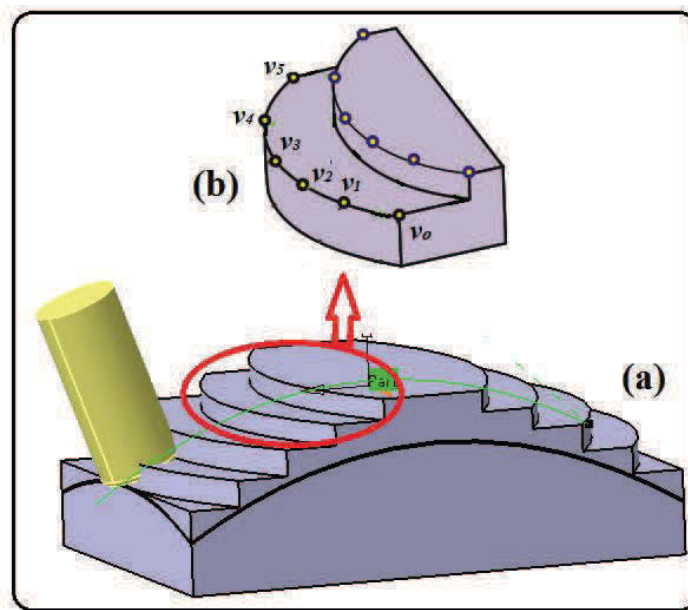


Fig. 4-33 Non straight staircase workpiece surface

4.5. Semi-Finish Milling with a Non-Straight Staircase Profile

When machining a free-form surface part, the shape of workpiece surface, which is produced by rough milling, can be a non-straight (curve) staircase profile instead of a straight staircase as presented in Fig. 4-33a. This profile is obtained depend on the machining strategy that is applied during rough milling. A curve workpiece surface is normally produced by 3D rough milling that is aimed to obtain lower chip load variation during semi-finish milling. In this study, the shape of the wall surface in every stair level is represented by six points that are located on the top of the wall surface as illustrated in Fig. 4-33b. Based on the

coordinate of the representative points, a mathematic equation to define the shape of the wall surface is developed using a polynomial equation. A flowchart describing the steps to obtain the CWE points is presented in Fig. 4-12. The details will be given in the subsequent sections.

4.5.1. Curve Surface Representation

A fundamental mathematical technique is to approximate something complex by something simple, or at least complex, in the hope that the simple can represent some of the essential information in the complicated. The wide spread used of computers has made the idea of approximation even more important.

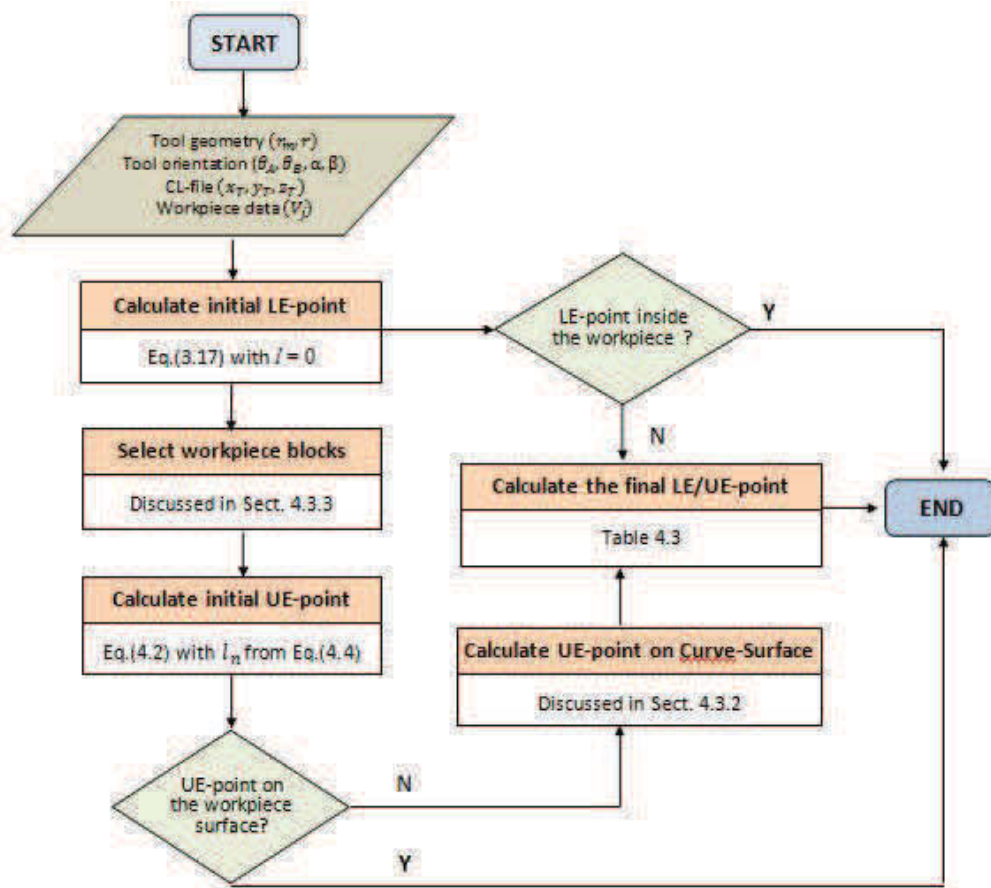


Fig. 4-34 Flow chart to obtain the CWE point for a non-straight staircase

As mentioned before that the wall of the workpiece surface is represented by a non-straight staircase profile, which is a curve from polynomial interpolation.

Interpolation is a problem of creating a function that belonging to a (simple) finite dimensional linear space from given set of data. Because a wall surface along a tool path is represented by a number of points, the shape of wall surface is constructed by 3th degree of polynomial curve fitting that constructed from a six given point. The number of points to represent the wall surface can be increased to get more accurate result. A 3rd degree of polynomial curve fitting has the form,

$$x_j = H_{0j} + H_{1j} y_j + H_{2j} y_j^2 + H_{3j} y_j^3 \quad (4-40)$$

where $j(1, \dots, n)$ represents the order of the workpiece blocks. Because the profile of the wall surface in every block may be different. To calculate the H_{0j}, \dots, H_{3j} , four linear equations in matrix form was set up as follows,

$$\begin{bmatrix} n & \sum y_{ij} & \sum y_{ij}^2 & \sum y_{ij}^3 \\ \sum y_{ij} & \sum y_{ij}^2 & \sum y_{ij}^3 & \sum y_{ij}^4 \\ \sum y_{ij}^2 & \sum y_{ij}^3 & \sum y_{ij}^4 & \sum y_{ij}^5 \\ \sum y_{ij}^3 & \sum y_{ij}^4 & \sum y_{ij}^5 & \sum y_{ij}^6 \end{bmatrix} \begin{bmatrix} H_{0j} \\ H_{1j} \\ H_{2j} \\ H_{3j} \end{bmatrix} = \begin{bmatrix} \sum x_{ij} \\ \sum (y_{ij} x_{ij}) \\ \sum (y_{ij}^2 x_{ij}) \\ \sum (y_{ij}^3 x_{ij}) \end{bmatrix} \quad (4-41)$$

where n is the number of representative points and $i = 1, \dots, n$.

4.5.2. Curve Boundary Method

In the case of a non-straight staircase, the UE-point on the top surface is defined using the *Z-cylindrical* method that was discussed in the previous section. However, when the UE-point point is identified on the wall surface, the *X-cylindrical* method for a straight staircase is not applicable. In this case, the UE-point is calculated using a method called the *Curve Boundary* Method. In this method, the intersection point between the wall surface and the cutting tool is occurred when (x'_{S_C}, y'_{S_C}) in Eq.(3-17) is equal to (x_j, y_j) in Eq.(4-40). The *Curve Boundary* Method is aimed to define the length of CWE (l_n) that will be used to calculate the UE-point. Therefore, x'_{S_C}, y'_{S_C} in Eq.(3-17) is expanded to become,

$$\begin{bmatrix} x'_{S_C} \\ y'_{S_C} \end{bmatrix} = \begin{bmatrix} R \sin \varphi \cos \theta_B + l_n \sin \theta_B + x_T \\ R \cos \varphi \sin \theta_A \sin \theta_B + R \cos \varphi \cos \theta_A - l_n \sin \theta_A \cos \theta_B + y_T \end{bmatrix} \quad (4-42)$$

To simplify the equations, some parts of x'_{S_C} and y'_{S_C} in Eq.(4-42) are represented by,

$$\begin{aligned} a &= R \sin \varphi \cos \theta_B + x_T \\ b &= R \cos \varphi \sin \theta_A \sin \theta_B + R \cos \varphi \cos \theta_A + y_T \end{aligned} \quad (4-43)$$

Then x'_{S_C} and y'_{S_C} yield to become,

$$\begin{bmatrix} x'_{S_C} \\ y'_{S_C} \end{bmatrix} = \begin{bmatrix} a + l_n \sin \theta_B \\ b - l_n \sin \theta_A \cos \theta_B \end{bmatrix} \quad (4-44)$$

The intersection point is obtained by insert the value of x'_{S_C} and y'_{S_C} from Eq.(4-44) into x_j and y_j in Eq.(4-40). Then Eq.(4-40) changes to become,

$$\begin{aligned} a + l_n \sin \theta_B &= H_0 + H_1 (b - l_n \sin \theta_A \cos \theta_B) \\ &+ H_2 (b - l_n \sin \theta_A \cos \theta_B)^2 \\ &+ H_3 (b - l_n \sin \theta_A \cos \theta_B)^3 \end{aligned} \quad (4-45)$$

The equation above was rearranged to become,

$$0 = K_0 + K_1 l_n + K_2 l_n^2 + K_3 l_n^3 \quad (4-46)$$

where :

$$\begin{aligned} K_0 &= H_0 + H_1 b + H_2 b^2 + H_3 b^3 - a \\ K_1 &= (-H_1 - 2H_2 b - 3H_3 b^2) \sin \theta_A \cos \theta_B - \sin \theta_B \\ K_2 &= (H_2 + 3H_3 b) \sin^2 \theta_A \cos^2 \theta_B \\ K_3 &= (-H_3) \sin^3 \theta_A \cos^3 \theta_B \end{aligned} \quad (4-47)$$

The roots of polynomial can be easily determined using software programming such as Matlab. Then the length of CWE is obtained by,

$$l_n = \text{roots} [K_3 \quad K_2 \quad K_1 \quad K_0] \quad (4-48)$$

The Eq.(4-48) produces three roots of l_n . Among those roots, however, only one l_n that is applicable for obtaining the CWE point correctly. The correct one is selected by following these rules,

- i. l_n must be real and positive,
- ii. if more than one l_n fulfill the criteria *i*, then the smallest one is selected.

Once l_n is obtained, then the engagement point is calculated using Eq.(4-23).

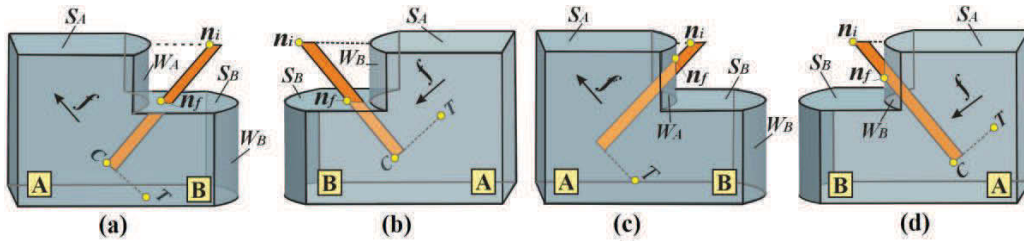


Fig. 4-35 Location of the UE-point when $z_A > z_B$

4.5.3. Obtaining the Engagement Point

In the beginning, the polynomial equation for every wall surface in one tool pass should be determined. The procedure to obtain the engagement points is begun by first defining two workpiece blocks that have potential engage with the cutting tool. The workpiece block is identified by comparing the coordinate of x_C from $C(x_C, y_C, z_C)$ with the coordinate of the wall surface x_j in Eq.(4-40). x_j is calculated using $y_j = y_C$. Block A is selected when $x_C > x_j$. Meanwhile block B is located next to block A when θ_B is positive, and before block A when θ_B is negative.

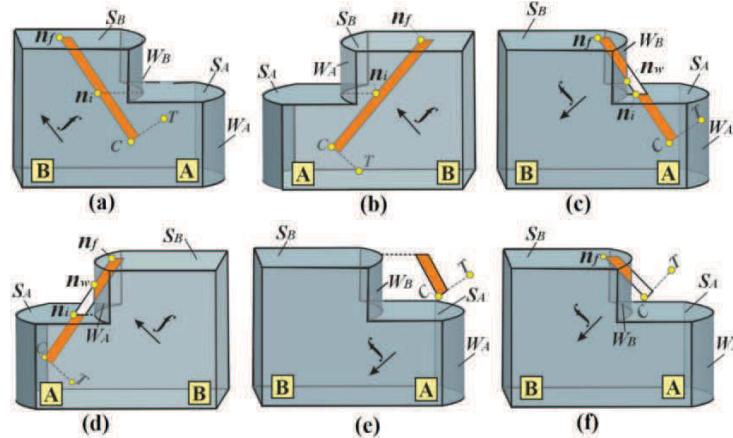


Fig. 4-36 Location of the UE-point when $z_A < z_B$

Similar to semi finish method, the UE-point is calculated by assuming that it is located on the top surface of block A (S_A). Then the *Z-cylindrical* method (Eq.(4-25)) is used to calculate l_n . After l_n is obtained, the initial UE-point, $n_i(x_{n_i}, y_{n_i}, z_{n_i})$, is then calculated using Eq.(4-23). After that, it is checked to determined whether or not it is on S_A . The checking step is performed by

calculating the coordinate of x_j using $y_j = y_{n_i}$. When θ_B is positive, x_j is calculated using the curve equation of block B (W_B), and the result called x_{jB} . On the other hand, when θ_B is negative, it is calculated using the curve equation of block A (W_A), then the result is called x_{jA} .

Table 4-3 Method to identify and calculate CWE for curve surface

No.	Indication	Location of the UE-point	l_n
$Z_A > Z_B$			
A.1	$x_{n_i} < x_{jA}, z_{n_i} > z_B, z_{n_w} < z_B$	S_B (Fig. 4-35a)	$l_n = l_B$
A.2	$x_{n_i} > x_{jB}, z_{n_i} > z_B, z_{n_w} < z_B$	S_B (Fig. 4-35b)	$l_n = l_B$
A.3	$x_{n_i} < x_{jA}, z_{n_i} > z_B, z_{n_w} > z_B$	W_B (Fig.	$l_n = l_W$
A.4	$x_{n_i} > x_{jB}, z_{n_i} > z_B, z_{n_w} > z_B$	W_B (Fig. 4-35d)	$l_n = l_W$
$Z_A < Z_B$			
B.1	$x_{n_i} > x_{jB}, z_{n_w} < z_A < z_B$ and $z_C < z_A$	S_B (Fig. 4-36a)	$l_n = l_B$
B.2	$x_{n_i} < x_{jA}, z_{n_w} < z_A < z_B$ and $z_C < z_A$	S_B (Fig. 4-36b)	$l_n = l_B$
B.3	$x_{n_i} < x_{jB}, z_A < z_{n_w} < z_B$ and $z_C < z_A$	W_B and S_B (Fig. 4-36c)	$l_n =$ $l_B - (l_W - l_A)$
B.4	$x_{n_i} > x_{jB}, z_{n_w} < z_A < z_B$ and $z_C < z_A$	W_A and S_B (Fig. 4-36d)	$l_n =$ $l_B - (l_W - l_A)$
B.5	$z_C > z_A$ and $z_w > z_B$	None (Fig. 4-36e)	$l_n = 0$
B.6	$z_C > z_A$ and $z_w < z_B$	S_B (Fig. 4-36f)	$l_n = (l_B - l_A)$

The initial UE-point is wrong if $x_{n_i} < x_{jA}$ when θ_B is negative, or $x_{n_i} < x_{jA}$ when θ_B is positive. In these cases, the final UE-point, $n_f(x_{n_f}, y_{n_f}, z_{n_f})$, need to be recalculated. Because the UE-point can be located on the wall surface, then the engagement point when it is on the wall surface,

$n_w(x_{n_w}, y_{n_w}, z_{n_w})$, need to be determined. It can be defined after the length of cut on the wall surface is calculated using the *curve boundary* method. Finally, some conclusion regarding the CWE, when the initial assumption is wrong, can be taken. All of the CWE conditions for a curve surface are illustrated in Fig. 4-35 and Fig. 4-36.

Table 4-3 presents the method to identify the final engagement point for the conditions as illustrated in Fig. 4-35 and Fig. 4-36. The procedures that are explained in this table is similar to that use in the case of straight staircase.

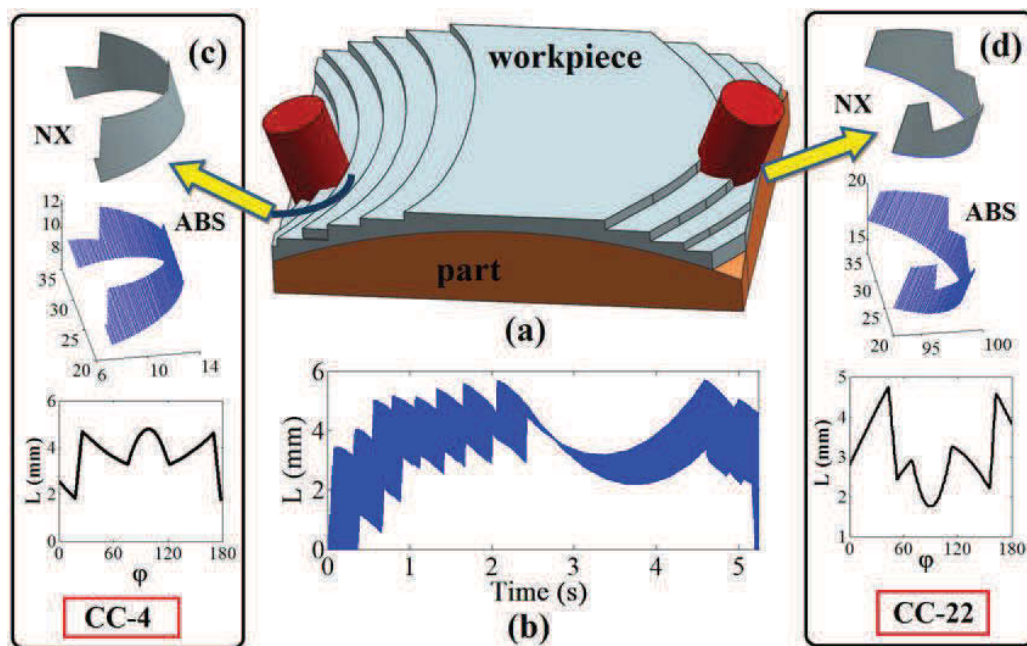


Fig. 4-37 a) Part and workpiece model, b) the length of cut progression, c) the shape and the length of cut for CC-4, and d) for CC-22

4.5.4. Implementation and Discussion

A one part design with a complex surface and workpiece surface, which were obtained from 3D rough milling as shown in Fig. 4-37a, was tested. A two teeth flat-end cutter with 14 mm diameter was employed as cutting tool, and it was set with a constant inclination angle (5°). Machining condition that was used for this implementation were feedrate 0.3 mm/tooth, and cutting speed 5000 rpm.

The *Curve boundary* method for a non-straight staircase profile has been added to Analytical Boundary Simulation (ABS). Using ABS, the length of cuts

for one tool pass were generated and presented in Fig. 4-37b. The shape of cut and the length of cut for one tool rotation are presented in Fig. 4-37c for CC-4 and Fig. 4-37d for CC-22. The shape of cuts, which were generated using ABS, were compared with the one obtained from the extraction model of the intersection between a cutter model and a workpiece model using Siemens-NX. From the two figures can be concluded that the shape of cuts generated using ABS resembled to that obtained using Siemens-NX. From Fig. 4-37 can be seen that the length of cuts are very fluctuates. This is because of the complexity of the part and workpiece surface.

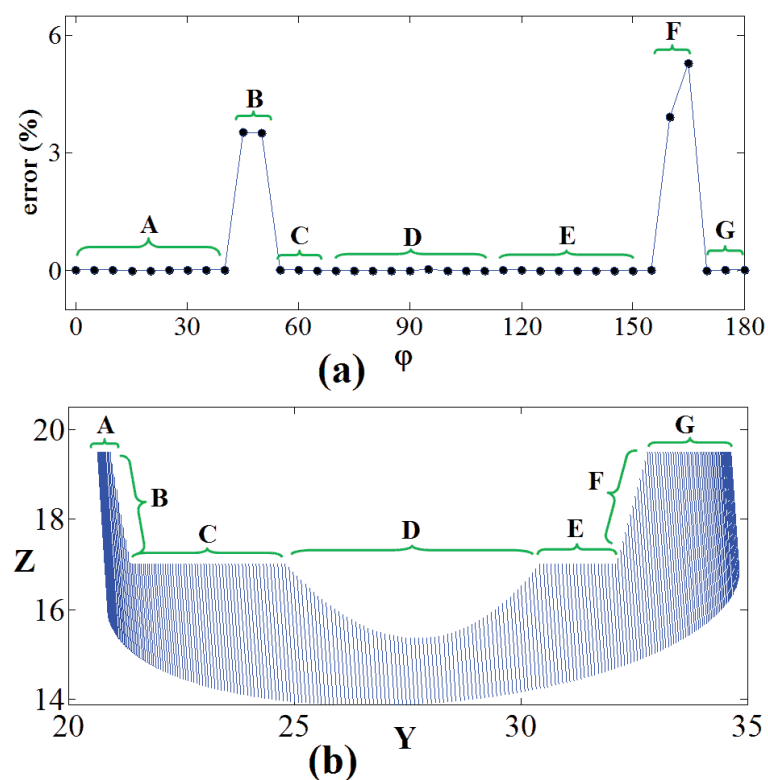


Fig. 4-38 Model verification, a) error of the proposed model, b) the sections of cut

To verify the accuracy of the proposed method, the length of cuts obtained using ABS were compared with the length of cut measured using Siemens-NX. The method to measure the length of cut in Siemens-NX uses the same method that was applied for the case as explained in section 4.4.1.1. For the verification purposes, the length of cut for CC-22 as depicted in Fig. 4-37d was tested as presented in Fig. 4-38a. The error was calculated by dividing the difference

between the length of cut obtained using ABS and the one obtained using Siemens-NX, with the length of cut obtained using Siemens-NX, or it can be expressed as follows:

$$error = \frac{|L_{(ABS)} - L_{(NX)}|}{L_{(NX)}} \times 100\% \quad (4-49)$$

Fig. 4-38b shows the shape of cut generated using ABS. Based on the location of the UE-point, this figure was divided into six sections. Section A, Section C, Section E and Section G are the section where the UE-points are located on the top surface. Meanwhile the UE-points in Section B and Section F are located on the curve-wall surface. Section D shows the shape of cut when the UE-points are located on the straight-wall surface. From this figures can be derived two conclusions:

- a. The accuracy of the proposed method when the UE-points located on a flat-top surface and on a flat-wall surface were very good. For these cases, the error was zero, or can be considered as zero.
- b. A relatively small errors were found when the UE-points were located on the curve-wall surface. Because the approximation method was used to represent the curve-wall surface, the accuracy was largely influenced by the accuracy in predicting the shape of the wall surface. From the verification was found that the errors were less than 6%.

4.6. Conclusion

In this chapter, the method to calculate the coordinate of the LE-point was developed and tested. For a flat cutting tool, the LE-point was always located at the bottom of cutting tool, whether it is with or without an inclination angle. A different phenomena was shown by toroidal cutter. When the tool without an inclination angle, the LE-point is located at the bottom of cutting tool. Meanwhile when an inclination angle exist, its location become very dynamic. The coordinate of the LE-point can be determined after the toroidal angle of the LE-point is defined. The toroidal angle of the LE-point was determined using a method called

the *Grazing* method. The proposed method was tested and the result revealed that the method can be used to define the coordinate of the LE-point.

The methods to generate the UE-point for rough and semi finish milling with a flat-end cutter and a toroidal cutter were also presented in this chapter. During rough milling and semi-finish milling, a method called the *Cylindrical-boundary* was employed to obtain the UE-point for a flat-end cutter or the UE-point for the UE-points on the cylindrical side of the toroidal cutter. On the other hand, the method called the *Toroidal-boundary* was used to calculate the UE-point of toroidal cutter when it is located on the toroidal side.

The algorithm derived in this chapter was used to develop a simulation program called Analytical Boundary Method (ABS). ABS can be used to generate the shape of cut and the length of cut. The accuracy of the proposed model was verified two times: first by comparing the coordinate of the UE-points with respect to the workpiece surface, and the second by employing a commercial CAD software Siemens-NX. The results proved that the proposed method was accurate. The efficiency of the proposed model in generating the CWE was also compared with the Z-mapping method. The result confirmed that the proposed model was more efficient in term of the computational time.

For the case of a non-straight staircase workpiece surface, the shape of the wall surface was determined mathematically using a polynomial curve. The method to define the UE-point when the engagement point located on the wall surface is called the *Curve boundary method*. The method was also verified using Siemens-NX. The result showed that the error for the UE-point located on the wall surface was below 6%.

CHAPTER 5

ANALYTICAL METHOD FOR OBTAINING THE UE-POINT ON FREE-FORM WORKPIECE SURFACE

In five-axis milling, the machining is not only performed to create a sculptured part from a block workpiece material. Machining can be performed for finishing a free-form part from a casting process. Another case is finishing a semi-finish part. A semi-finish machining normally produces a part surface with a constant removal rate for finish machining. When a final part is a free-form surface, the workpiece from semi finish milling is also a free-form surface. Prediction of machining process with a complex part is a challenging. During finish milling, controlling the dimensional accuracy, the gouge prevention and the workpiece surface roughness are the most important criteria. As a result, a finishing process generally spends the largest amount of machining time due to low depth of cut and feed rate [98].

The method proposed in this study is a hybrid method, which is a combination of discretization and analytical method. The workpiece surface is represented using point spreading method as presented in Fig. 5-1a. However, despite the workpiece is discretized using the normal vectors, but there is no calculation to check the intersection between cutter and normal vectors. They are only used as the reference to define the shape of the surface at every CC-point, mathematically. Compare to a full discrete method, the proposed method uses smaller number of normal vectors to represent the workpiece surface. The normal vector can be defined as a point on the workpiece surface that has the orientation relative to the workpiece coordinate system (WCS) in the x -axis (μ_x) and the y -axis (μ_y) as shown in Fig. 5-1b. As mentioned in introduction, all of the workpiece surface data (normal vectors) are assumed to be provided (given). The method to obtain the discrete normal vectors is not discussed in this study.

Small portion of workpiece surface as illustrated in Fig. 5-1a is approximated by a surface that is a combination of the surface shape in the x -axis and the y -axis as presented in Fig. 5-1c. The shape of the surface can be a combination of convex, concave, flat or slope surface. This approximation is used to define the shape of the instantaneous workpiece surface. The method to define the shape of the surface will be discussed in the following section. The detail procedure to obtain the UE-point for flat-end cutter or cylindrical tool is presented by flow chart in Fig. 5-2.

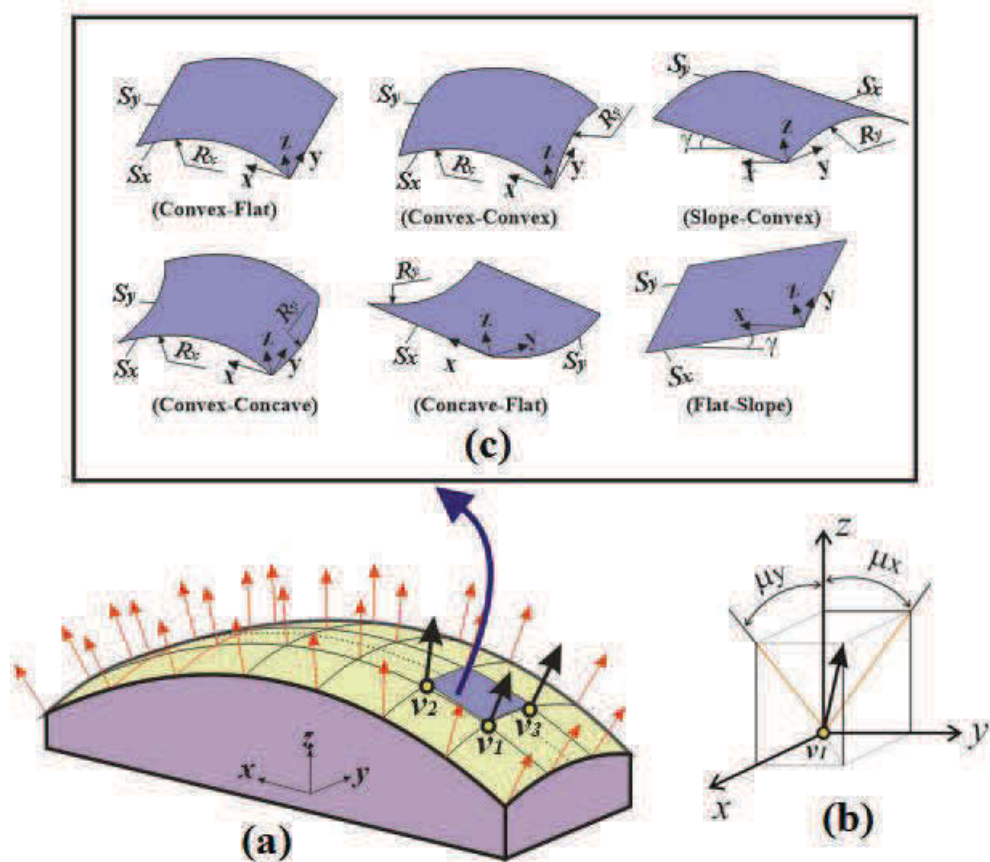


Fig. 5-1 Workpiece surface representation, a) normal vector distribution, b) vector orientation in WCS, d) feasible surface shape combination

5.1. Identifying Instantaneous Surface Shape

At instantaneous tool position, the shape of the workpiece surface should be identified. Fig. 5-3a shows top view of the workpiece surface. The shape of an instantaneous workpiece surface region is defined using three selected normal

vectors (v_1, v_2, v_3) . v_1 is a reference vector that is located closest to the *CC-point*. It can be located inside or outside the cutter region. While v_2 and v_3 are vectors that are located before v_1 .

Based on the coordinate and orientation of the normal surface, the radius of the workpiece surface in the *x-axis* (R_x) is determined using Eq.(5-1). The equations were derived by referring to Fig. 5-3b. Using the same method, the radius of the workpiece surface in the *y-axis* (R_y) is determined using Eq.(5-2).

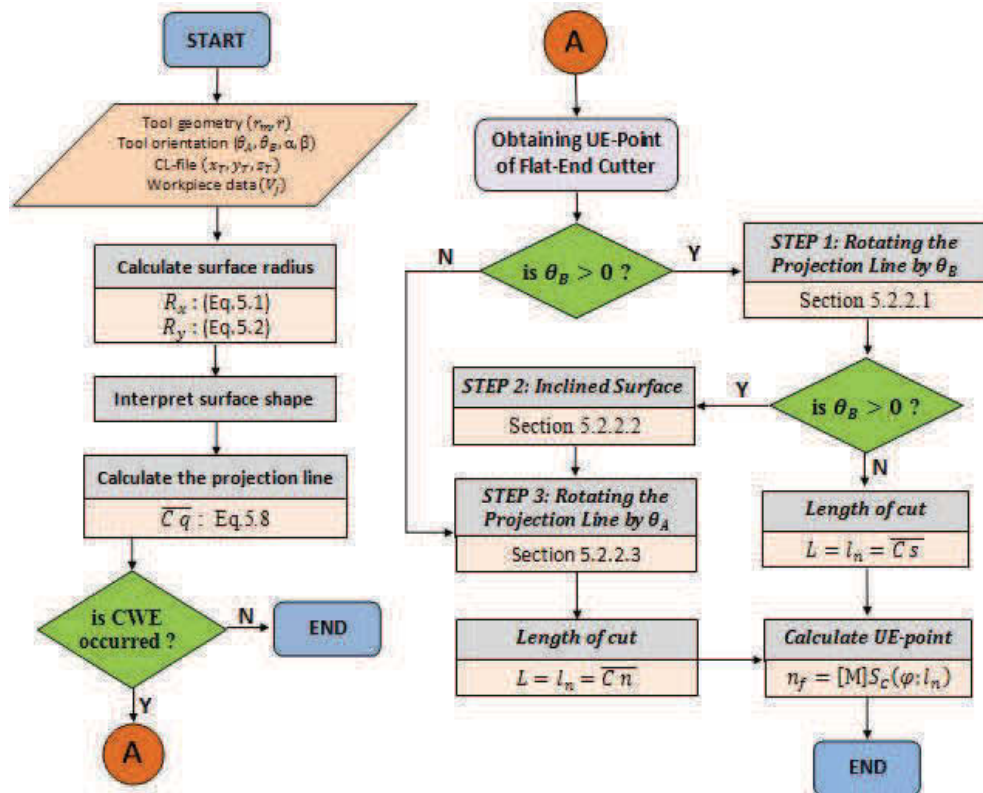


Fig. 5-2 Flow chart to obtain the UE-point of flat-end cutter (cylindrical tool)

$$R_x = \left(\sqrt{(x_2 - x_1)^2 + (z_2 - z_1)^2} \right) / (2 \sin(0.5(\mu_{x2} - \mu_{x1}))) \quad (5-1)$$

$$R_y = \left(\sqrt{(y_3 - y_1)^2 + (z_3 - z_1)^2} \right) / (2 \sin(0.5(\mu_{y2} - \mu_{y1}))) \quad (5-2)$$

After R_x and R_y are obtained, then several conclusions regarding the shape of the workpiece surface in the *x-axis* (S_x) and the *y-axis* (S_y) can be taken.

- Convex surface : if $R_x > 0, R_y > 0$
- Concave surface : if $R_x < 0, R_y < 0$

- Flat surface : if $R_x = 0$ and $\mu_{x1} = 0$; or $R_y = 0$ and $\mu_{y1} = 0$
- Slope surface : if $R_x = 0$ and $\mu_{x1} \neq 0$, slope angle (γ) = μ_{x1} ; or $R_x = 0$ and $\mu_{y1} \neq 0$, $\gamma = \mu_{y1}$

Therefore, the shape of an instantaneous workpiece surface is constructed using a combination of S_x and S_y . Several feasible surface shapes are illustrated in Fig. 5-1c.

The method to identify the selected normal vectors, as illustrated in Fig. 5-3a, is applied when the shape of the workpiece surface at the instantaneous tool location is determined using only one surface region. When the workpiece surface has a high curvature, the shape of the instantaneous surface can be very complex. In this case, the errors can be higher if only one surface region is used to represent one instantaneous workpiece surface. The accuracy of this method is largely influenced by the accuracy in determining the shape of workpiece surface. Therefore, to reduce the error due to the complexity of the surface, the instantaneous workpiece surface can be divided into two or more regions instead of one region. The method to define the shape of the surface for each region is similar as previously discussed. When the surface is separated into several regions, the workpiece surface should be discretized with larger number of normal vector, as illustrated in Fig. 5-3c.

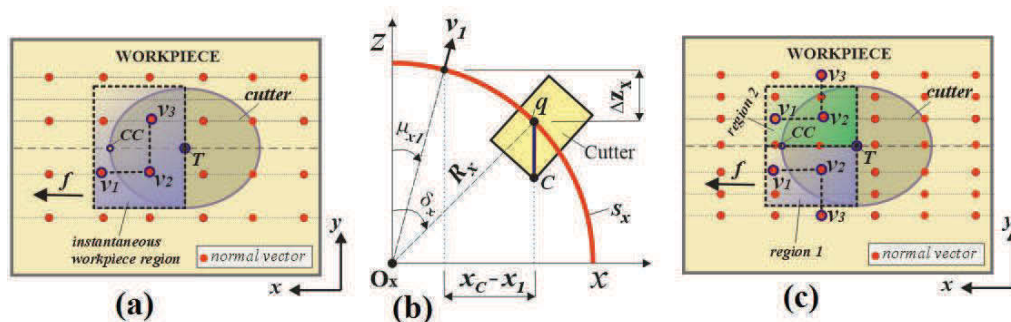


Fig. 5-3 Workpiece surface representation, a) top view of workpiece, b) method to calculate radius of surface, c) surface discretization using two instantaneous workpiece regions

For more simple surfaces such as hemisphere surface, hemi cylindrical surface and flat surface, which have constant curvature shape, they are only required three normal vectors to define the whole surface area. More complex

surface needs more instantaneous workpiece region, and obviously more number of reference vectors.

5.2. Obtaining the UE-Point of A Free-form Surface Machining Using A Flat-End Cutter

Some studies [80, 99] were found that, by changing from three-axis to five-axis milling, efficiency can be improved by 10 to 20 times. Furthermore, a ball end cutting tool which is widely used for free-form surface machining, has disadvantages on low cutting efficiency. So, the flat-end cutter is increasingly paid attention to.

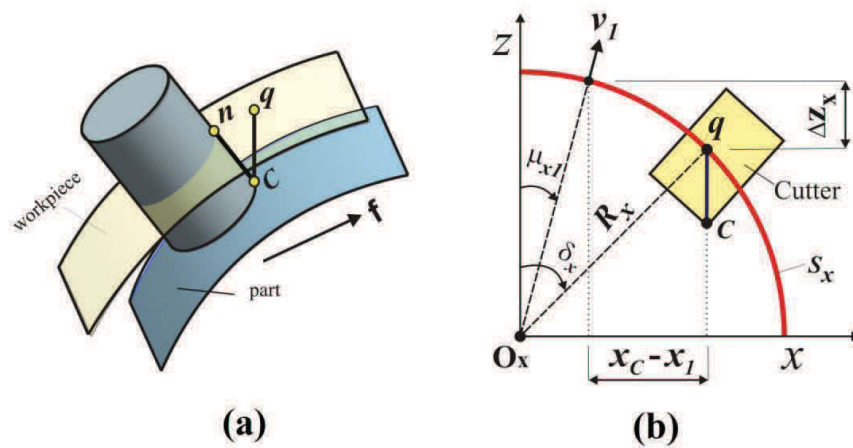


Fig. 5-4 Projection line and location of the UE-point

5.2.1. Checking the Feasible Engagement Location

Before further calculation, at every instantaneous tool position, the cutting tool need to be determined whether or not it engages with the workpiece. It can be defined by calculating a projection point $q(x_q, y_q, z_q)$ as shown in Fig. 5-4. Because q is obtained by projecting point $C(x_c, y_c, z_c)$ in the z -axis, then $\{x_q, y_q\}$ is equal to $\{x_c, y_c\}$. While z_q is obtained by calculating the distance in the z -axis between v_1 and q on S_x (ΔZ_x), and the z -axis on S_y with respect to y_c (ΔZ_y). First, by working on S_x , the z -value can be calculated by comparing x_c with the coordinate and orientation of the reference vector v_1 . The equations to obtain (ΔZ_x) and (ΔZ_y) for a curved surface (concave or convex) is expressed by,

$$\begin{aligned}\delta_x &= \sin^{-1}((R_x \sin \mu_{x1} + (x_c - x_1))/R_x); \\ \delta_y &= \sin^{-1}((R_y \sin \mu_{y1} + (y_c - y_1))/R_y)\end{aligned}\quad (5-3)$$

$$\begin{aligned}\Delta Z_x &= R_x (\cos \delta_x - \cos \mu_{x1}); \\ \Delta Z_y &= R_y (\cos \delta_y - \cos \mu_{y1})\end{aligned}\quad (5-4)$$

δ_x is the angle between the line $\overline{O_x q}$ and the z -axis as depicted in Fig. 5-3b. Meanwhile δ_y is angle between the line $\overline{O_y q}$ and the z -axis. For a slope surface, ΔZ_x and ΔZ_y are determined by,

$$\begin{aligned}\Delta Z_x &= (x_c - x_1) \tan \mu_{x1}; \\ \Delta Z_y &= (y_c - y_1) \tan \mu_{y1}\end{aligned}\quad (5-5)$$

Meanwhile for a flat surface, ΔZ_x and ΔZ_y are equal to zero. Finally, z_q is defined as follows,

$$z_q = z_1 + \Delta Z_x + \Delta Z_y \quad (5-6)$$

After z_q is obtained, thus the length of projection line from C to q is calculated by $\overline{Cq} = z_q - z_c$. The projection line \overline{Cq} will be used as the initial reference line for further calculation to get the UE-points. The engagement is occurred if \overline{Cq} is positive. Otherwise, the cutting edge is located above the workpiece surface and hence there is no engagement between tool and workpiece.

5.2.2. Obtaining the UE-Point

After the projection line is obtained, then it will be rotated by the tool orientation angles (θ_B and θ_A) to obtain the UE-point. These two rotation procedures must be performed sequentially except for a certain conditions it can be skipped and then jump to the next procedure. In this section, the detail procedure to obtain n_f will be derived.

5.2.2.1. STEP 1: Rotating the Projection Line by θ_B

In the first step, to get the line \overline{Cs} , the projection line is rotated about point C by θ_B . If θ_B is equal to zero, then the line \overline{Cs} is equal to line \overline{Cq} . The equations to define the rotated line for every surface shape are expressed below. Using the

trigonometry equations, the length of the lines and angles for a convex surface in Fig. 5-5a are determined by,

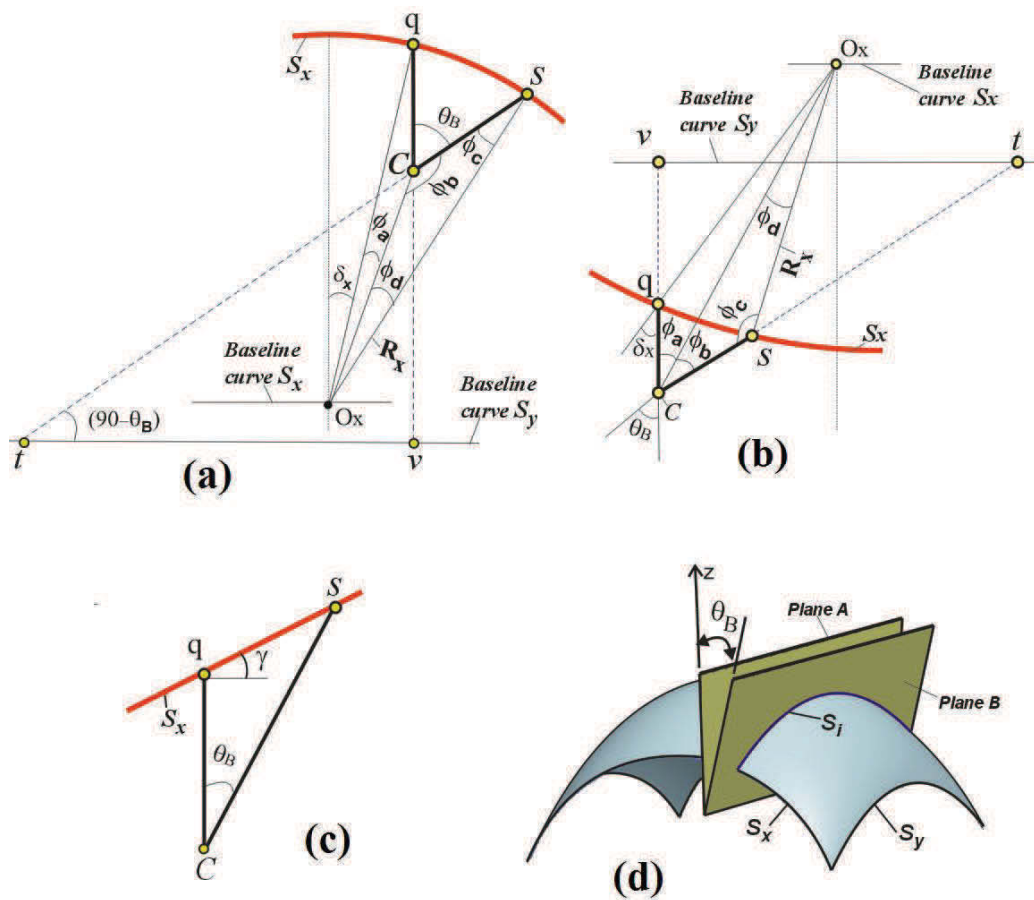


Fig. 5-5 Rotation of the projection line on S_x , a) convex surface, b) concave surface, c) slope surface, d) inclined surface

$$\overline{C O_x} = (\overline{C q}^2 + R_x^2 - 2 \overline{C q} R_x \cos \delta_x)^{0.5} \quad (5-7)$$

$$\phi_a = \cos^{-1}[(\overline{C O_x}^2 + R_x^2 - \overline{C q}^2)/(2 \overline{C O_x} R_x)] \quad (5-8)$$

$$\phi_b = 180 - |\theta_B| - |\delta_x + \phi_a| \quad (5-9)$$

$$\phi_c = \sin(\overline{C O_x} \sin \phi_b / R_x) \quad (5-10)$$

$$\phi_c = \sin\left(\frac{\overline{C O_x} \sin \phi_b}{R_x}\right) \quad (5-11)$$

$$\phi_d = 180 - (\phi_b + \phi_c) \quad (5-12)$$

$$\overline{C s} = (R_x^2 + \overline{C O_x}^2 - 2 R_x^2 \overline{C O_x}^2 \cos \phi_d)^{0.5} \quad (5-13)$$

Meanwhile for a concave surface, the equations to calculate the line $\overline{C s}$ were developed by referring to Fig. 5-5b and they are presented as follows,

$$\overline{C O_x} = (\overline{C q}^2 + R_x^2 - 2 \overline{C q} R_x \cos \delta_x)^{0.5} \quad (5-14)$$

$$\phi_a = \sin^{-1}(R_x^2 \sin(180 - \delta_x) / \overline{C O_x}) \quad (5-15)$$

$$\phi_b = |\theta_B - \phi_a| \quad (5-16)$$

$$\phi_c = 180 - \sin^{-1}(\overline{C O_x} \sin \phi_b / R_x) \quad (5-17)$$

$$\phi_d = 180 - (\phi_b + \phi_c) \quad (5-18)$$

$$\overline{C s} = \overline{C O_x} \sin(\phi_d) / \sin \phi_c \quad (5-19)$$

More simple equations are used to calculate the line $\overline{C s}$ for a slope surface and a flat surface as depicted in Eq.(5-20) and Eq.(5-21), respectively. For a slope surface, the equation was derived by referring to Fig. 5-5c.

$$\overline{C s} = \overline{C q} \sin(90 + \gamma) / \sin(90 - \gamma - \theta_B) \quad (5-20)$$

$$\overline{C s} = \overline{C q} / \cos \theta_B \quad (5-21)$$

5.2.2.2. STEP 2: Inclined Surface

If θ_B is not equal to zero, it means that the projection line has been rotated in the first step. Because of this rotation, the projecting line is not perpendicular to the second surface (S_y). Consequently, when S_y is a curved surface, the line $\overline{C s}$ cannot be mapped or rotated on S_y due to the line $\overline{C s}$ and the surface S_y are not aligned anymore. It can be analogous by Fig. 5-5d. The inclined curved surface (S_i) is obtained by sliced the workpiece material using plane B. Plane B is a plane A that is rotated by θ_B . The radius of S_i (R_i) is dependent on S_x . When S_x is a curved surface, the equations were derived by referring back to Fig. 5-5a. Line $\overline{q v}$ denotes the projected distance in the z -axis from a projected point q on the workpiece surface to the baseline of curved surface S_y .

$$\overline{q v} = R_y \cos \delta_y \quad (5-22)$$

$$\overline{st} = ((\overline{qv} - \overline{Cq}) / \cos \theta_x) + \overline{Cs}; \quad \text{for convex surface} \quad (5-23)$$

$$\overline{st} = ((\overline{qv} + \overline{Cq}) / \cos \theta_x) - \overline{Cs}; \quad \text{for concave surface} \quad (5-24)$$

$$R_i = \left((\overline{st})^2 + (R_y \sin \delta_y)^2 \right)^{0.5} \quad (5-25)$$

On the other hand, when S_x is a slope or flat surface, then it is calculated as follows,

$$R_i = (R_y \sin(90 + \gamma)) / \sin(90 - \gamma - \theta_B); \quad \text{for slope surface} \quad (5-26)$$

$$R_i = R_y / \cos \theta_B; \quad \text{for flat surface} \quad (5-27)$$

R_i is calculated only when it meets three conditions: θ_B , R_y , and θ_A are not equal to zero. Otherwise, $R_i = R_y$.

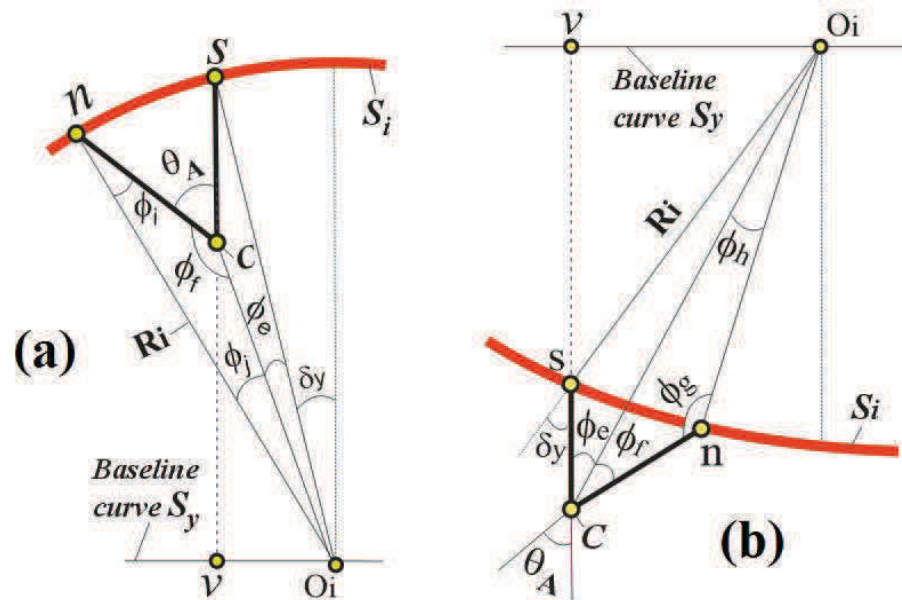


Fig. 5-6 Rotation of rotated projection line on S_i , a) convex surface,
b) concave surface

5.2.2.3. STEP 3: Rotating the Rotated Line by θ_A

In the Step 3, the rotated projection line (\overline{Cs}) from step 1 is rotated again about point C by θ_A . This rotation is aimed to obtain line \overline{Cn} on S_i . Line \overline{Cn} represents the length of contact between the tool and the workpiece, or normally called as the length of cut. This step is performed only when θ_A is not equal to

zero, otherwise, $\overline{Cn} = \overline{Cs}$. For a convex surface, the equations to calculate \overline{Cn} were derived by referring to Fig. 5-6a.

$$\overline{CO}_i = (\overline{Cs}^2 + R_i^2 - 2\overline{Cs}R_i \cos\delta_y)^{0.5} \quad (5-28)$$

$$\phi_e = \cos^{-1}((\overline{CO}_i^2 + R_i^2 - \overline{Cs}^2)/(2\overline{CO}_iR_i)) \quad (5-29)$$

$$\phi_f = 180 - |\theta_y| - |\delta_y| + \phi_e \quad (5-30)$$

$$\phi_g = \sin(\overline{CO}_i \sin\phi_f/R_i); \quad (5-31)$$

$$\phi_h = 180 - (\phi_f + \phi_g) \quad (5-32)$$

$$\overline{Cn} = (R_i^2 + \overline{CO}_i^2 - 2R_i\overline{CO}_i \cos\phi_h)^{0.5} \quad (5-33)$$

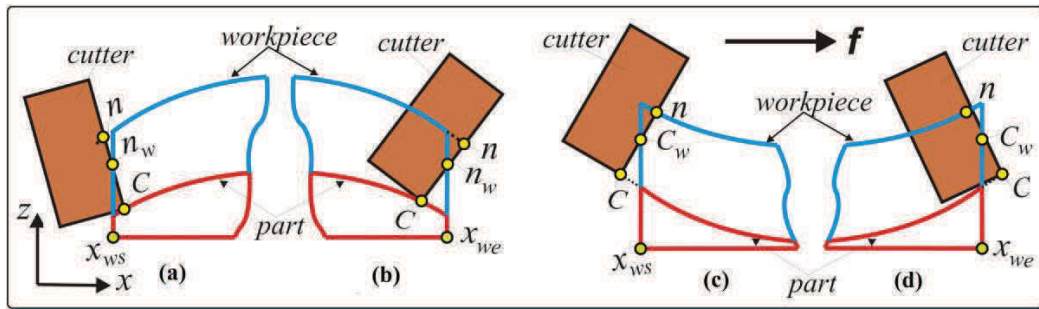


Fig. 5-7 Engagement points on the wall of workpiece surface

For a concave surface, the method was derived by referring to Fig. 5-6b and the results are presented as follows.

$$\overline{CO}_i = (\overline{Cq}^2 + R_i^2 - 2\overline{Cq}R_i \cos\delta_y)^{0.5} \quad (5-34)$$

$$\phi_e = \sin^{-1}(R_i^2 \sin(180 - \delta_y)/\overline{CO}_i) \quad (5-35)$$

$$\phi_f = |\theta_A - \phi_e| \quad (5-36)$$

$$\phi_g = 180 - \sin^{-1}(\overline{CO}_i \sin\phi_f/R_i) \quad (5-37)$$

$$\phi_h = 180 - (\phi_f + \phi_g) \quad (5-38)$$

$$\overline{Cn} = \overline{CO}_i \sin(\phi_h)/\sin\phi_g \quad (5-39)$$

For a slope and a flat surface are determined using Eq.(5-40) and Eq.(5-41), respectively.

$$\overline{C n} = (\overline{C s} \sin(90 + \gamma)) / \sin(90 - \gamma - \theta_A) \quad (5-40)$$

$$\overline{C n} = \overline{C s} / \cos \theta_A \quad (5-41)$$

Finally, the coordinate of n_f is determined by mapping the parametric equation of a cylindrical surface in Eq.(4-23) or Eq.(4-24) with l_n is equal to $\overline{C n}$.

For a case when the tool is located near by the limit of the workpiece dimension, or in the other word when the tool is located at start or end of tool path as illustrated in Fig. 5-7, the UE-point and the LE-point may be located on the wall of workpiece surface, which are denoted by n_w and C_w , respectively. In these cases, the UE-point and LE-point, which are obtained in the previous section, should be checked to determine the actual location. For this case, the *cylindrical-boundary* method as discussed in Chapter 4 is used to define the UE-point. Then a new l_n is obtained.

5.2.3. Application and Discussion

The formulae derived in this section were used to developed ABS using MATLAB. Three free-form workpiece and part surface models as shown in Fig. 5-8 were tested. A two teeth flat-end cutter with a diameter 20 mm was employed for Test 1 and Test 2. Meanwhile for Test 3 was used a flat-end cutter with 12 mm in diameter. The tool was set incline with an inclination angle 10° for Test 1 and Test 3, and 15° for Test 2. Using ABS, the shape of cut were generated and the results for several CC-points are presented in the right side of Fig. 5-8. All of the tests produced the shapes of cut that is similar to the shape of the workpiece removed. This was an indication that the proposed method was accurate. The lengths of cut for one tool pass for every test with machining conditions 5000 rpm and 0.3 mm/tooth are presented in Fig. 5-9.

The shapes and the length of cut as a function of the engagement angle for several CC-points are presented in Fig. 5-10. The length of cuts, which were produced by Test 1, forms a symmetrical shape as presented in Fig. 5-10a. For CC-40, mostly the UE-points are located on the wall surface at the workpiece end limit. It makes the length of cut in the middle of tool rotation drop drastically.

Differ to Test 1, the length of cut for Test 2 and Test 3 are asymmetrical. This is because the shape of the workpiece and part surfaces were more complex.

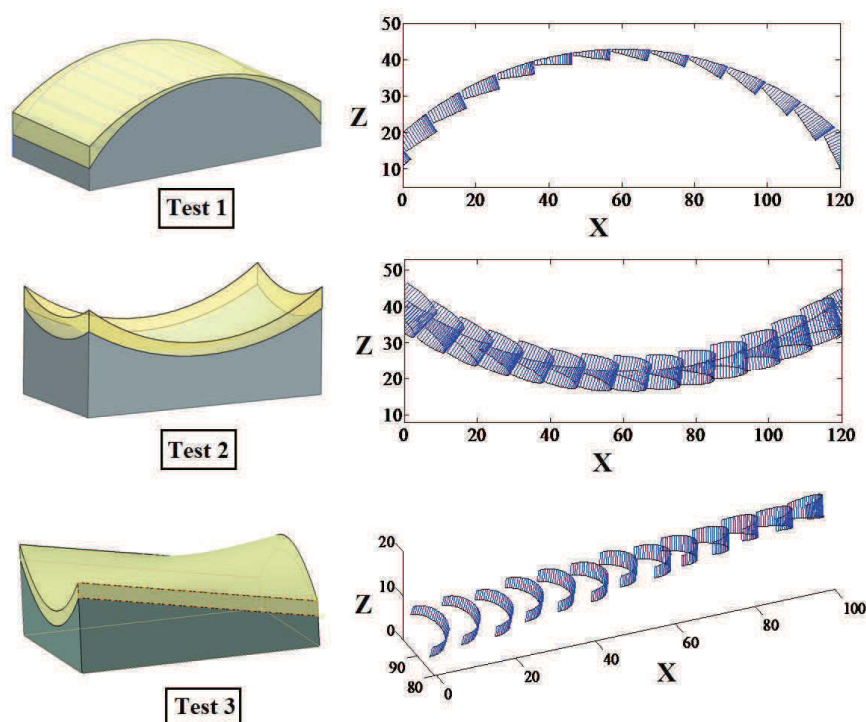


Fig. 5-8 Part and workpiece design for test, and the shape of cut generated by program simulation

Compared to test 1 and test 2, The shape of the workpiece surface for Test 3 was more complex (higher curvature). To reduce the error due to the complexity of the workpiece surface in Test 3, the instantaneous workpiece surface at instantaneous tool location was divided into two: first, the surface at the engagement angle $0 < \varphi \leq 90$ and the second for $90 < \varphi \leq 180$. Hence, the workpiece surface was discretized by more number of normal vectors. For the case when the UE-points located on the wall of workpiece start limit are shown by Test 2 at CC-1. Due to the initial LE-point is out of the workpiece, then the length of cut at the start and end of tool rotation decrease. Meanwhile for the case when both the UE-point and the LE-point located out of the workpiece is presented by Test 2 at CC-1 when $\varphi = 180$. In this graph can be seen that the length of cut is equal to zero.

Even though the shape of cut was similar to the shape of material removed, but the accuracy of the proposed method was kept verified. The

verification was performed by comparing the length of cut obtained from the simulation program to the one measured using commercial CAD software, Siemens-NX. Actually, Siemens-NX has no function to generate the instantaneous CWE data. Therefore, the CWE measurements were performed manually. Verification method performed in this method is similar to that was applied for the second verification in semi-finish milling. As shown by Fig. 5-11a, the length of cuts were measured by extracting the intersection between a tool model and a workpiece model. The tool model was placed at the instantaneous CC-point and then its orientation was adjusted. After that, the intersection between the workpiece model and the tool model can be extracted. Then the length of cut for every engagement angle were measured from the extracted model. Although the CWE can be measured using Siemens-NX, but it is very time consuming because it is performed manually.

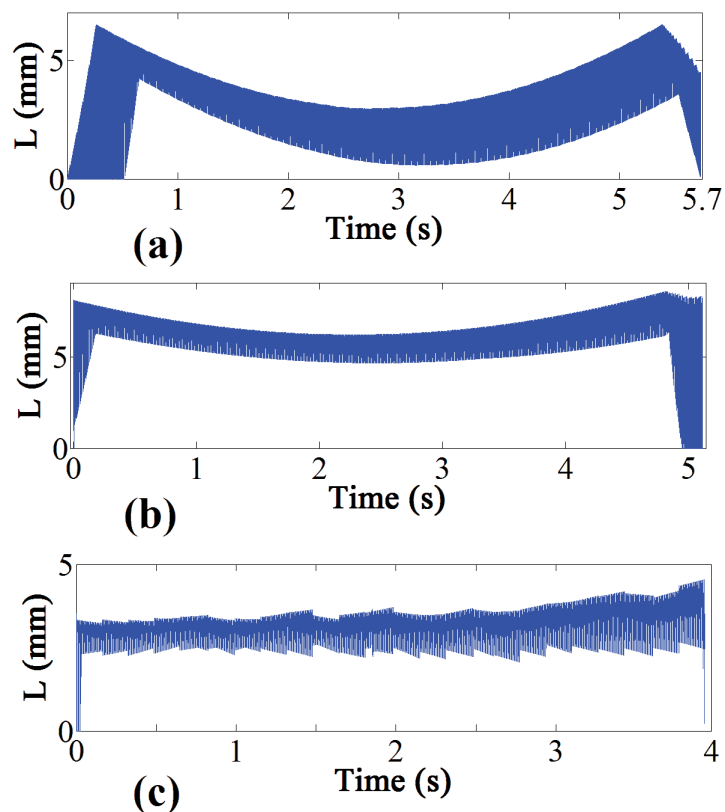


Fig. 5-9 The length of cut progression for every test model

An error of the developed model is a difference between the length of cut generated using the program simulation and the one measured using Siemens-NX.

The verification results are presented in Fig. 5-11b,c,d. From the graphs in this figure can be seen that the proposed model produced small error. The errors of Test 1 for both CC-points (CC-10 and CC-40) are less than 0.13%. Test 2 shows higher error compared with Test 1 and Test 2, especially for CC-1 when the tool enter to and exit from the workpiece. Actually, this test produced small difference between the length of cut from simulation and the one from measurement. However, because the length of cuts are also small (see Fig. 5-11b for the length of cut at CC-1), then it made the percentage of the errors higher. For test 2, the errors are less than 3.4%. Small errors are also presented by Test 3. The maximum error is 0.38%.

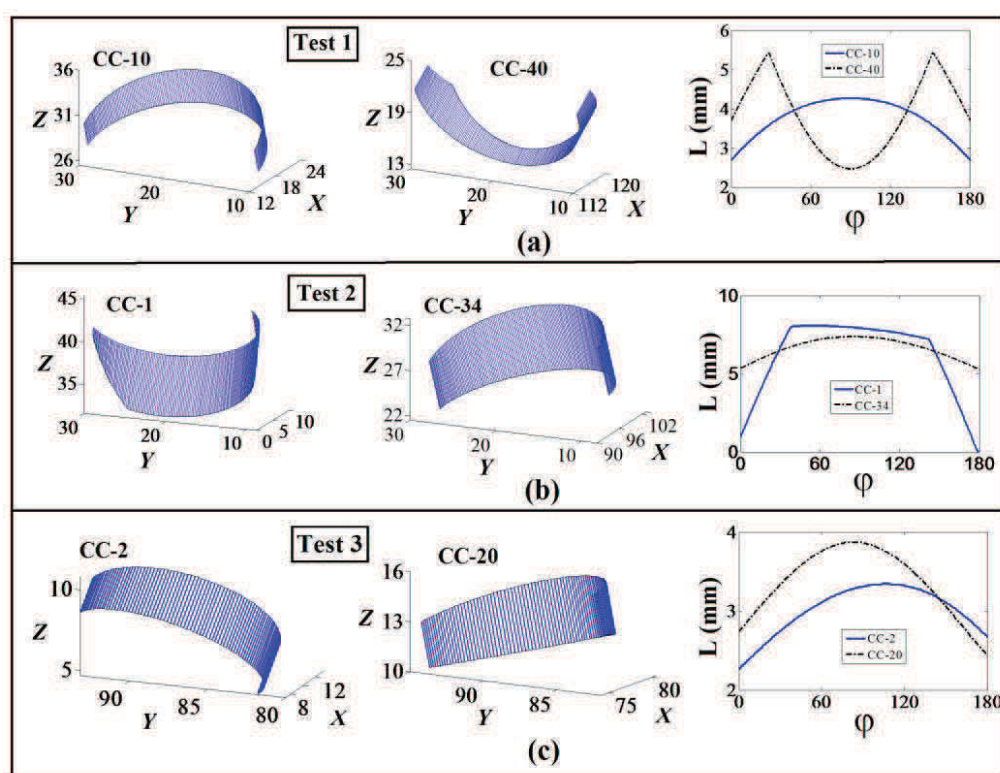


Fig. 5-10 The shape of cut and the length of cut at $\varphi \in \{0, 180\}$ for selected CC-point

Even though the shape of workpiece surface in Test 3 was more complex than both Test 1 and Test 2, but it produced smaller errors. This is because the calculation was performed by dividing the instantaneous workpiece surface into two regions, hence it reduced the error. However, it caused the calculation time higher because more surface regions should be calculated.

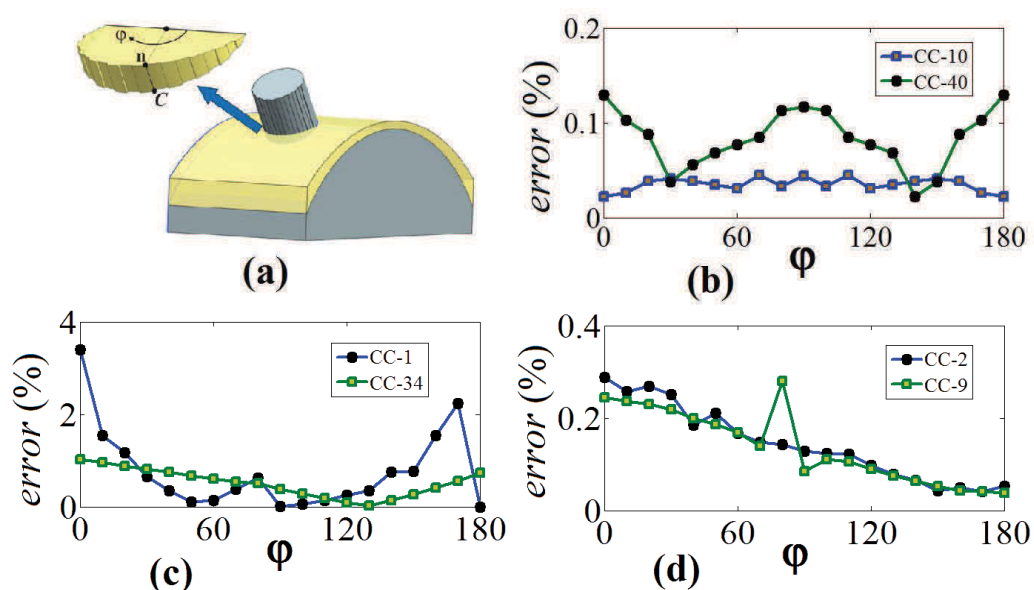


Fig. 5-11 Model verification, a) method to measure CWE in CAD software, b,c,d) error for $\phi \in [0 : 10 : 180]$

The tests revealed that the proposed method could be used to determine the CWE of a free-form surface. The accuracy of this method was largely influenced by the accuracy in predicting the surface shape at every tool location. If the calculation was performed using one surface region for a one complete tool revolution, hence, the error may increase when the workpiece has higher curvature. High-curvature means that the surface is very dynamic that has more than one surface shape in one tool revolution. In this case, however, the error can be decreased by dividing the instantaneous workpiece surface into several regions. By this strategy, the workpiece surface must be discretized with more number of normal vector. Obviously, the calculation time will also longer.

5.2.4. Comparison of Finish Model with Z-Mapping

To ensure the advantage of the proposed method over the discretization method, the comparison test in term of computational time was also performed. The part and workpiece model as used in Test 1 was used in the comparison test. The simulation was performed using a cutting speed 5000 rpm and a feedrate 0.3 mm/tooth. For the Z-mapping method, the workpiece surface was discretized with a grid size 0.1 mm both in the x -axis and the y -axis. Meanwhile for the ABS, the

workpiece surface was discretized with a grid size 0.3 mm in the x -axis and 20 mm in the y -axis.

Both the ABS and the Z-mapping method were performed using Matlab on Intel Core i5 1.7 GHz laptop with 6 GB RAM. The uninterrupted test from CC-1 to CC-40 was carried out and the computational time in between two consecutive CC-point was recorded. This measurement was repeated three times for every method and the average results are presented in Fig. 5-12. From this graph can be seen that the computational time for the proposed method (ABS) is much shorter than the Z-mapping method. The ABS took only 334.68 second to generate the length of cut as presented in Fig. 5-12, meanwhile the Z-mapping took 3,579.82 second. The Z-mapping is not a fast algorithm because it must calculate a large number of surface data. Meanwhile the ABS is more efficient because the workpiece surface is defined mathematically, and the CWE is calculated directly using a combination of parametric equation of the cutting tool, tool orientation data and mathematic equation of the workpiece surface, which was discussed in the previous sections. The computational time is the main advantage of analytical method over the discrete method.

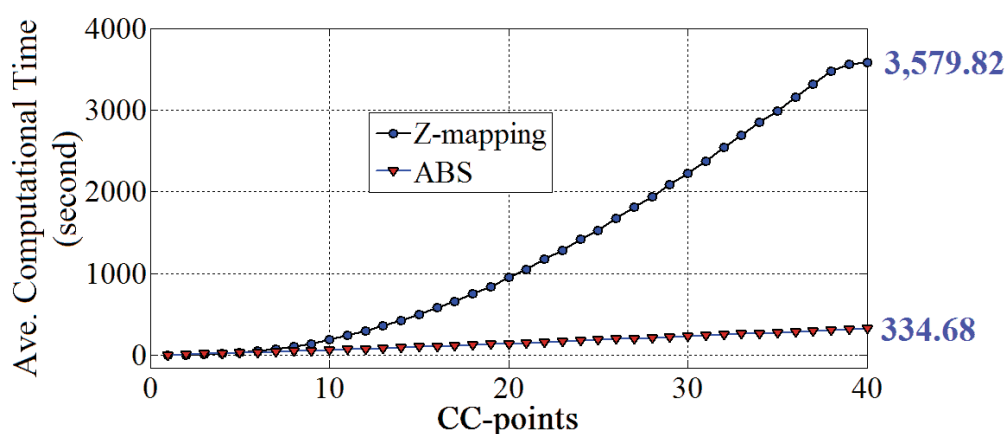


Fig. 5-12 Comparison of average computational time between ABS and Z-mapping

5.3. Obtaining the UE-Point of a Free-form Surface Machining using a Toroidal Cutter

The procedure to define the CWE points using a toroidal tool is more complicated compared with a flat-end cutting tool. Because of its geometric, the UE-point can be located either on the toroidal side or cylindrical side. Therefore, two projection lines, as shown in Fig. 5-13, should be identified. Hence, the coordinate of $w_C(x_{w_C}, y_{w_C}, z_{w_C})$, which is a point on the workpiece surface that is projected from point $C(x_C, y_C, z_C)$, and $w_P(x_{w_P}, y_{w_P}, z_{w_P})$, which is a point on the workpiece surface that is projected from point $P(x_P, y_P, z_P)$, should be determined. Point C and point P are the points on the cutting tool that are located at the lowermost toroidal side and uppermost toroidal side, respectively. The projection lines, $\overline{Cw_C}$ and $\overline{Pw_P}$, are employed as the initial reference line for further calculation. The engagement point are obtained by rotating the projection line using the tool orientation angles. Fig. 5-14 summarizes the procedure to obtain the UE-point and the detail steps will be elaborated in the following sections. When the UE-point is predicted on the cylindrical side, then, the method to calculate the UE-point for a flat end cutter in Fig. 5-2 is utilized.

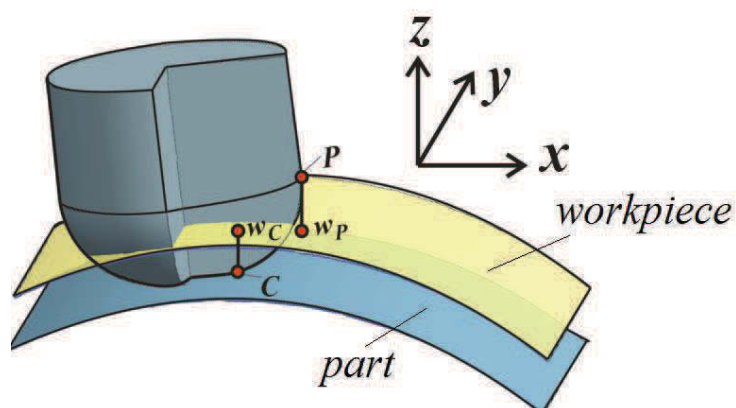


Fig. 5-13 Projection line of toroidal cutter

5.3.1. Checking the Feasible Engagement Location

Because the generic equations for the toroidal side and cylindrical side of the cutting tool are different, then the method to calculate the UE-point on the toroidal side is different to that on the cylindrical side. Location of the UE-point either it is

on toroidal side, cylindrical side, or no engagement between cutter and workpiece, should be determined in beginning. This checking step is performed by calculating the value of D_C , which is equal to $z_{w_C} - z_C$, and D_P , which is equal to $z_{w_P} - z_P$, as depicted in Fig. 5-13.

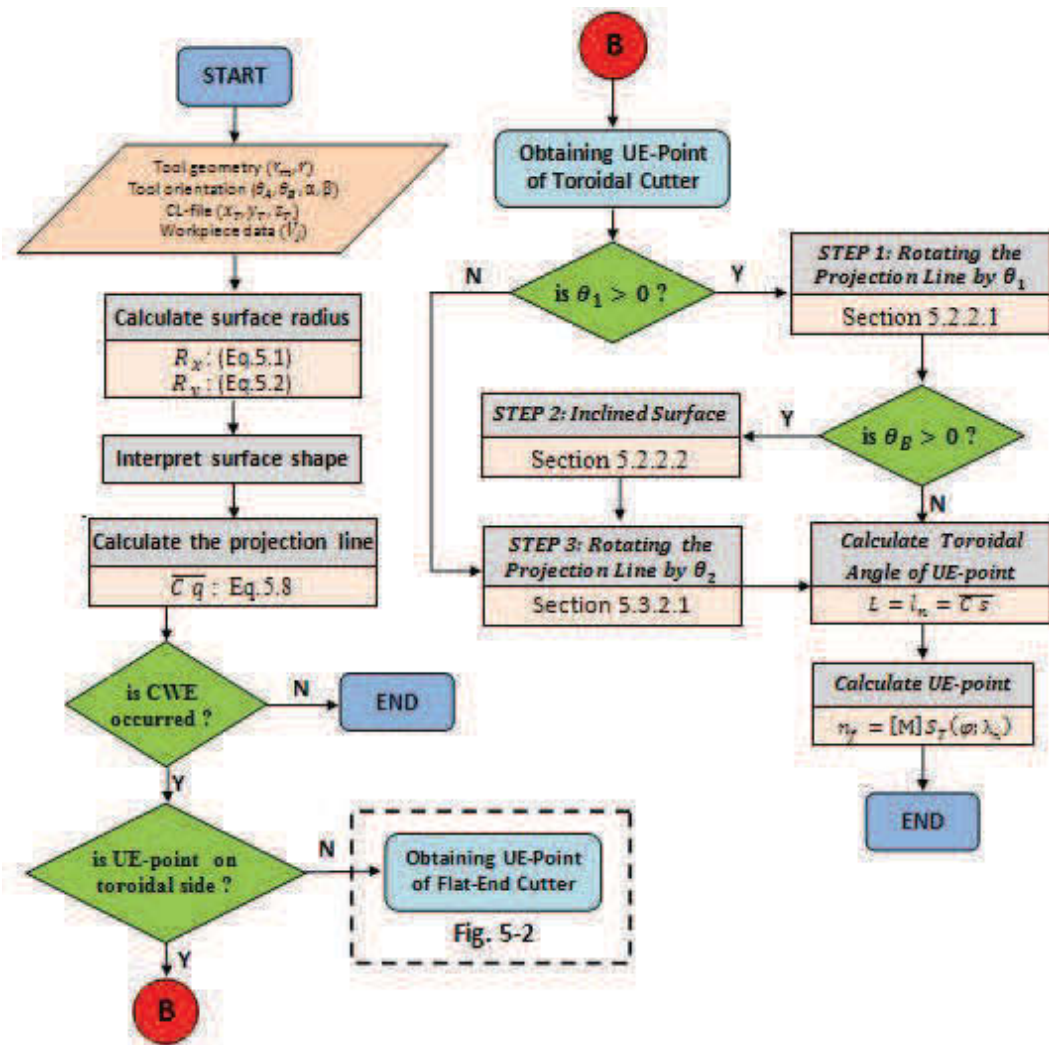


Fig. 5-14 Flow chart to obtain the UE-point for toroidal cutter

Before defining D_C and D_P , the coordinate of $w_C(x_{w_C}, y_{w_C}, z_{w_C})$ and $w_P(x_{w_P}, y_{w_P}, z_{w_P})$ should be determined. Because w_C and w_P are the points that are projected from point $C(x_C, y_C, z_C)$ and point $P(x_P, y_P, z_P)$, respectively, then $\{x_{w_C}, y_{w_C}, x_{w_P}, y_{w_P}\}$ are equal to $\{x_C, y_C, x_P, y_P\}$. While z_{w_C} is obtained by calculating the z -axis on S_x with respect to x_C , and the z -axis on S_y with respect to

y_C . First, by working on S_x , the z -value can be calculated by comparing x_C with the coordinate and orientation of the reference vector v_1 .

Using the same procedure in calculating D_C , then x_P and y_P are employed to calculate D_P . After D_C and D_P are determined, the location of UE-point can be defined by following the rules below.

1. If $D_C > 0$ and $D_P \leq 0$: the UE-point is located on the toroidal side, and then $\overline{C w_C}$ becomes the projection line.
2. If $D_C > 0$ and $D_P > 0$: the UE-point is located on the cylindrical side, and then $\overline{P w_P}$ becomes the projection line.
3. If $D_C < 0$ and $D_P < 0$: there is no engagement between cutter and workpiece.

The projection line is a line that will be used as the initial reference line to calculate the length of cut and to define the coordinate of the CWE.

Table 5-1 Variables used for selected engagement angle

Variables	$\varphi \{0\}$	$\varphi \{90\}$	$\varphi \{180\}$
R_1	R_x	R_y	R_x
R_2	R_y	R_x	R_y
ε_1	ε_{x1}	ε_{y1}	ε_{x1}
ε_2	ε_{y1}	ε_{x1}	ε_{y1}
δ_1	δ_x	δ_y	δ_x
δ_2	δ_y	δ_x	δ_y
θ_1	$\theta_B/\theta_{B\chi}$	$\theta_A/\theta_{A\chi}$	$\theta_B/\theta_{B\chi}$
θ_2	$\theta_A/\theta_{A\chi}$	$\theta_B/\theta_{B\chi}$	$-\theta_A/\theta_{A\chi}$
S_1	S_x	S_y	S_x
S_2	S_y	S_x	S_y

5.3.2. Obtaining the UE-Point

The calculation is initially performed by determining the CWE at $\varphi \{0, 90, 180\}$. The cut geometry at others engagement angle will be interpolated based on the cut geometry from these three engagement angles. Thus, for generalizing the calculation, several variables for every engagement angle should be defined. The variables and their values can be seen in Table 5-1.

After the projection line is obtained, then it is rotated using the tool orientation angles, θ_1 and θ_2 (Table 5-1). These two rotation processes are part of the three procedures that will be performed to calculate the UE-point. The UE-point on the cylindrical side is obtained by performing only two rotation procedures. In this case, all of the procedures to obtain the UE-point for a flat end cutting tool, which has been discussed in the previous section, can be applied to calculate l_n . Then the coordinate of UE-point, n_f , is calculated using Eq.(4-23) or Eq. (4-24) with $l = l_n + r$.

A different method was developed for the UE-point on the toroidal side. When it is located on the toroidal side, the method to obtain the UE-point consist of three procedures. Two of three procedures are the rotation of the projection line using θ_1 and θ_2 . The final intersection between a tool and a workpiece will be obtained in the third procedure. In the third procedure, the toroidal side of toroidal cutting tool is represented by a circle. All of the procedures must be performed sequentially, except for certain conditions it can be skipped and then jump to the next procedure. For the first procedure, the method to rotate the projection line for a flat-end mill, which was derived in section 5.2.2.1, and the method to obtain the inclined surface in section 5.2.2.2 are utilized. For the second procedure, even though the procedure is similar to the method used for a cylindrical surface, but the objective is different. The detail procedure to obtain n_f will be derived and discussed in the following sections.

5.3.2.1. Rotating the Rotated Line by θ_2

In this procedure, the rotated line, which is obtained from the first rotation by θ_1 , is rotated again by θ_2 . Even though the final coordinate of the UE-point will be obtained in the third procedure. But if S_2 is a curved surface, then, ϕ_g and the length of line $\overline{O_3O_4}$, as depicted in Fig. 5-15, need to be defined in the second procedure. Otherwise, the calculation jumps to the next procedure. ϕ_g and $\overline{O_3O_4}$ are employed as the input for the CWE calculation in the third procedure. Point O_4 is the center point of the toroidal side of the cutting tool and it can be located either inside or outside of the workpiece surface. The length of $\overline{bO_4}$ is equal to the

5.3.2.2. Calculate Toroidal Angle of the UE-Point

For the CWE that is only occurred on the toroidal side, n_f is determined by mapping the parametric equation of a toroidal surface (Eq.(4-28) or (4-29)). Before the mapping operation is executed, the toroidal angle of the engagement point need to be determined. The methods to calculate a toroidal angle for all of the surface shapes are elaborated below. In this stage, the toroidal cutter will be represented as a circle with radius r .

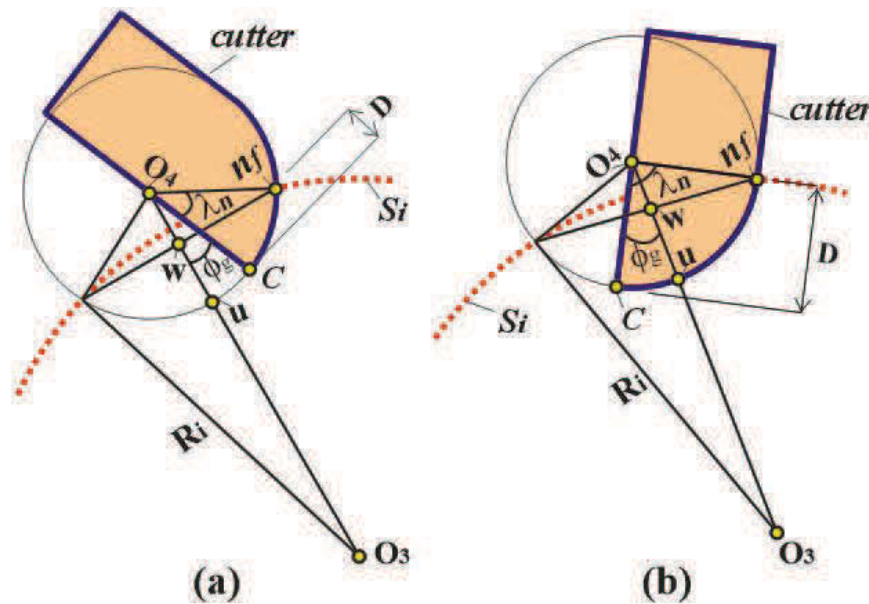


Fig. 5-16 The intersection point between the toroidal side of a cutting tool and a curved workpiece surface, a) θ_2 positive, b) θ_2 negative

1. Curved Surface

n_f is obtained using two circles intersection methodology as shown in Fig. 5-16. In this case, the toroidal side of the cutting tool and the workpiece surface are considered as a circle with radius r and R_i , respectively. ϕ_g , which was obtained in the second procedure, is used to define the orientation of the cutting tool. Then the line \overline{wu} is calculated as,

$$\overline{wu} = (r - r^2 - R_i^2 + \overline{O_3O_4}^2) / (2 \overline{O_3O_4}) \quad (5-48)$$

It is possible that the tool is rotated in positive (Fig. 5-16a) or negative (Fig. 5-16b) direction. For example, when the tool orientation at $\varphi\{0\}$ is positive, then it is negative at $\varphi\{180\}$, and vice versa. Accordingly, θ_2 for $\varphi\{180\}$ as

shown in Table 5-1 was set to be negative. The toroidal angle is expressed generally by,

$$\lambda_n = \cos^{-1}\left(1 - \left(\frac{\overline{wu}}{r}\right)\right) + \phi_g \quad (5-49)$$

ϕ_g is positive when θ_2 is negative and negative when θ_2 is positive .

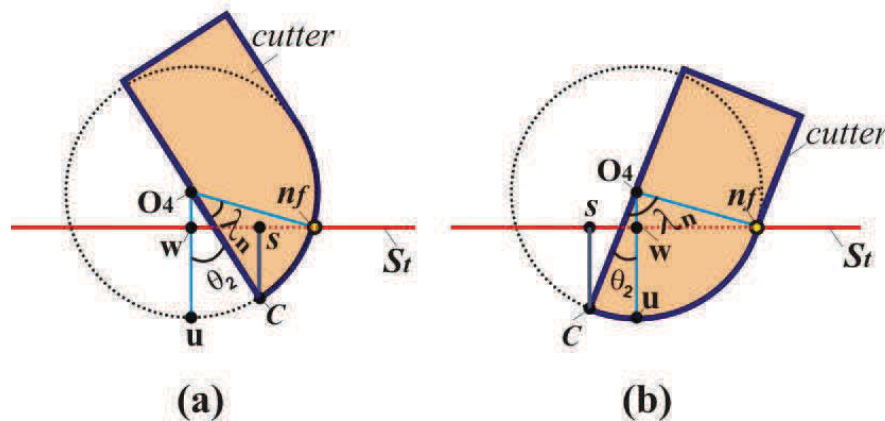


Fig. 5-17 The intersection point between the toroidal side of a cutting tool and a slope workpiece surface, a) when θ_2 is positive, b) when θ_2 is negative

2. Flat surface

When S_2 is a flat surface, then the two circle intersection method is not applicable because the workpiece surface cannot be represented as a circle. Then the line \overline{wu} and the toroidal angle are calculated by referring to Fig. 5-17.

$$\overline{wu} = (r - r \cos \theta_2) + \overline{Cs} \quad (5-50)$$

$$\lambda_n = \cos^{-1}\left(1 - \left(\frac{\overline{wu}}{r}\right)\right) + \theta_2 \quad (5-51)$$

3. Slope surface

The line \overline{wu} and the toroidal angle for a slope surface, which are presented in Fig. 5-18, are determined using the following equations,

$$\overline{wu} = \overline{Cs} - r(1 + \sin \theta_2 \tan \gamma - \cos \theta_2) \quad (5-52)$$

$$\lambda_n = 90 - \gamma + \theta_2 - \sin^{-1}\left\{\frac{(r - \overline{wu}) \sin(90 - \gamma)}{r}\right\} \quad (5-53)$$

Finally, n_f is calculated using Eq.(4-28) or (4-29) with $\lambda = \lambda_n$.

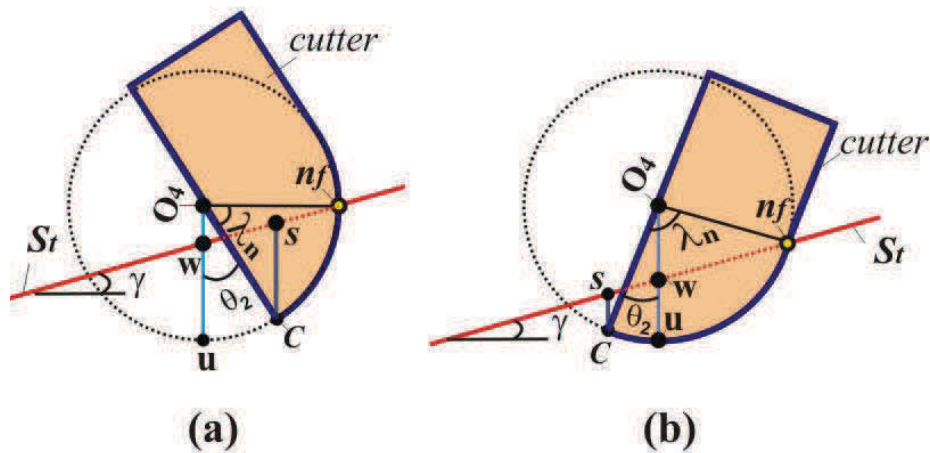


Fig. 5-18 The intersection point between the toroidal side of a cutting tool and a slope surface, a) when θ_2 positive, b) when θ_2 negative

5.3.2.3. The UE-point for Every Engagement Angles

As mentioned before that the calculation, which was discussed in the previous section, is only for obtaining the UE-point at $\varphi \{0, 90, 180\}$. The UE-points obtained in that stages are called as $n_A(\varphi = 0)$, $n_B(\varphi = 90)$ and $n_C(\varphi = 180)$. For the other engagement angles, the UE-points are determined by interpolating these three engagement angles. The coordinate of n_f as a function of the engagement angle is determined by first obtaining the z_{n_f} using an interpolating process. For reducing the error, the interpolating process is divided into two sections, the UE-point at $0 \leq \varphi < 90$ and that at $90 < \varphi < 180$.

$$\begin{aligned} z_{n_f} &= z_{n_A} + (z_{n_B} - z_{n_A}) \sin \varphi ; \text{ for } 0 \leq \varphi < 90 \\ z_{n_f} &= z_{n_C} + (z_{n_B} - z_{n_C}) \sin \varphi ; \text{ for } 90 < \varphi < 180 \end{aligned} \quad (5-54)$$

After z_{n_f} is obtained, the next step is to determine the location of the CWE whether it is on the cylindrical side or the toroidal side. The method, which was explained in section 3.5.1, is applied in this section. Then, the UE-point can be determined after its toroidal angle, which is calculated using *Z-toroidal* method, or the length of cylindrical contact that is calculated using *Z-cylindrical* method, is obtained. After the toroidal angle or the length of cylindrical contact is obtained, finally the coordinate of the UE-point can be calculated.

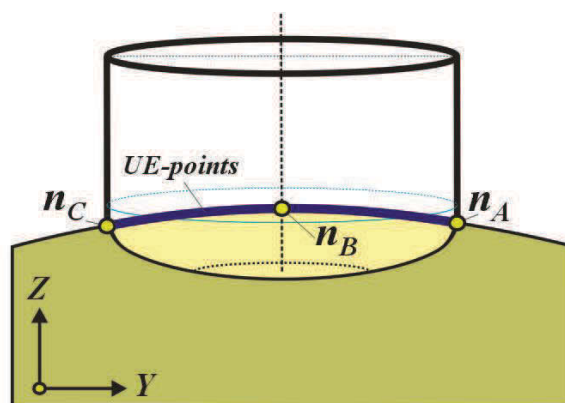


Fig. 5-19 the UE-point for $\varphi \{0, 90, 180\}$

5.3.3. Application and Discussion

Based on the formulae that were derived in the previous sections. A simulation program (ABS) using MATLAB has been developed, enabling the calculation of the CWE at the instantaneous tool location. Four models with various workpiece surfaces and part surfaces, as shown in Fig. 5-20, were tested. Machining conditions used in the test were a feedrate 0.3 mm/tooth and a cutting speed 5000 rpm. A two teeth toroidal cutter with diameter 20 mm and minor radius 5 mm was employed as cutting tool.

Using the developed simulation, the shape of cut geometry and the coordinate of the CWE can be generated. The graphs, which are showed in Fig. 5-20a,b,c,d, are the cut geometry for every CC-points. It can be seen that the shape of cut is similar to the shape of part and workpiece surface. The progressions of the length of cut for one tool pass are presented in Fig. 5-20e,f,g,h.

The first test was aimed to test the proposed method with a surface that is a combination of a curved surface and a flat surface. In this test, the normal distance between the part and workpiece surface was designed constant. From the graph shown in Fig. 5-20a can be concluded that the CWEs from test model 1 were only located on the toroidal side. Furthermore, the length of cut, as depicted in Fig. 5-20e, are constant. The decreasing value from CL-point 37 until CL-40 were occurred because some part of the cutter have been located out of the workpiece limit.

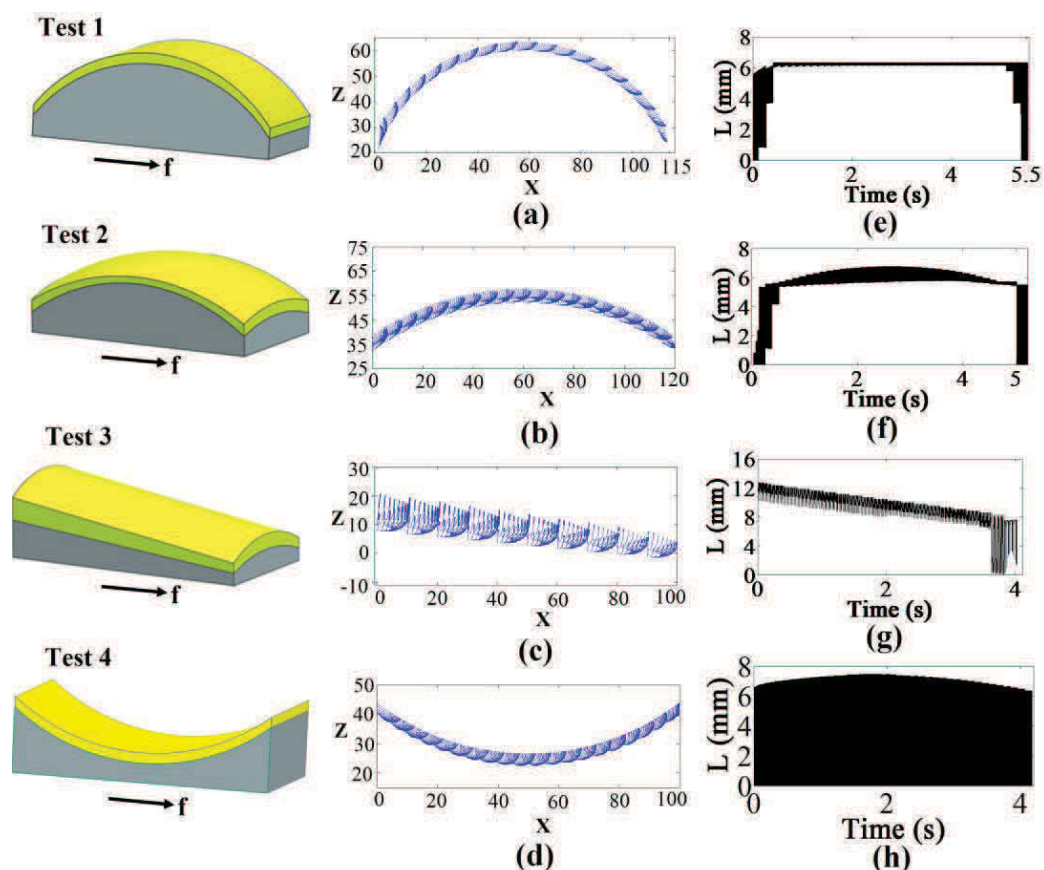


Fig. 5-20 Test models; a,b,c,d) the shape of cut, e,f,g,h) the progression of the length of cut

In the second test, a sculptured part and workpiece surface was machined. The part and workpiece surface are a combination of convex-convex surface. It is normally occurred during finish machining. Once again, the contacts were located only on the toroidal side (Fig. 5-20f) and a small variation of the length of cut was produced (Fig. 5-20). The third test was aimed to test the proposed method on a combination of a slope surface and a flat surface. The CWE were located on the cylindrical side, except for the last CC-point (Fig. 5-20g) that there was no CWE on some part the cutting tool. It was because they were located out of the workpiece limit. From Fig. 5-20h can be seen that the length of cut decrease gradually.

For the last test, a combination of a concave surface and a flat surface was machined. In this test, the tool was inclined with the inclination angle 10° . From Fig. 5-20h can be seen that there is a small variation in the length of cut. Cut

geometry progression for all of the test models, as shown in Fig. 5-20, are similar to the shape of the workpiece surface. It is an indication that the method was accurate. Nevertheless, the accuracy of the proposed method was kept examined. Therefore, to verify the accuracy of the proposed method, the length of cuts calculated using the simulation program were compared with the ones measured using the commercial software Siemens-NX. The verification method for a flat cutting tool, as explained in section 5.2.3, was also employed.

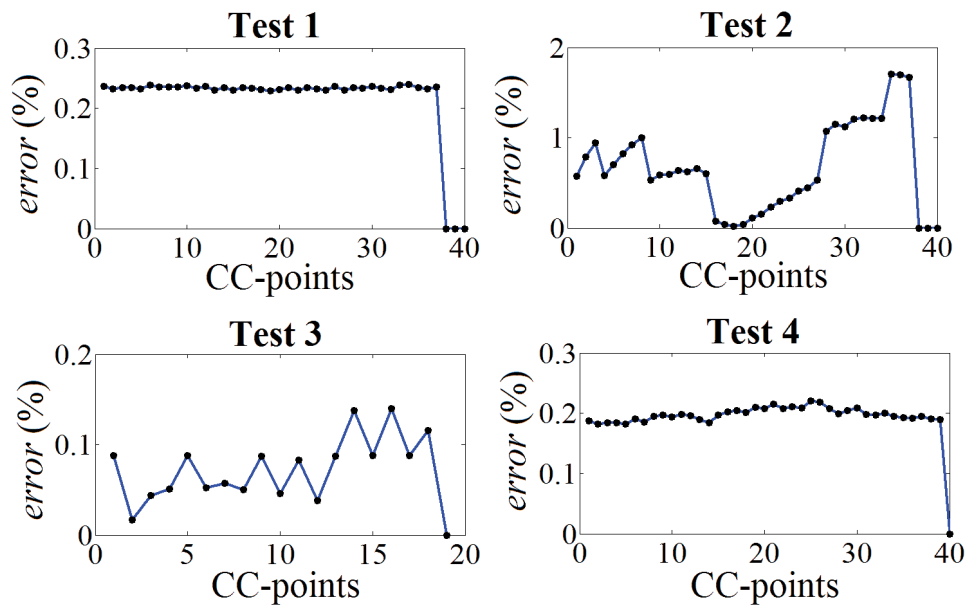


Fig. 5-21 Error at every CC-point

From the results showed in Fig. 5-21 can be seen that all of the test models produced relatively small errors. Test model 1 produced relatively constant the length of cut, and the errors were also constant about 0.23%. For Test 2, the errors were less than 1.7%. Meanwhile for the Test 3 they were below 0.14%. The last test produced error maximum 0.21%. The results indicated that there was a good agreement between the cut geometry obtained from the measurement and the one obtained from the simulation program.

The shapes of the CWE as a function of the engagement angles are presented in Fig. 5-22. For the Test 1 at CC-10 and the Test 2 at CC-10, all of the UE points were located on the toroidal side. Meanwhile for the Test 3 at CC-6, they were located on the cylindrical side. For the Test 4 at CC-30, the UE-points were also located on the toroidal side. Because the tool was set with the

inclination angle, then the length of cuts as a function of engagement angle were very fluctuate.

Verifications were also performed to check the accuracy of the method in predicting the cut geometry with respect to the engagement angle. The results are depicted in Fig. 5-22e,f,g,h. From these graphs can be seen that the errors produced by all of the tests were small. Therefore it can be concluded that the proposed method was accurate.

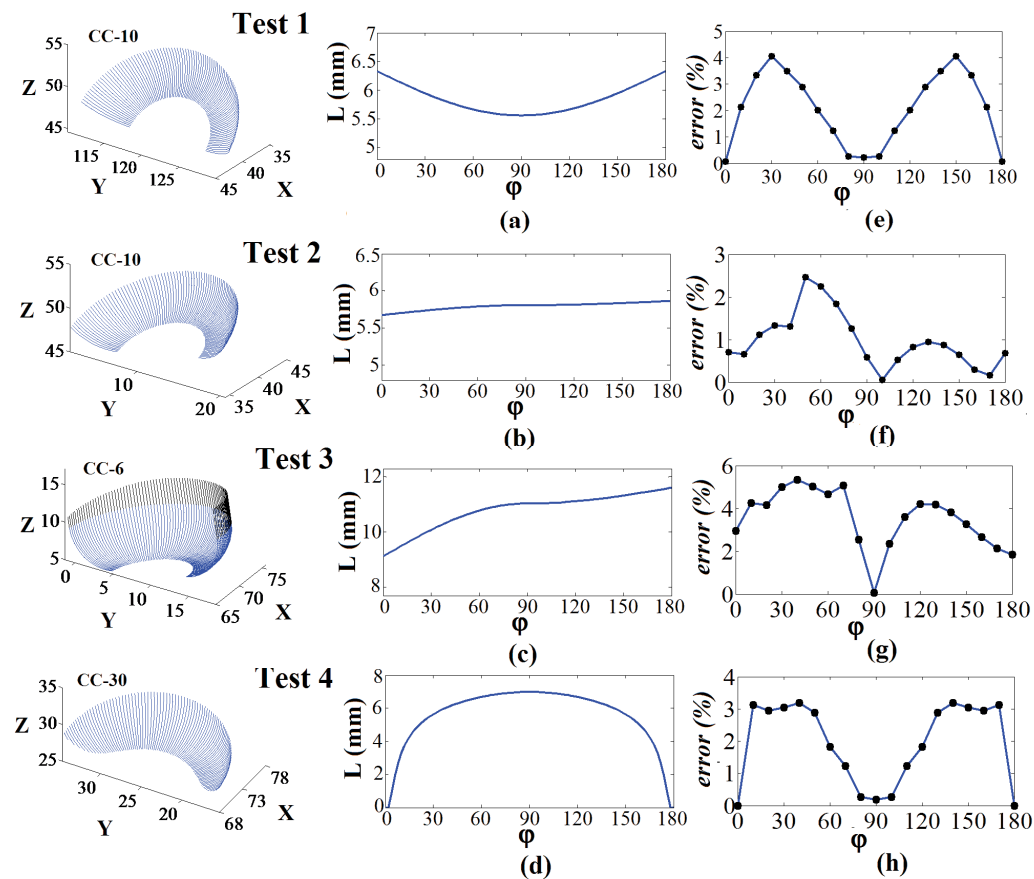


Fig. 5-22 The shape of cut geometry, the length of cut and the error for $\phi \in \{0, 180\}$ at selected CC-points

The accuracy of the proposed model was also verified by comparing the cut geometry obtained from ABS with the one obtained from the experimental work. For this purpose, a machining has been performed using five axis milling (Hurco VMX 30U - belongs to Universitas Negeri Jakarta, Indonesia). The selected machining conditions were feedrate 0.2 mm/tooth and cutting speed 1000 rpm. A two teeth toroidal cutter with major radius 6 mm and minor radius 2 mm

was used as the cutting tool. The shape of cut obtained from the experimental work is presented in Fig. 5-23a. This figure was captured using Nikon D5100. For the comparison purpose, thirty six data of the length of cut were measured, which was performed as shown in Fig. 5-23b, and the results are presented in Fig. 5-23c. This data was obtained using CorelDraw X3 by following the method as explained in section 4.4.2.4. From Fig. 5-23c can be seen that there was also a good agreement between the length of cut calculated using ABS and the one measured from the experimental work. In general, the errors were less than 7 %.

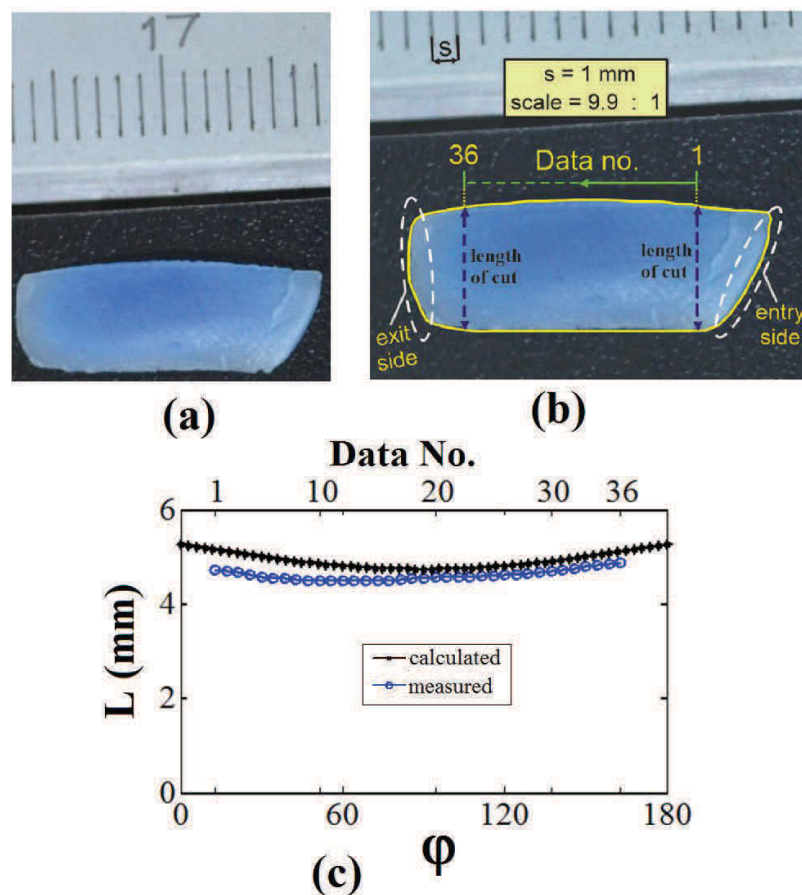


Fig. 5-23 Actual cutting verification, a) chip from machining, b) chip measured using Corel Draw X3, c) comparison of calculated and measured the length of cut

5.4. Conclusion

In this chapter, The methods to define the Cutter Workpiece Engagement for a free form workpiece surface, which are normally performed during finish milling,

was presented. The engagement was calculated using a combination of discretization and analytical method. Despite the workpiece was discretized by normal vectors, but there was no calculation to check the intersection between the cutting tool and the normal vectors. They were only used as the reference to define the shape of the surface at every CL-point, mathematically. The engagement point was obtained based on the predicted surface shape and tool orientation angles at the instantaneous tool location. The formulae were derived and implemented in a computer simulation. The program simulation, the *Analytical Boundary Simulation* (ABS), can generate the instantaneous shape of cut and the length of cut. The accuracy of the proposed methods were tested using Siemens NX. The verification was performed using the same procedure that was applied in semi-finish milling. The results showed that the proposed model produces relatively small errors. For both cutting tools, it was found that the errors are less than 4%. It proved the accuracy of the method. Moreover, the method was eliminating the need for large number of Z-mapping to define the workpiece surface. A test on the computational time proved that the proposed method is more efficient compared with Z-mapping method.

The accuracy of the proposed model was largely influenced by the accuracy in predicting the shape of the workpiece surface. Increasing the complexity of the workpiece surface will increase the error. For a complex surfaces, the error can be reduced by dividing the instantaneous workpiece surface to become several regions. Hence, the workpiece surface should be discretized into more number of normal vectors. Consequently, the calculation time will also increase.

CHAPTER 6

MODELING OF MILLING FORCE

In a CAD/CAM environment and the actual operation, practical and accurate cutting force prediction approaches are needed to optimize a process planning. Although significant works have been reported in modeling individual but simplified machining process, generalized mathematical modeling of arbitrary operations is an essential step to predict part specific operations in virtual machining. Cutting forces prediction in milling process is very importance as they are the key factors that influence the dimensional surface accuracy, machining power, and the required strength for workpiece holding mechanisms and the cutting tool. By predicting the cutting force, the tool breakage and tolerance violations before the real machining can be avoid. This Chapter presents a generalized mathematical method to predict the instantaneous cutting force. The CWE models that have been developed in the previous chapters are employed to support the cutting forces prediction model.

6.1. Cutting Force Coefficient Identification

According to the early studies [103], cutting force predictions are mainly characterized by three methods: analytical, mechanistic, and numerical methods. However, the first model is less accurate and the third is time-consuming [104]. Mechanistic model gives intermediate advantages based on the different cutting conditions and cutter types. In the milling operation, the mechanistic identification model is widely used to predict the cutting forces. By this model, the cutting forces are related to the average cut thickness and the cutting force coefficients that are calibrated experimentally for a specific workpiece material-tool geometry pair.

Another method was also proposed by Armarego et al. [105]. They used the oblique cutting model for milling force predictions that is called the *mechanics of milling* approach. Prediction of cutting force coefficients is based on the mechanics of general oblique cutting and requires knowledge of the fundamental cutting parameters, such as workpiece material, shear stress, and friction coefficient [106]. These parameters have to be calculated from the orthogonal cutting test and create an orthogonal database for a particular tool-workpiece material pair. Once the orthogonal database has been established, the specific cutting and edge coefficients can be predicted for turning, drilling, and milling operation, for specified tool geometry and cutting conditions. Orthogonal database is particularly useful for the cutting tool designer, since the coefficient can be estimated before the cutter is going to be manufactured [107]. However, despite the orthogonal to oblique transformation provides cutting force coefficients for a variety of milling cutter geometries using three orthogonal parameters (shear stress, shear angle, friction coefficient), it is not always possible to identify these parameters when the cutting tools with a complex cutting edges are used. Moreover, constructing an orthogonal cutting database is very time consuming and costly. For this case, the specific cutting force coefficients have to be identified mechanistically.

In the mechanistic identification model, the force coefficients are identified from a series of milling test. Two different mechanistic cutting force models are found in the machining literature. They are the *exponential force coefficient* model and the *linear edge force* model. In the first one, the cutting forces are proportional to the cut thickness. The effects of shearing mechanisms due to the chip generating process on the tool's rake face and the effects of rubbing and ploughing mechanisms on the flank face are lumped into one specific cutting force coefficients for each cutting force component (tangential, radial, and axial). This model was modeled by Merchant [108]. Meanwhile Koenigsberger and Sabberwal [109] reported the proportional relationship between the uncut chip thickness and the tangential milling force component. Tlustý and MacNeil [110] and Kline [26] extended this model by including a radial force component. This extended method has been widely used in the milling force analysis [7, 111]. The

experimental results show that the cutting force tend to converges to some values different than zero as the cut thickness close to zero. It makes the cutting forces coefficient from the exponential force model increase indefinitely as the cut thickness smaller. It is occurred because of the finite sharpness of the tool edge which results in the ploughing of some material under the tool nose, and the flank contact which follow it [112].

The complexity of the phenomena of physics occurred during the cutting edge ploughing on the workpiece surface led the researcher to determine the edge forces using the second mechanistic model (*linear edge force* model). In this model, the force component is separated into the shearing component at the rake face and the ploughing component at the flank face [25]. The shearing and ploughing effect are characterized separately by the respective specific cutting and edge force coefficients [106-113]. Armarego and Deshpande [114] mentioned that the separation of ploughing force from the shearing force was found to be important in obtaining a linearized model with a constant cutting coefficient. Since the coefficients are relative independent of the average cut thickness, this model is more suitable for an analytical method [106]. However, compared to exponential model, more force coefficients need to be determined. Zorev [115] proposed different ways for identifying the edge forces that are usually found by extrapolating the cutting forces to zero cut thickness. The *linear edge force* model was also used by Armarego and Epp [105] in formulating the milling forces for zero helix cutters, and by Yellowley [116] for analytical mean force and torque formulations in peripheral milling operations.

Cheng and Tsay [117] studied the relationship between the instantaneous cutting force coefficients and other cutting parameters, and analyzed the degrees of effect factors for each parameter. Gonzalo and Beristain [118] proposed an inverse method to calculate the instantaneous cutting force by taken into account the influence of a rake angle and the cut thickness to the specific force coefficients. Another method was proposed by Wan and Zhang [100]. A forward calibration based on the lumped force model for general end milling was used to calculate the coefficients cutting force. Currently, finite element method (FEM)

based on specific software that provides simulation functionalities with different helical angle has attracted the interest in machining process modeling [103].

In this study, the second mechanistic model is used in which the cutting forces are composed of the tangential, radial and axial components. The specific cutting and edge force coefficients for each force component is calculated using the experimental cutting forces data. In this model, the average cutting forces per tooth are measured and the effect of run-out on measurement can be minimized by dividing the total force per spindle revolution by the total number of teeth.

6.2. Mechanistic Modeling of Milling Forces

Cutting forces are modeled with respect to two fundamental factors, shearing effects that is taking place in the shear zone and edge effects, which are induced by plowing or ploughing at cutting edges. Six force coefficients have to be identified through experiments and mathematical analysis for a given cutter geometry and workpiece material under specific cutting conditions. Then the cutting forces are calculated using the six force coefficients, cut thickness and the length of cut. The geometry of cut or cutter workpiece engagement (cut thickness and the length of cut) are obtained using the methods that were discussed in the previous chapters.

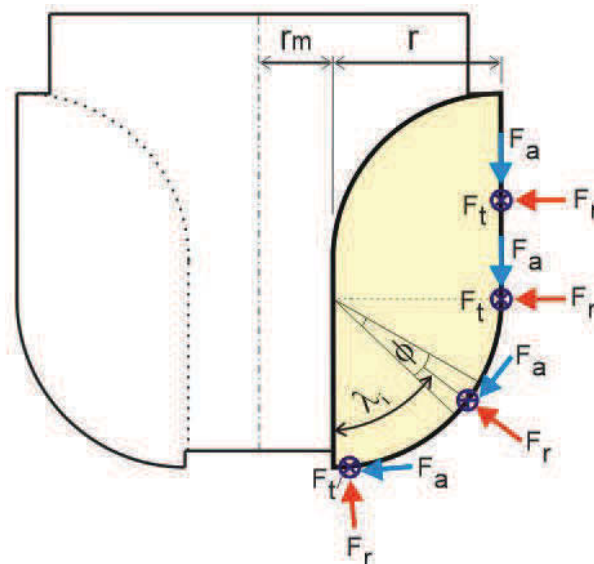


Fig. 6-1 Orientation of cutting force components on cutting edge

By following the method that was explained by Altintas [39], the tangential (F_t), radial (F_r) and axial (F_a) cutting forces acting on the infinitesimal cutting edge segment are expressed as a function of varying cut area and edge contact length as follows,

$$\begin{aligned} F_{t,i,j}(\varphi, \phi) &= K_{tc} L_{i,j} h_{i,j}(\varphi) + K_{te} L_{i,j} \\ F_{r,i,j}(\varphi, \phi) &= K_{rc} L_{i,j} h_{i,j}(\varphi) + K_{re} L_{i,j} \\ F_{a,i,j}(\varphi, \phi) &= K_{ac} L_{i,j} h_{i,j}(\varphi) + K_{ae} L_{i,j} \end{aligned} \quad (6-1)$$

where K_{tc} , K_{rc} , and K_{ac} are the cutting force coefficients contributed by the shearing action in the tangential, radial, and axial directions, respectively. Meanwhile, K_{te} , K_{re} , and K_{ae} are the edge constants. L and h are the length of cut and the cut thickness. The subscript i (1,2,3,...) and j (1,2,3,...) denote the order number of cutting edge's segment and cutting tooth, respectively. The cutting edge is segmented into small segment as illustrated in Fig. 6-1. Three components of the cutting forces are distributed along the contact length. Because the cutting tool has two surface geometries, then discretization method between the toroidal surface and the cylindrical surface are different. For toroidal surface, the surface is segmented with respect to the toroidal angle of the UE-point (λ_n) and LE-point (λ_c). Every small segment has segment angle as follows,

$$\phi_j = \frac{\lambda_{n,j} - \lambda_{c,j}}{k} \quad (6-2)$$

where k is the number of segment. In every segment, the cutting force is located in the middle of the cutting edge segment as shown in Fig. 6-1. Then the toroidal angle of a segment ($\lambda_{i,j}$) is the angle that is measured from the bottom of cutting tool ($\lambda = 0$) to the middle point of the segment. And it is calculated by,

$$\lambda_{i,j} = \phi_j (i - 0.5) \quad (6-3)$$

The length of cut at every segment is determined by,

$$\begin{aligned} L_{i,j} &= \phi_j \pi r / 180 \quad (\text{toroidal side}) \\ L_{i,j} &= l_n / k \quad (\text{cylindrical side}) \end{aligned} \quad (6-4)$$

After tangential, radial, and axial cutting force components are obtained, the forces in the Cartesian coordinate system are derived through a coordinate

transformation from orthogonal to oblique cutting. The mapping of cutting forces with respect to $\lambda_{i,j}$, φ and χ (helical angle) is expressed as follows,

$$[M]_F = Rot(Z, \varphi) \cdot Rot(Y, \chi) \cdot Rot(x, \lambda_i) = \begin{bmatrix} A_{11} & A_{12} & A_{13} \\ A_{21} & A_{22} & A_{23} \\ A_{31} & A_{32} & A_{33} \end{bmatrix} \quad (6-5)$$

where

$$\begin{aligned} A_{11} &= \cos \varphi \cos \chi \\ A_{12} &= -\cos \varphi \sin \chi \sin \lambda_i + \sin \varphi \cos \lambda_i \\ A_{13} &= -\cos \varphi \sin \chi \cos \lambda_i + \sin \varphi \sin \lambda_i \\ A_{21} &= -\sin \varphi \cos \chi \\ A_{22} &= \sin \varphi \sin \chi \sin \lambda_i + \cos \varphi \cos \lambda_i \\ A_{23} &= \sin \varphi \sin \chi \cos \lambda_i + \cos \varphi \sin \lambda_i \\ A_{31} &= \sin \chi \\ A_{32} &= \cos \chi \sin \lambda_i \\ A_{33} &= \cos \chi \cos \lambda_i \end{aligned} \quad (6-6)$$

When the UE-point is located on the cylindrical side, λ_i is equal to $\pi/2$. Finally, the forces as a function of engagement angle for multi-teeth cutters are obtained by summing the forces acting on the individual tooth in the cut.

$$\begin{bmatrix} F_X(\varphi) \\ F_Y(\varphi) \\ F_Z(\varphi) \end{bmatrix} = \sum_{j=1}^m \sum_{i=1}^k [M]_F \times \begin{bmatrix} F_{t,i,j}(\varphi, \phi) \\ F_{r,i,j}(\varphi, \phi) \\ F_{a,i,j}(\varphi, \phi) \end{bmatrix} \quad (6-7)$$

6.3. Identification of the Specific Cutting and Edge Coefficients

Specific cutting and edge coefficient are empirical and commonly identified experimentally. Martellotti [119] explained that the components of the cutting forces could be related to the average cut thickness. Sawin [120] and Sabberwall [121] showed that the cutting coefficient varies with the cut thickness. Other studies showed that the coefficient also depend on the other machining parameters such as cutting speed [104, 122] and tool geometry [123].

In this study, the effect of the axial depth of cut to the cutting and edge coefficient are analyzed. The cutting force data are generated from a set of milling test at various feedrates and axial depth of cut. The average cutting force is obtained from the fitted experimental data using polynomial curve fitting. Fig. 6-2 showed two samples of the experimental and fitted cutting force data. From Eq.(6-8), by giving the cut geometry (the length of cut and cut thickness), only the specific cutting and edge coefficient remain unknown in the right hand side. Eq.(6-8) is obtained by converting F_s ($s = X, Y, Z$) in Eq.(6-7) by F_s in Eq.(6-1) and it is expressed as follows,

$$\begin{bmatrix} F_X \\ F_Y \\ F_Z \end{bmatrix} = \sum_{j=1}^m \sum_{i=1}^k \left(L_{i,j} h_{i,j} [M]_F \begin{bmatrix} K_{tc} \\ K_{te} \\ K_{rc} \end{bmatrix} + L_{i,j} [M]_F \begin{bmatrix} K_{re} \\ K_{ac} \\ K_{ae} \end{bmatrix} \right) \quad (6-8)$$

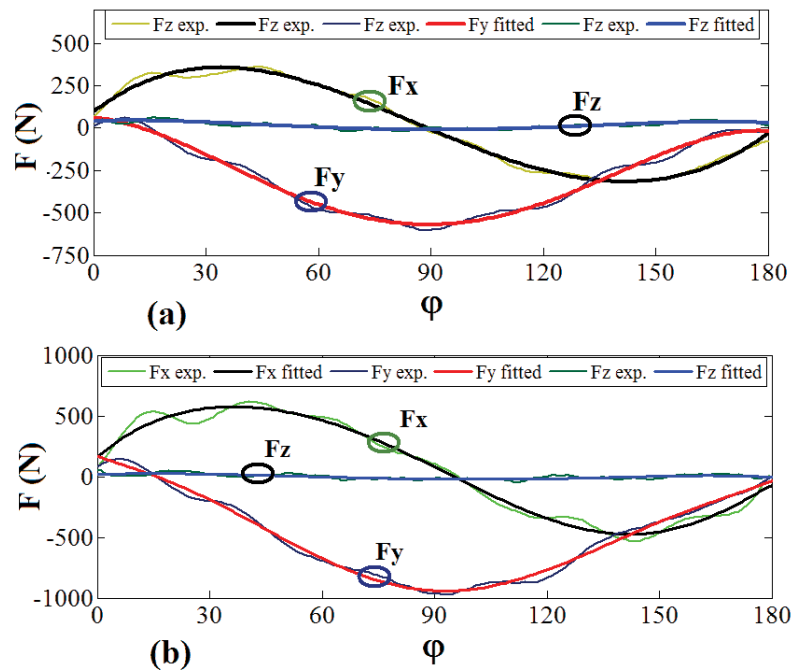


Fig. 6-2 Two samples of cutting forces data, a) feedrate 0.3 mm/tooth and axial depth of cut 2 mm, b) feedrate 0.1 and axial depth of cut 10 mm

The coefficient for each axial depth of cut is determined using the average cutting forces data at different feedrate but constant radial and axial immersions. Using the average cutting force data from two different feedrate, six cutting and edge

coefficient can be determined. The procedure to obtain the force coefficients as a function of axial depth of cut follows the procedure that was discussed in [104].

Suppose the cutting force data $\{F_{s,1}, F_{s,2}, F_{s,3}, F_{s,4}, F_{s,5}, F_{s,6}\}$ are generated from the experiment at axial depth of cut $\{D_1, D_2, D_3, D_4, D_5, D_6\}$. While F_s in Eq. (6-8) at different depth should be changed into $\bar{F}_n = \bar{F}_{s,n} - \bar{F}_{s,n-1}$, n is the current cutting depth and $n - 1$ refers to the previous depth. The force on each span is recalculated based on the forces on the current and adjacent layers. For six axial depth of cuts, the cutting forces adopted in different axial immersion are,

$$\begin{bmatrix} \bar{F}_{s,1} \\ \bar{F}_{s,2} - \bar{F}_{s,1} \\ \bar{F}_{s,3} - \bar{F}_{s,2} \\ \bar{F}_{s,4} - \bar{F}_{s,3} \\ \bar{F}_{s,5} - \bar{F}_{s,4} \\ \bar{F}_{s,6} - \bar{F}_{s,5} \end{bmatrix} = \begin{bmatrix} \bar{F}_1 \\ \bar{F}_2 \\ \bar{F}_3 \\ \bar{F}_4 \\ \bar{F}_5 \\ \bar{F}_6 \end{bmatrix} \quad (6-9)$$

The final cutting and edge coefficients as a function of axial depth of cut (D) are fitted through a polynomial fitting. The detailed expression of cubic polynomial is written by,

$$K_q = aD^3 + bD^2 + cD + d \quad (6-10)$$

where K_q ($q = tc, rc, ac, te, re, ae$) are the force coefficients and a, b, c, d are the polynomial coefficients.

6.4. Cutting Force Prediction in Five-Axis Milling

The procedure discussed in section 6.2 is applicable for calculating the cutting force in three-axis milling operation. Cutting forces measurement in five-axis milling is more challenging task due to the varying orientation of the tool axis with respect to the workpiece coordinate surface. In five-axis milling, generally the cutting forces can be measured in two ways; first one is using table-typed dynamometer that is attached to the rotary table of the machine tool. The second one is using a rotary dynamometer that is directly attached to the spindle of the machine tool and cutting tool is attached to the dynamometer.

Contrary to three-axis milling, tool orientation in five-axis milling is continuously changed. Therefore, tool coordinate system has to be mapped into the workpiece coordinate system. Therefore, the equation to calculate cutting force in X , Y , Z direction for three-axis milling in Eq.(6-7) is transformed to five-axis milling as follows,

$$\begin{bmatrix} F_X(\varphi) \\ F_Y(\varphi) \\ F_Z(\varphi) \end{bmatrix} = \sum_{j=1}^m \sum_{i=1}^k [M] \times [M]_F \times \begin{bmatrix} F_{t,i,j}(\varphi, \phi) \\ F_{r,i,j}(\varphi, \phi) \\ F_{a,i,j}(\varphi, \phi) \end{bmatrix} \quad (6-11)$$

where $[M]$ is a mapping operator from the tool coordinate system to the workpiece coordinate system involving the tool orientation angles in the x -axis (θ_A) and the y -axis (θ_B).



Fig. 6-3 Experimental setup

6.5. Simulation and Experimental Results

A series of full immersion 3D slot milling tests were conducted with a 32 diameter carbide end mill with two cutting teeth, 11° helical angle and 4 mm minor radius. The machining was performed on five-axis milling (Tripteor X7 located in the technical Hall of Institut Français de Mécanique Avancée (IFMA) Aubière, France) and the cutting forces were measured using a three components dynamometer Kistler 9257B as shown in Fig. 6-3. Cutting parameters were set as

follow: cutting speed 1000 m/min and a series of axial immersion with 1, 2, 3, 4, 5, 8, 10 mm are applied under feedrate 0.1, 0.2, 0.3 mm/tooth. Cutting force coefficients were identified using feedrate 0,1 and 0.3 mm/tooth. Feedrate 0.2 mm/tooth is used for verification purpose.

6.5.1. Cutting Force Coefficients

Through experiments and data processing, the general trend of six cutting and edge force coefficients were determined and presented in Fig. 6-4. From this figures can be seen that the coefficients are very fluctuative. Then, the values of the force coefficients obtained from the experiment are fitted, thereby its value at every z elevation can be determined. Using a cubic polynomial fitting, the cutting and edge coefficients as a function of axial depth of cut (D) are expressed as follows,

$$\begin{aligned}
 K_{tc} &= (-0.877) D^3 + (18.6863) D^2 + (-116.6406) D + 748.0811 \\
 K_{rc} &= (0.3048) D^3 + (-4.3090) D^2 + (-1.8247) D + 58.5752 \\
 K_{ac} &= (-2.4127) D^3 + (43.9065) D^2 + (-236.4195) D + 58.3667 \\
 K_{te} &= (0.0197) D^3 + (-0.5740) D^2 + (3.775) D + 24.5360 \\
 K_{re} &= (-0.0405) D^3 + (0.7798) D^2 + (-2.6908) D + 3.2515 \\
 K_{ae} &= (0.0522) D^3 + (-1.1549) D^2 + (5.1104) D + -0.057
 \end{aligned} \tag{6-12}$$

From the graph in Fig. 6-4 can be seen that the cutting edge coefficients (K_{tc} , K_{rc} , K_{ac}) have larger fluctuation ranges compared with those of the edge coefficient (K_{te} , K_{re} , K_{ae}). According to Ge et al. [104], this phenomenon can be explained by metal removal mechanism acting on the rake and flank contact areas. Drastic changes of cutting (shearing) coefficients are characterized by the size effect. Larger force coefficient at smaller axial depth of cut was also found by Erdim et al. [57]. Several studies [7, 27, 124] were also reported that the cutting force coefficients increase as the cut thickness decrease.

The cutting forces coefficients are calibrated experimentally for a specific workpiece material-tool geometry pair [39]. Therefore, different coefficients need to be identified when a different workpiece material-tool geometry pair is employed. The cutting force coefficients in Eq.(6-12) were derived from the

experimental data with various feedrate and depth of cut. Hence, it can be used to predict the cutting force as a function of axial depth of cut and feedrate. Because the effect of cutting speed was not taken into account in the model development, it is probably not applicable for variety of cutting speed. Study on the relationship of cutting speeds on the force coefficients has been performed by Ge et al. [104]. They mentioned that the force coefficients tend to increase as the cutting speed decrease, and vice versa.

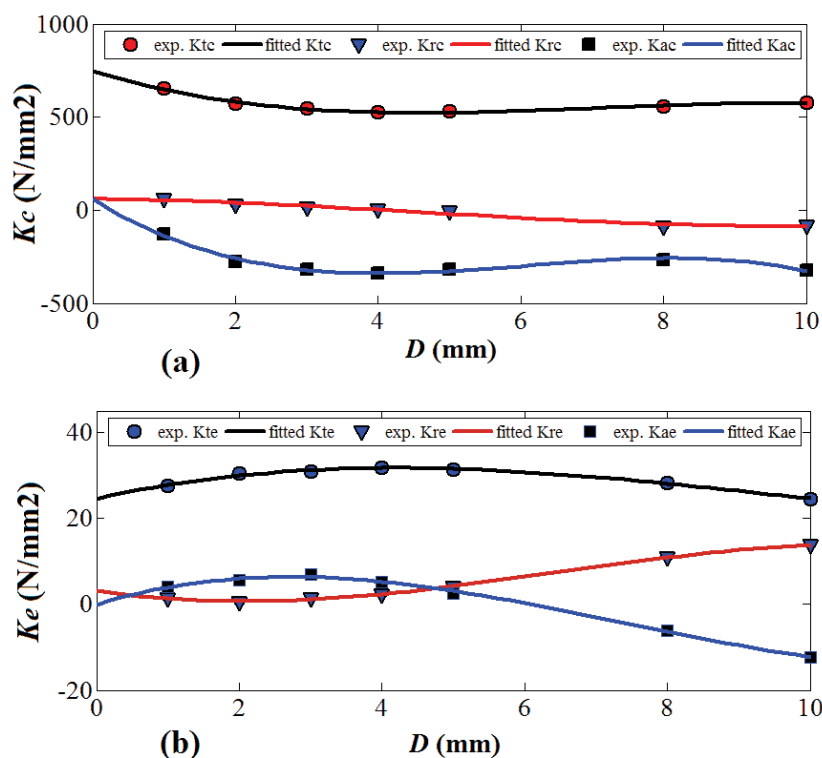


Fig. 6-4 Experimental and fitting of coefficients data, a) cutting coefficients, b) edge coefficients

6.5.2. Model Implementation in Five-Axis Milling

Cutting experiments were performed to verify the proposed model in five-axis milling. For this purpose, the same cutting tool and workpiece material were utilized. The cutting speed and feedrate used in tests were 1000 m/min and 0.2 mm/tooth, respectively. The verifications were performed for two milling operations, semi-finish milling and finish milling.

For the first test, a part and workpiece model as shown in Fig. 6-5a was used and the length of cut, which were calculated using ABS, are presented in Fig. 6-5b. The cutting force components during one tool pass were measured and compared against the calculated cutting forces. From Fig. 6-6 through Fig. 6-8 show that the profile of the graph of the measured cutting forces and their value correspond to the graph of calculated cutting forces. It can be seen that calculated cutting force in the x -axis (F_x) and the y -axis (F_y) match well with the experimental data in both their trends and amplitudes. In most of regions, the deviation with regard to measured cutting force were below 15%. Meanwhile in Z direction (F_z), higher deviation were found. Mostly the deviations were low, but in some region it reached until 40%. The second validation test was performed for a free-form workpiece surface as depicted in Fig. 6-9a. The length of cut with respect to the machining time is presented in Fig. 6-9b. As it is demonstrated in Fig. 6-10 through Fig. 6-12, calculated and measured cutting force components match well. In general, the difference between the calculated and measured force amplitudes were below 10%. It can be considered that there is a strong relationship between them.

Many reports [51, 88, 100-122] studied cutting force prediction. Mostly they were performed a plain cutting in three-axis milling, and only few studies that were developed for five-axis milling. Becze et al. [125] proposed an analytical force model and then it was verified using hardened tool steel (D2 tool steel). They concluded that the proposed model was able to predict the cutting force well, but there is some deviation of the predicted cutting force from the actual forces, which can reach until 40%. Erdim [51] used mechanistic force model to predict the cutting forces, and then the proposed model was applied for feedrate scheduling of a complex part in five-axis milling. The method could predict the cutting forces of the optimization feedrate with the maximum deviation about 28%. Boz et al. [88] was also developed an cutting force prediction model. According to the verification results, they stated that the simulated and measured cutting force match reasonably well within the deviation band of 0-20%.

In the real five-axis machining, there are many factors that affect the magnitude of cutting forces in which some of them did not taken into consideration in the cutting force model proposed in this study. The flexibility inherently associated by two additional axes of the machine/workpiece system causes significant vibrations, which in turn may lead to tool chatter. This factor might contribute to the deviation of the simulation results due to the force coefficients were calculated using a set of experimental data that were obtained from three-axis milling. Another factor that greatly influenced the magnitude and distribution of the cutting force is the cutter run-out effect, which is general phenomenon in the milling process. The existence of these factors that might influence the discrepancy between the calculated and measured cutting forces.

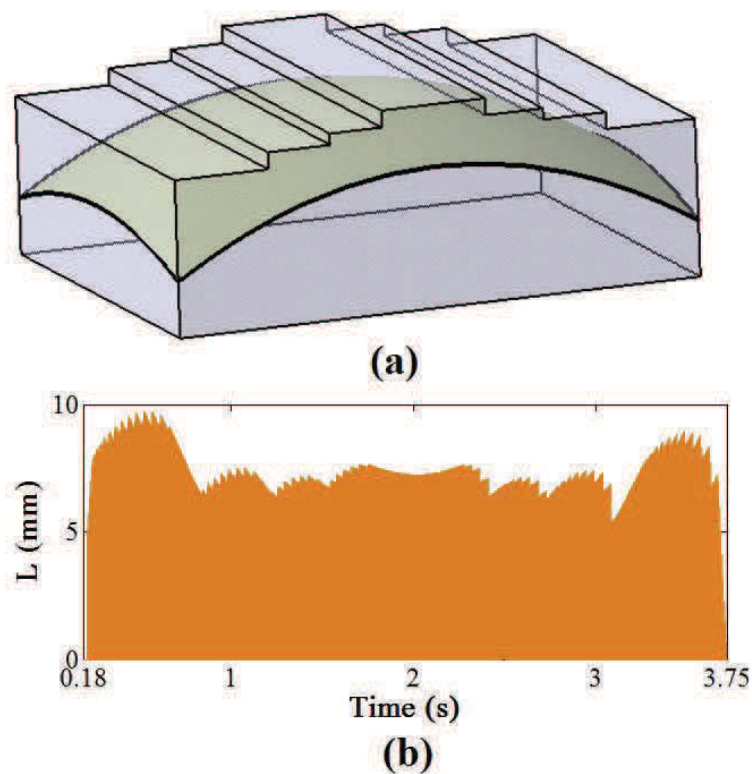


Fig. 6-5 Test for semi-finish milling, a) part and workpiece model, b) the length of cut progression (L)

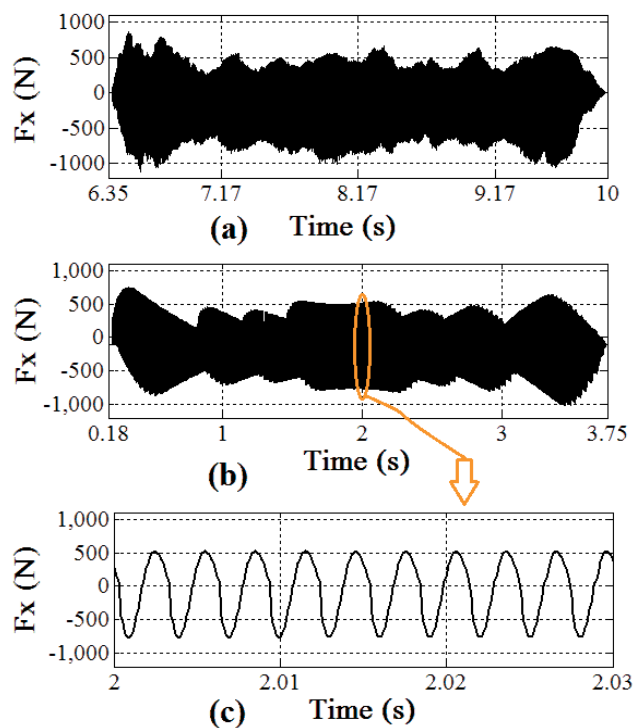


Fig. 6-6 Comparison of F_x , a) measured, b) calculated, c) detail of calculated

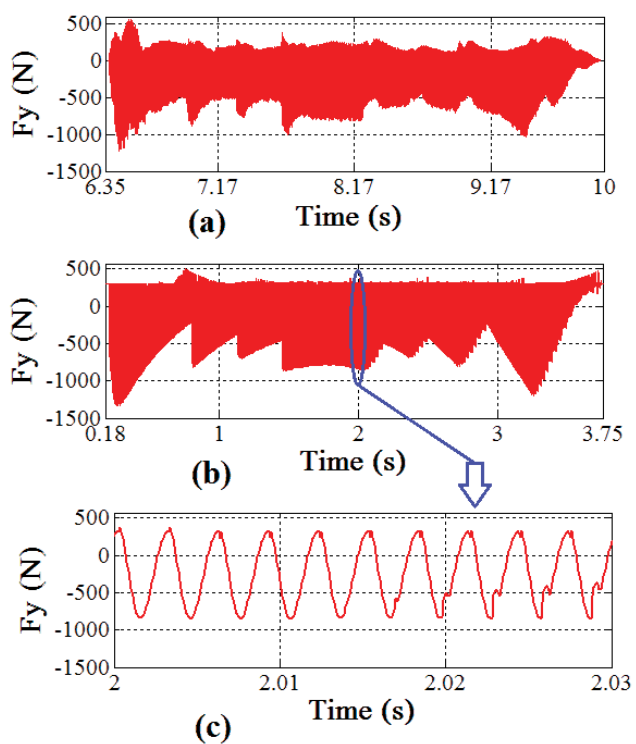


Fig. 6-7 Comparison of F_y , a) measured, b) calculated, c) detail of calculated

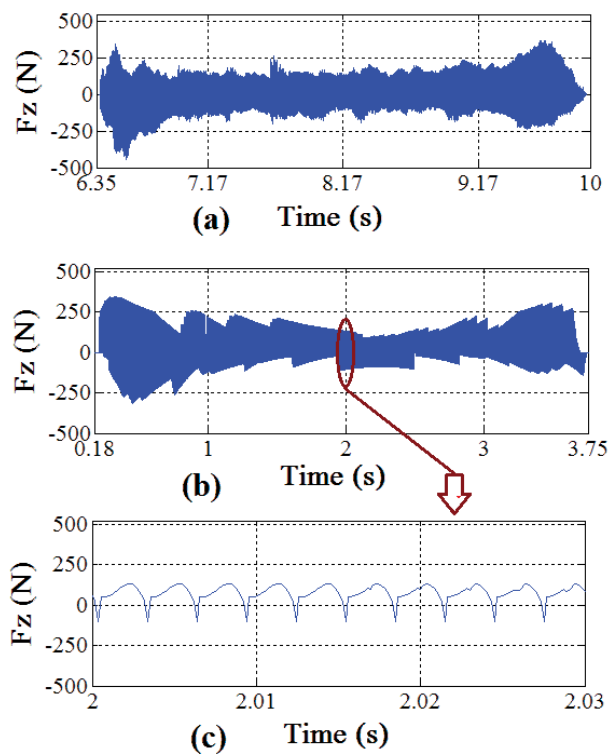


Fig. 6-8 Comparison of F_z , a) measured, b) calculated, c) detail of calculated

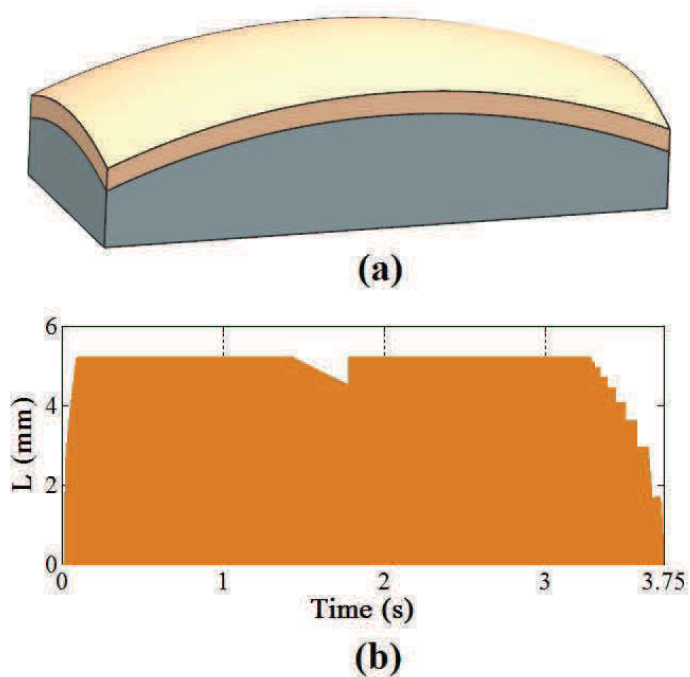


Fig. 6-9 Test for finish milling, a) part and workpiece model, b) the length of cut progression (L)

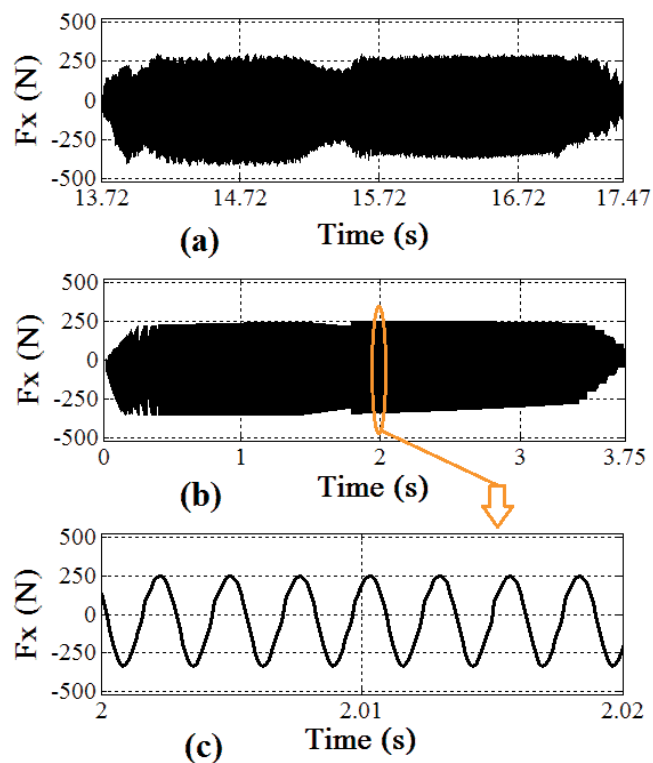


Fig. 6-10 Comparison of F_x , a) measured, b) calculated, c) detail of calculated

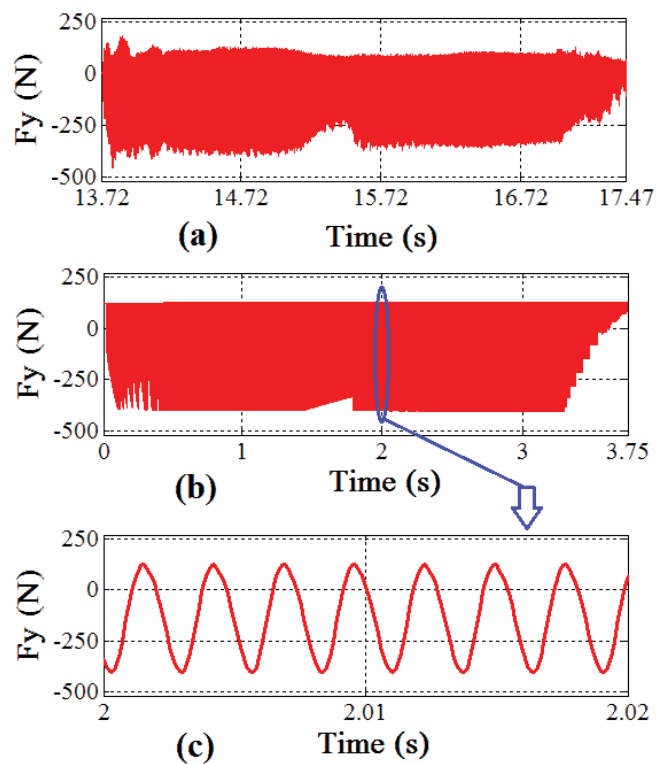


Fig. 6-11 Comparison of F_y , a) measured, b) calculated, c) detail of calculated

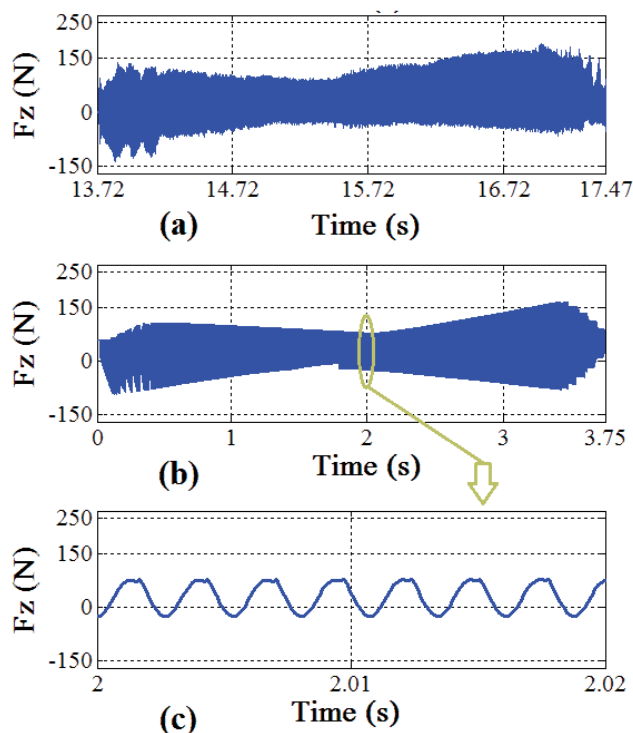


Fig. 6-12 Comparison of F_z , a) measured, b) calculated, c) detail of calculated

4.1. Conclusion

This chapter presents a generalized mathematical method to predict the instantaneous cutting forces. The cut geometry models that have been developed in the previous chapter were employed to support the cutting forces prediction model. Mechanistic cutting force model, which breaks down the cutting force into three components (tangential, radial and axial), was used in this study. For a simulation purpose, the force coefficients (cutting coefficient and edge coefficient) were determined using the cutting forces data that were obtained from a series of experimental works. Cutting force coefficients as a function of axial depth of cut was defined using a cubic polynomial fitting.

The proposed method has been tested to generate cutting forces during a semi finish and a finish milling. Using the same part and workpiece model, the actual cutting force were measured experimentally. The test results showed that the calculated cutting forces have a good agreement, both in trends and amplitudes, with the cutting force generated from the experimental work .

CHAPTER 7

CONCLUSION AND FUTURE WORKS

7.1. Conclusion

In this study, the geometries of cross section of the instantaneous CWE in five axis milling have been defined. The length of cut was determined by defining two points, the LE-point and the UE point. Determination of cross cut geometry for continuous tool orientation change is not as simple as when milling with a constant tool orientation. The tool orientation continuously change in between two consecutive CC-points and the complexity of the workpiece profile made the CWE become very dynamic. The CWE was also proven to be influenced by the inclination angle that normally exist in five-axis milling. When machining using a negative inclination angle, LE-point is always located at the front cutting edge. Otherwise, it is located at the back cutting edge. For toroidal cutter, increasing positive inclination angle will decrease the length of cut. On the other hand, increasing negative inclination angle will increase the length of cut.

The new methods to generate CWE for roughing, semi finishing and finishing milling with a flat-end cutter and toroidal cutter were presented. The UE-point was calculated using a combination of discretization and analytical method. During rough milling and semi-finish, a method called the *Toroidal-boundary* was employed to obtain the UE-point when it was located on the cutting tool at toroidal side. On the other hand, a method called the *Cylindrical-boundary* was used to calculate the UE-point for a flat-end cutter and a cylindrical side of toroidal cutter. All of the equations, which were derived in this study, were used to develop a simulation program using Matlab. It was called Analytical Boundary Simulation (ABS). The accuracy of the proposed models were verified two times, first by comparing the coordinate of the UE-points with respect to the workpiece surface, and the second by employing CAD software Siemens-NX. The results

proved that the proposed method was accurate. The efficiency of the proposed model was also compared with the Z-mapping method in generating the CWE. The result confirmed that the proposed model was more efficient in term of computational time. For the case of the shape of workpiece surface is a non-straight staircase, the wall surface was represented by polynomial curve. The method to define the UE-point when the engagement located on the wall surface was called the *curve boundary* method. The method was also verified using Siemens-NX, and the result showed that the error when the UE-point located on the wall surface was below 6%.

Meanwhile for finish milling, the surface is discretized using normal vectors. Despite the workpiece surfaces were discretized, but there was no calculation to check the intersection between the cutter and the representative vectors. They were only used as the reference to define the shape of the surface at every CC-point, mathematically. The engagement point was obtained using a combination of workpiece surface equation, parametric equation of cutting tool and tool orientation data. The accuracy of the developed method was verified using the same method that was applied in semi-finish milling. The results showed that the proposed model produces relatively small errors. For both cutting tools, it was found that the errors were less than 4%. It proved the accuracy of the method. Moreover, the method was eliminating the need for large number of Z-map to define the workpiece surface. The computational time test proved that it was more efficient compared with the Z-mapping method.

Cutter workpiece engagement model was applied for supporting the method to predict the cutting forces. In this study, the mechanistic cutting force model was used. Cutting force coefficients as a function of axial depth of cut was obtained using a cubic polynomial fitting. The test results showed that the calculated cutting forces have a good agreement with the cutting force generated from the experimental work.

7.2. Future Work

In an analytical method, the algorithm developed for the CWE generator is applicable only for a specified cutting tool geometry and workpiece surface.

Because the study in this area is still lack, many topics still can be developed and explored. For future works, there are several research topics, which are related to the current research area, can be developed, such as,

1. Develop an efficient method to generate the in-progress workpiece surface data for supporting Cutter Workpiece Engagement model.
2. Develop an analytical and hybrid method for others type of cutting tool geometry, and also for a solid cutting tool.

REFERENCES

- 1 Yun, W.S., Cho, D.W., Ehmann, K.F. (2002). Development of a virtual machining system, part 1: approximation of the size effect for cutting force prediction. *International Journal of Machine Tools & Manufacture*, 42, 1595-1605.
- 2 Yun W.S., Ko J.H., Cho D.W., Ehmann K.F. (2002). Development of a virtual machining system, part 2: prediction and analysis of a machined surface error. *International Journal of Machine Tools & Manufacture*, 42, 1607-1615.
- 3 Yun, W.S., Ko, J.H., Lee, H.U., Cho, D.W. (2002). Development of a virtual machining system, part 3: cutting process simulation in transient cuts. *International Journal of Machine Tools & Manufacture*, 42, 1617-1626.
- 4 Merdol, S.D. & Altintas Y. (2008). Virtual Cutting and Optimization of three-axis milling processes. *International Journal of Machine Tool & Manufacture*, 48, 1063-1071.
- 5 Technology Trends, Am. Mach. 1994, 138 (16).
- 6 Salami, R., Sadeghi M.H., Motakef, B. (2007). Feedrate optimization for 3-axis ball-end milling of sculptured surfaces. *International Journal of Machine Tools and Manufacture*, 47(5), 760–767.
- 7 Altintas, Y., & Spence A.D. (1991). End Milling Force Algorithms for CAD Systems. *Manufacturing Technology CIRP Annuals*, 40, 31-34.
- 8 Spence A.D., & Altintas, Y. (1994). A solid modeler based milling process simulation and planning system. *Trans ASME J Eng Ind*, 116 (1), 61–69.
- 9 El-Mounayri, H., Spence, A.D., Elbestawi, M.A. (1998). Milling Process Simulation-A generic Solid Modeller Based Paradigm. *Journal of Manufacturing Science and Engineering*, 120,(2), 213-221.
- 10 Fussel, B.K., Ersoy, C., Jerard, R.B. (1992). Computer Generated CNC Machining Feedrates. *ASME Japan/USA Symposium on Flexible Automation*, 1, 377-384.
- 11 Fussell, B.K., Jerard R.B., Hemmett J.G. (2001) Robust feedrate selection for 3-axis NC machining using discrete models. *ASME Journal of Manufacturing Science and Engineering*, 123, 214-224.

- 12 Jerard, R.B., Drysdale, R.L., Hauck, K., Schaudt, B., Magewick, J. (1989). Methods for detecting errors in Sculptured Surface Machining. *IEEE Computer Graphical and Applications*, 9-1, 26-39.
- 13 Park, J.W., Shin, Y.H., Chung, Y.C. (2005). Hybrid cutting simulation via discrete vector model. *Computer Aided Design*, 37 (4), 419-430.
- 14 Roth, D., Ismail, F., Bedi, S. (2005). Mechanistic modelling of the milling process using complex tool geometry. *International Journal of Advanced Manufacturing Technology*, 25(1-2), 140-4
- 15 Roth, D., Gray, P., Ismail, F., Bedi, S. (2007). Mechanistic modeling of 5-axis milling using an adaptive and local depth buffer. *Computer-Aided Design*, 39 (4), 302-312.
- 16 Yao, Z, (2005). *Finding Cutter Engagement For Ball End Milling of Tessellated Free-Form Surfaces*. Presented at ASME International Design Engineering Technical conferences”, DETC2005-84798
- 17 Aras, E, Hoi, D.Y., Geometric modeling of cutter/workpiece engagements in three axis milling using polyhedral representations. *J. Manufacturing Science and Engineering*, 2008, 8(3), 031007.
- 18 Yip-Hoi, D., Peng, X. (2007). *R-Tree Localization for Polyhedral Model Based Cutter/Workpiece Engagements Calculations in Milling*. Presented at ASME CIE.
- 19 Robert, J.A., & Sole, J. (1995). Constructing face octrees from voxel-based volume representations. *Computer Aided Design*, 27 (10), 783-791.
- 20 Li GJ, Yao YX, Xia PJ, Liu CQ, Wu C Extended octree for cutting force prediction. *Int. J. Mach. Tools and Manuf.* 2008; 39:866-873.
- 21 Jang, D., Kim, K., Jung, J. (2000). Voxel-based virtual multi-axis machining, *Int J Adv. Manuf. Technology*, 16, 709-713.
- 22 Ozturk, B., Lazoglu, I. (2006). Machining of free-form surfaces. Part I: Analytical chip load. *International Journal of Machine Tools and Manufacture*, 46(7-8), 728-735.
- 23 Spence, A., Altintas, Y., Kirkpatrick, D. (1990). Direct calculation of machining parameters from a solid model. *Comput Ind.*, 14(4), 271-280.
- 24 Tunc, L.T., Budak, E. (2009). Extraction of 5 axis milling conditions from CAM data for process simulation. *Int J. Adv. Manuf. Technol.*, 43, 538-550.
- 25 Altintas, Y., Lee, P. (1998). Mechanics and dynamics of ball end milling. *ASME Journal of Manufacturing Science and Engineering*, 2, 219-234

- 26 Kline, W.A., DeVor, R.E. and Zdeblick, W.J. (1980). *A Mechanistic Model for the Force System in End Milling with Application to Machining Airframe Structures*. Paper presented at In North American Manufacturing Research Conference Proceeding, page 297, Dearborn, MI , Society of Manufacturing Engineers. Vol, XVIII.
- 27 Wan, M., Zhang W.H. (2007). Efficient calibration of instantaneous cutting force coefficients and run out parameters for general end mills. *Int. J Machine Tools Manuf.*, 47 (11), 1767-1776.
- 28 Gupta, S.K., Saini, S.K., Sparanklin, B.W., Yao, Z. (2005). Geometric algorithms for computing cutter engagement functions in 2.5D milling operations. *Computer Aided Design*, 37 (14), 1469-1480.
- 29 Bailey, T., Elbestawi, M.A., El-Wardany, T.I., Fitzpatrick P. (2002). Generic simulation approach for multi-axis machining, part 2: model calibration and feed rate scheduling, *ASME Trans J. Manuf. Sci. Eng.*, 124, 634-642.
- 30 Yazar, Z., Koch, K.F., Merick, T., Altan, T. (1994). Feedrate optimization based on cutting force calculations in 3-axis milling of dies and molds with sculptured surfaces. *Int. J. Mach. Tool Mnuf.*, 34 (3), 365-377.
- 31 Karunakaran KP. (2004). Industry watch-modern machine tools, pp 52-58.
- 32 Li, Q., Budong, Y., Shuting, L. (2008). Comparing and combining off-line feedrate rescheduling strategies free-form surface machining with feedrate acceleration and deceleration. *Robot Comput-Integr. Manuf.*, 24, 796-803.
- 33 Elkeran, A., El-Baz, M.A. (2003). NURBS federate adaptation for 3-axis CNC machining, <http://www.maintenanceresources.com>.
- 34 Wang, W.P. (1988) Solid modeling for optimizing metal removal three dimensional NC end milling. *ASME journal of Engineering for industry*, 113(2),169-175.
- 35 Jang, D.J., Kim, K.S., Jung, J.M. (2000). Voxel-based virtual multi-axis machining. *Int J Adv Manufact Technol*, 16(10), 709–713
- 36 Ip, W.L.R., Lau, H.C.W., Chan, F.T.S. (2003). An economical sculptured surface machining approach using fuzzy models and ball nosed cutters. *Journal of Materials Processing Technology*, 138, 579-585.
- 37 Budak, E., Tekeli, A. (2005). Maximizing chatter free material removal rate in milling through optimal selection of axial and radial depth of cut pair. *Annals of the CIRP*, 54(1), 353-356.

- 38 Feng, H.Y., Menq, C.H. (1994). The prediction of cutting forces in the ball-end milling process-II. Cut geometry analysis and model verification. *Int. J. Mach Tools Manufact*, 34(5), 711–19.
- 39 Altintas, Y. (2000). *Manufacturing Automation: Metal Cutting mechanics, Machine Tool Vibrations, and CNC Design*. Cambridge University Press.
- 40 Cherif, M., Thomas, H., Furet, B., Hascoet, J.Y. (2004). Generic modeling of milling forces for CAD/CAM applications. *International Journal of Machine Tools and Manufacture*, 44, 29-37.
- 41 Marin, F.B., Banu, M., Marinescu, V., Epureanu, A., Constantin, I. (2009) *AI technique for online non linear feedrate scheduling*. Paper presented at the 8th WSEAS Int. Conf. On Non Linear Analysis, Non-Linear Systems and Chaos. ISBN: 978-960-474-094-9
- 42 Li, Z.Z., Zheng, M., Zheng, L., Wu, Z.J., Liu, D.C. (1998). A solid model based milling process simulation and optimization system integrated with CAD/CAM. *J. Mater. Process Technol.*, 36 (9), 2553-585.
- 43 Ip, W.L.R. (1998). A fuzzy basis material removal optimization strategy for sculptured surface machining using ball-nosed cutters. *Int. J. Prod. Res.*; 36(9), 2553-2571.
- 44 Lan, T.S., Hsu, K.S. (2007). The implementation of optimum MRR on digital PC based lathe system. *Int. J. Adv. Manufacturing Technology*, 35(3-4), 248-254.
- 45 Chen, J., Huang, Y., Chen, M. (2005). Feedrate optimization and tool profile modification for the high-efficiency ball-end milling process. *Int. J. Mach. Tools Manuf.*, 45, 1070-1076.
- 46 Kurt, M., Bagci, E. (2011). Feedrate optimisation/scheduling in sculptured surface machining; a comprehensive review, applications and future directions. *International Journal of Advance Manufacture Technology*, 55, 1037-1067.
- 47 Jerrard, R.B., Fussell, B.K., Eran, M.T. (2001). *On-line optimization of cutting conditions for NC machining*. Paper presented at NSF Design, Manufacturing & Industrial Innovation Research Conference, Tampa, Florida.
- 48 Choi, B.K., Jerrard, R. *Sculptured surface machining. Theory and Applications*. Kluwer Academic, Dordrecht.

- 49 Nehez, K., Csaki, T. (2002). *Cutting force modeling possibilities in open GL based milling simulators*. Paper presented at The 10th international conference on machine design and production, Cappadocia, Turkey, 127-138.
- 50 Baek, D.K., Ko, T.J., Park, J.W., Kim, H.S. (2005). Chip load control using a NC verification model based on z-map. *J KSPE*, 22 (4), 68-75.
- 51 Baek, D.K., & Ko, T.J. (2008). Feedrate scheduling for free-form surface using an NC verification model. *Int. J Mach Tools Manuf.*, 48 (2), 163-175.
- 52 Imani, B.M., Sadeghi, M.H., Elbestawi, M.A. (1998). An improved process simulation system for ball-end milling of sculptured surfaces. *Int. J Mac. Tools Manuf.*, 38(9), 1089-1107
- 53 Lim, E.M., & Menq, C.H. (1997). Integrated planning for precision machining of complex surfaces. Part 1: cutting path and feedrate optimization. *Int. J Mach Tool Manufact.*, 37(1), 61-75.
- 54 Guzel, B.U., & Lazoglu, I. (2004). An enhanced force model for sculptured surface machining. *Machining Sci. Technology*, 44(14), 1511-1526.
- 55 Lazoglu, I. (2003). Sculpture surface machining: a generalized model of ball-end milling force system. *Int. J Mach. Tools Manuf.*, 43, 453-462.
- 56 Guzel, B.U., & Lazoglu, I. (2004). Increasing productivity in sculptured surface machining via off-line piecewise variable feedrate scheduling based on the forces system model. *Int. J. Mach. Tools Manuf.*, 44(1), 21-28.
- 57 Erdim, H., Lazoglu, I., Ozturk, B. (2006). Feedrate scheduling strategies for free-form surfaces. *Int. J. Mach. Tools & Manuf.*, 46, 747-757.
- 58 Lim, M., Hsiang, M.C. (1997). Integrated planning for precision machining of complex surface, part I: cutting path and feedrate optimization. *Int. J Mach. Tools Manuf.*, 37, 61-75.
- 59 Kim, K.K., Kang, M.C., Kim, J.S., Jung, Y.H., Kim, N.K. (2002). A study on the precision machinability of ball end milling by cutting speed optimization. *J Mater process Technol.*, 130-131, 357-362.
- 60 Fussel, B.K., Jerard, R.B., Richards, N., Yalcin, C. (2002). *NC machining feedrate optimization using on-line model tuning and adaptive control*. Paper presented at the NSF design. service and manufacturing grantees and research conferences, Puerto Rico.
- 61 Jerard, R.B., Fussell, B.K., Xu, M., Yalcin, C. (2006). Process simulation and feedrate selection for three-axis sculptured surface machining. *Int. J Manuf. Res.*, 1(2), 136-156.

- 62 Zhang, L., Feng, J., Wang, Y., Chen, M. (2009). Feedrate scheduling strategy for free-form surface machining through an integrated geometric and mechanistic model. *Int. J. Adv. Manuf. Technol.*, 40(11-12), 1191-1201.
- 63 Lee, H.U., Cho, D.W. (2003). An intelligent feedrate scheduling based on virtual machining. *Int J Adv. Manuf. Technol.*, 22, 873-882.
- 64 Ko, J.H., Cho, D.W. (2004) Feedrate scheduling model considering transverse rupture strength of a tool for 3D ball-end milling. *Int. J. Adv. Manuf.*, 44(10), 1047-1059.
- 65 Tounsi N, Elbestawi M.A. (2003). Optimized feed scheduling in three axes machining, part I: fundamentals of the optimized feed scheduling strategy. *Int. J. Mach. Tools Manuf.*, 43(3), 253-267.
- 66 Yip-Hoi, D., Huang, X. (2006). Cutter/Workpiece engagement feature extraction from solid models for end milling. *Journal of manufacturing science and engineering, Transaction of the ASME*, 128 (1), 249-260
- 67 Zeid I. CAD/CAM: Theory and Practice. McGraw-Hill Inc. 1991
- 68 Farin, G. (1993). *Curves and surfaces for Computer Aided Geometric Design-A practical guide*. Academic Press Inc. San Diego, CA, USA, 3rd Edition.
- 69 Requicha AAG. (1980). Representations for rigid solids: Theory, methods and systems. *ACM Computing Surveys.*, 12(4), 437-464.
- 70 Larue, A., Altintas, Y. (2004). Simulation of flak milling processes. *Int. J. Machine Tools and Manuf.*, 45, 549-559.
- 71 El-mounayri, H., Elbestawi, M.A., Spence, A.D., Bedi, S.(1997). General geometric modeling approach for machining process simulation. *Int. J. Adv. Manuf. Techno.*, 13, 237-247.
- 72 Woon-Soo, Y., Jeong-Hoon, K., Han, L, Dong-Woo, C. (2002). Development of a virtual machining system, Part 3: Cutting process simulation in transient cuts. *Int. J. Mach. Tools. Manuf.* 42(15), 1617-1626.
- 73 Jerard, R.B., Drysdale, R.L., Hauck, K.E., Schaudt, B., Magewick, J. (1989). Methods for detecting errors in numerically controlled machining of sculptured surfaces. *Computer Graphics and Applications, IEEE*, 9(1), 419-430.
- 74 Baek, N., Maeng, S.R., Shin, S.Y., Choi, B.K. (2003). A Z-map update method for linearly moving tools. *Computer Aided design*, 35:995-1009.

- 75 Baek, N., Maeng, S.R., Shin, S.Y., Choi, B.K. *A fast NC simulation method for circularly moving tools in the Z-map environment*. Proceeding of the Geometric Modeling and Processing 2004 (GMP'04).
- 76 Ozturk, B, Lazoglu, I. (2006). Machining of free-form surfaces. Part I: Analytical chip load. *Int. J. of Mach. Tools and Manuf.*, 46(7), 728-735.
- 77 Kral, I.H. (1986). *Numerical Control Programming in APT*, Prentice-Hall, New Jersey.
- 78 Shao, Z., Guo, R., Li, J. (2011). Accurate modeling method for generalized tool swept volume in 5-axis NC Machining Simulation, *Journal of Software*, 6 (10), 2056-2063.
- 79 Marciniak, K. (1987). Influence of surface shape on admissible tool positions in 5-axis face milling. *Computer Aided Design*, 19 (5), 233-236
- 80 Vickers, G.W. & Quan, K.W. (1989) Balls-mills versus end mill for curved surface machining. *Journal of Engineering for Industry*, Transaction of the ASME, 111.
- 81 Cho, H.D., Jun, Y.T., Yang, M.Y. (1993). Five axis CNC milling for effective machining of sculptured surfaces. *Int. Journal of Production Research*, 31(11), 2559-2573.
- 82 Kruth J.P. & Klewais, P. (1994). Optimization and dynamic adaptation of the cutter inclination during five axis milling of sculptured surfaces. *Ann. Of the CIRP*, 43(I), 443-448.
- 83 Bedi, S., Gravelle, S., Chen, Y.H. (1997). Principal curvature alignment technique for machining complex surface. *Journal of Manufacturing Science and Engineering, Transaction of the ASME*, 119, 756-765.
- 84 Choi, B.K. and Jun, C.S. (1989). Ball-end cutter interference avoidance in NC machining of sculptured surfaces. *Computer Aided Design*, 21(6), 371-378.
- 85 Jensen, C.G., & Anderson, D.C. (1993). Accurate tool placement and orientation for finished surface machining, *J. Design and Manufacture*, (3), 251-261.
- 86 Li, X.S., Jerard, R.B. (1994). 5-axis machining of sculptured surface with a flat-end cutter. *Computer Aided Design*, 26 (3), 165-178.
- 87 Wang, Y.M., Deng, Z.P., Yan, X.D. (1999). A modified method for determining flat-end cutter orientation in five-axis NC machining. *Int. Journal of Flexible Automation and Integrated Manufacturing*, 7.

- 88 Rao, A., & Sarma, R. (2000). On local gouging in five-axis sculptured surface machining using flat-end tools. *Computer Aided Design*, 32, 409-420.
- 89 Lee, Y.S. (1997). Admissible tool orientation control of gouging avoidance for 5-axis complex surface machining. *Computer Aided Design*, 29(7), 507-521.
- 90 Kumanchik, L.M., Schmitz, T.L. (2007). Improved analytical chip thickness model for milling. *Precision Engineering*, 31, 317-324.
- 91 Gani, E.A., Kruth, J.P., Vanherck, P., Lauwers, B. (1997). A geometrical model of the cut in five axis milling accounting for the influence of tool orientation. *Int. J. Adv. Manuf. Technology*, 13, 677-684.
- 92 Boz, Y., Erdim, H., Lazoglu, I. (2011). Modeling cutting forces for five axis milling of sculptured surfaces. *J. Advanced Materials Research*, 223, 701-712.
- 93 Chiou, C.J., & Le, Y.S. (2002). Swept surface determination for five-axis numerical control machining. *Int. J. Mach. Tools and Manuf.*, 42 , 1497-1507.
- 94 Weinert, K., Du, S., Damm, P., Stautner, (2004). M. Swept volume generation for the simulation of machining processes. *Int. J. Mach. Tools and Manuf.*, 44, 617-628.
- 95 Du, S., Surmann, T., Webber, O. (2005). Weinert K. Formulating swept profile for five-axis tool motions. *Int. J. Mach. Tools and Manuf.*, 45, 849-861.
- 96 Yao, Z. and Gupta, S.K. (2004). Cutter path generation for 2.5D milling by combining multiple different cutter path patterns. *Int. J. Prod. Res.*, 42(11), 2141-2161.
- 97 Hatna, A., Grieve, R.J. & Broomhead, P. (1998). Automatic CNC milling of pocket: geometric and technological issues. *Computer Integrated Manufacturing Systems*, 11 (4), 309-330.
- 98 Toh, C.K. (2005). Design, evaluation and optimisation of cutter path strategies when high speed machining hardened mould and die materials. *Int. J. Material and Design*, 26, 517-533.
- 99 Li, S. & Jerard, R.B. (1994). 5 axis machining of sculptured surfaces with a flat end cutter. *Computer Aided Design*, 26 (3), 165-178

- 100 Wang, J.J.J., & Zheng, C.M. (2002). Identification of shearing and ploughing cutting constants from average forces in ball-end milling. *Int. J Machine Tools and Manufacture*, 42 (6), 765-774.
- 101 Altintas, Y., Eynian, M. (2008). Identification of dynamic cutting force coefficients and chatter stability with process damping. *CIRP ann Manuf. Technol*, 57 (1), 371-374
- 102 Tukora, B. & Tibor, S. (2011). Real-time determination of cutting force coefficients without cutting geometry restriction. *Int. J Mach Tools Manuf*, 51 (12), 8719
- 103 Lee, H.U. & Cho, D.W. (2007). Development of a reference cutting force model for rough milling feed rate scheduling using FEM analysis. *Int. J. Mach. Tools Manuf*, 47 (1), 158-167.
- 104 Ge, G., Baohai, W., Dinghua, Z., Ming, L. (2013). Mechanistic identification of cutting force coefficients in bull-nose milling process. *Chinese Journal of Aeronautics*, 26 (3), 823-830.
- 105 Armarego, E.J.A., & Epp, C.J. (1970). An investigation of Zero Helix Peripheral Up-Milling. *International Journal of Machine Tool Design and Research*, 10, 273-291
- 106 Budak, E., Altintas, Y., Armarego, E.J.A. (1996) Prediction of Milling Force Coefficient from Orthogonal Cutting Data. *ASME Journal of Manufacturing Sciences and Engineering*, 118 (2) , 216-224.
- 107 Gradisek, J., Kalveram, M., Weinert, K. (2004). Mechanistic identification of specific force coefficients for a general end mill. *Int. J. Machine Tool and Manuf.*, 44, 401-414.
- 108 Merchant, M.E., Basic Mechanics of the Metal Cutting Process. *Trans ASME Journal of Applied Mechanics*.
- 109 Koenigsberger, F. & Sabberwal, A.J.P. (1961). An investigation into the cutting force pulsations during milling operations. *International Journal of Machine Tool Design and Research* 1, 15-33.
- 110 Tlusty, J. & MacNeil, P. (1975). Dynamics of Cutting Forces in End Milling. *Annals of the CIRP*, 24, 21-25.
- 111 Sutherland, J.W. & DeVor, R.E. (1986). An Improved Method for Cutting Force and Surface Error Prediction in Flexible End Milling Systems. *Transactions ASME, Journal of Engineering for Industry*, 108, 269-279.
- 112 Budak, E. (1994). *Mechanics and Dynamic of Milling Thin Walled Structures*. Phd thesis, University of British Columbus, Canada.

- 113 Lee, P. & Altintas, Y. (1996). Prediction of Ball-End Milling Forces from Orthogonal Cutting Data. *International Journal of Machine Tools and Manufacture*, 36 (9), 1059-1072.
- 114 E.J.A. Armarego, N.P. Deshpande. (1991). Computerized end-milling force predictions with cutting models allowing eccentricity and cutter deflections, *Ann. CIRP* 40 (1), 25–29.
- 115 Zorev, N.N. (1986). *Metal Cutting Mechanics*. Pergamon Presss.
- 116 Yellowley, I. (1985). Observations of the Mean Values of Forces, Torque and Specific Power in the Peripheral Milling Process. *International Journal of Machine Tool Desing and Research*, 25 (4), 337-346.
- 117 Cheng, P.J., & Tsay J.T. (1997) A study on instantaneous cutting force coefficients in face milling. *Int. J Machine Tools and Manuf.*, 37 (10), 1397-1408.
- 118 Gonzalo, O., & Beristain, J. (2010). A method for the identification of the specific force coefficients for mechanistic milling simulation. *Int. J Mach. Tools Manuf.*, 50 (9), 765-774.
- 119 Martellotti, M. (1941). An analysis of the milling process. *Transactions of the ASME, J. of Engineering for Industry*, 63, 667-700.
- 120 Sawin, N. (1926). Theory of milling cutters. *Mechanical Engineering*, 48, 1203-1209.
- 121 Sabberwal, A. (1961). Chip section and cutting force during the milling operation, *CIRP Annals.*, 10, 197-203.
- 122 Shin, Y.C., Waters, A.J. (1997). A new procedure to determine instantaneous cutting force coefficients for machining force prediction. *Int. J. Machine Tools and Manuf.*, 37 (9), 1337-1351.
- 123 Jayaram, S., Kapoor, S.G., DeVor, R.E. (2001). Estimation of the specific cutting pressures for mechanistic cutting force models. *Int. J Machine Tools and Manufacture*, 41, 265-281.
- 124 Yun, W.S., Cho, D.W. (2001). Accurate 3-D force prediction using cutting condition independent coefficients in end milling. *Int. J. Machine Tools and Manuf.*, 41, 463-478.
- 125 Becze, C.E., Clayton, P., Chen, L., El-Wardany, T.I. (2000). Elbestawi, M.A. High-speed five-axis milling of hardened tool steel. *Int. J. of Mach. Tools & Man.*, 40, 869-885.

